Redox homeostasis in *Mycobacterium tuberculosis* is modulated by a novel actinomycete-specific transcription factor

Mehak Zahoor Khan[1] ID, Biplab Singha[1] ID, Mohammad Farhan Ali[2], Khushman Taunk[3], Srikanth Rapole[3], Samudrala Gourinath[2] & Vinay Kumar Nandicoori[1,*] ID

Abstract

Mycobacterium tuberculosis (*Mtb*) has evolved diverse cellular processes in response to the multiple stresses it encounters within the infected host. We explored available TnSeq datasets to identify transcription factors (TFs) that are essential for *Mtb* survival inside the host. The analysis identified a single TF, Rv1332 (AosR), conserved across actinomycetes with a so-far uncharacterized function. AosR mitigates phagocyte-derived oxidative and nitrosative stress, thus promoting mycobacterial growth in the murine lungs and spleen. Oxidative stress induces formation of a single intrasubunit disulphide bond in AosR, which in turn facilitates AosR interaction with an extracytoplasmic-function sigma factor, SigH. This leads to the specific upregulation of the CysM-dependent non-canonical cysteine biosynthesis pathway through an auxiliary intragenic stress-responsive promoter, an axis critical in detoxifying host-derived oxidative and nitrosative radicals. Failure to upregulate AosR-dependent cysteine biosynthesis during the redox stress causes differential expression of 6% of *Mtb* genes. Our study shows that the AosR-SigH pathway is critical for detoxifying host-derived oxidative and nitrosative radicals to enhance *Mtb* survival in the hostile intracellular environment.

Introduction

Mycobacterium tuberculosis (*Mtb*) is an airborne pathogen that has co-evolved with its human host to establish the continual loop of inhalation, active to chronic infection, latency, dissemination to virtually any organ, and transmission to other individuals. Though primarily phagocytosed by alveolar macrophages, *Mtb* has been found to reside in a variety of niches with distinct environments including dendritic cells (Wolf *et al*, 2007), neutrophils (Eum *et al*, 2010), hematopoietic (Tornack *et al*, 2017), and mesenchymal (Das *et al*, 2013) stem cells. The host-derived stresses that the bacterium is exposed to include oxidative and nitrosative radicals produced by NADPH-dependent phagocyte oxidase (phox) and inducible nitric oxide synthase (iNOS), respectively. Acidic conditions, starvation, and hypoxic conditions in the host all contribute toward inhibiting bacterial proliferation and survival. To effectively respond to the dynamic microenvironment of the hostile host, *Mtb* extensively remodels its transcriptional and translational networks, and thus, gene expression is fine-tuned in response to local environmental cues and growth conditions (Manganelli *et al*, 2004). Transcriptome analyses of intracellular *Mtb* uncover the reconfiguration of the transcriptional landscape upon infection, with the expression of multiple genes being controlled by regulators that help the bacterium adapt to shifting host-induced stresses, ultimately transducing the cascading stimuli into coordinated gene responses (Fontan *et al*, 2008; Rohde *et al*, 2012).

Studies over the past two decades have delineated the roles of several *Mtb* transcription factors (TFs) using various approaches, including the utilization of gene replacement and overexpression mutants, chromatin immunoprecipitation sequencing (ChipSeq), and gene expression profiling. However, TFs are often activated by either post-translational modifications or through interactions with other proteins, or a combination of these under a specific stress condition (Manganelli *et al*, 2004). Consequently, the regulons of ~ 60% TFs and their cellular roles are yet to be identified. To identify TFs that are vital for *Mtb* survival in the host microenvironment but are non-essential for *in vitro* growth conducive conditions, we explored the TnSeq data (Sassetti & Rubin, 2003; DeJesus *et al*, 2017; Bellerose *et al*, 2020) (Fig 1A, Appendix Table S1). One of the TFs encoded by *rv1332* (here named as *aosR*) is non-essential for *in vitro* growth but augments *in vivo* survival. Interestingly, AosR was found to be highly enriched in

1 National Institute of Immunology, New Delhi, India
2 School of Life Sciences, Jawaharlal Nehru University, New Delhi, India
3 National Centre for Cell Science, Pune, India
*Corresponding author. Tel: +91 11 26703789; Fax: +91 11 26742125; E-mail: vinaykn@nii.ac.in

actinomycetes, which can be a potential therapeutic target with minimal effects on the microbiome.

The present study was undertaken to address the following questions: (i) "What is the cellular and physiological role of this transcription factor and why does it aid in the survival within the host though not *in vitro*?", (ii) "what are the physiological triggers and the mode of activation of AosR?", (iii) "what does the AosR regulon comprise of?", (iv) "does it mediate its function(s) through any partner proteins, and if so, which?", and (v) "what is the significance of AosR-mediated regulation of the transcriptional network(s) it controls vis-à-vis *Mtb* survival and persistence within the host?". Collectively, our results indicate that inhibition of this novel redox-sensing regulatory network impacts global gene expression, dampening the pathogen's ability to combat host-induced redox stress, thus attenuating its survival in the host.

Results

AosR is a novel transcription factor that promotes *Mtb* virulence *in vivo*

Analysis of previously published *Mtb* TnSeq data revealed that transposon-induced mutants of 10 TFs display attenuated growth only when within the host (Appendix Table S1 and Fig 1A). Interestingly, only one among these—Rv1332 (AosR), is highly enriched in actinomycetes (99.8%). AosR is a 24 kDa protein that harbors an N-terminal CxxxC motif and a helix-turn-helix motif, followed by a domain of an unknown function, DUF2017 (Fig EV1A). Orthologs of AosR are highly conserved throughout the actinomycete order (Huerta-Cepas *et al*, 2019), with 25.5% of the orthologs belonging to mycobacteriaceae, 36.4% belonging to corynebacteriaceae, and 10.9% to nocardiaceae (Fig EV1B and Table 1). To investigate the effect of AosR on mycobacterial gene expression and adaptation, we constructed a genetic deletion mutant *RvΔaosR* in *MtbH37Rv* (*Rv*) (Fig EV2A and B). Complementation with AosR placed under its native promoter in an integrative plasmid (*RvΔaosR:: aosR*) restored AosR expression to levels similar in *Rv* (Fig EV2C). While the *RvΔaosR* mutant showed no growth difference *in vitro* in nutrient-rich or limiting media (Fig EV2D and E), its survival was compromised by ~ 10-fold within peritoneal macrophages (pΦ) at day 4 post-infection (p.i) (Fig 1B). Subsequently, we evaluated bacillary survival using the murine model of infection (Fig 1C). Equal deposition of all three strains was confirmed by determining CFUs in the

lung 24 h p.i (Fig 1D). The bacillary survival and growth rates of all three strains were indistinguishable a week after infection, both in the lungs and in the spleen (Fig 1D and E). As the infection progressed thereafter, the difference in the survival of *RvΔaosR* became distinctly apparent. The survival of *RvΔaosR* was ~ 10-fold lower than *Rv* and *RvΔaosR::aosR* at the persistence phase of infection (day 14 onwards; Fig 1D and E). These data suggest that Rv1332 is specifically required for mycobacterial survival within its host.

Mycobacterium tuberculosis is exposed to multiple stresses within host macrophages. The deletion of *aosR* did not affect *Mtb's* ability to combat acidic, starvation, or surfactant stresses (Fig EV3A–C). We observed a marginal (~ 1.5-fold) decrease in the survival of *RvΔaosR* upon exposure to nitrosative stress. However, *RvΔaosR* showed markedly compromised survival (~ 30-fold) upon exposure to peroxide radicals (Fig EV3E and F). This effect was dose-dependent, with increasing concentrations of CHP leading to poorer survival of *RvΔaosR* when compared with *Rv* and *RvΔaosR:: aosR* (Fig EV3G). Importantly, *RvΔaosR* displayed higher susceptibility to both peroxide stress (H_2O_2, CHP) and thiol oxidizer diamide (Fig 1F). Collectively, these data led us to conclude that AosR is a major contributor to mycobacterial survival during oxidative stress. Thus, we named it as **a**ctinomycetes **o**xidative **s**tress **r**egulator (**AosR**).

AosR protects the pathogen from phagocyte-derived reactive oxygen and nitrogen species

IFNγ elicits the generation of reactive oxygen species (ROS) and reactive nitrogen species (RNS) through Phox and iNOS, respectively (Fig EV4A). Phox is composed of two transmembrane glycoprotein subunits, gp22 and gp91, and three additional cytosolic subunits (Fig EV4A). Survival defects of *Mtb* mutants of *katG*, *sodA*, and *sodC* genes (whose products neutralize oxygen radicals) are restored in gp91 knockout mice (phox$^{-/-}$), underlining the importance of ROS in host defense mechanisms (Edwards *et al*, 2001; Piddington *et al*, 2001; Ng *et al*, 2004). To evaluate the contribution of AosR in protecting *Mtb* from host-derived stress, we infected peritoneal macrophages that were derived from wild-type C57BL/6 (WT) or murine strains that are deficient either in their ability to induce oxidative stress (phox$^{-/-}$) or both oxidative and nitrosative stresses (IFNγ$^{-/-}$) (Fig 2A). *RvΔaosR* mutants showed compromised survival within the peritoneal macrophages isolated from wild-type mice, which was

▶

Figure 1. AosR is a novel redox-responsive transcription factor.

A Schematic outline of the strategy used for the identification of *rv1332/aosR*.

B Single-cell suspensions of *Rv*, *RvΔaosR*, and *RvΔaosR::aosR* strains were used to infect pΦ isolated from Balb/C at 1:10 MOI. Cells were lysed at indicated time points, and the intracellular survival was enumerated. Data are presented as mean CFU log$_{10}$/ml $\pm$ SEM and are representative of two biologically independent experiments, each performed in triplicates (*n* = 3).

C Balb/C mice were aerosolically challenged with *Rv*, *RvΔaosR*, and *RvΔaosR::aosR* strains. Each data point represents log$_{10}$ CFU obtained from the infected lung of mice, and error bar depicts the median with interquartile range for each group.

D Each data point represents log$_{10}$ CFU obtained from the infected spleen of a mice, and the error bar depicts the mean with SD for each group.

E Bacterial strains were treated with indicated oxidizing agents for 24 h, and the survival was monitored. Control represents untreated cultures. Data are presented as mean CFU log$_{10}$/ml $\pm$ SEM and are representative of two biologically independent experiments, each performed in triplicates (*n* = 3).

Data information: Statistical significance was analyzed using one-way ANOVA followed by a *post hoc* test (Tukey test; GraphPad prism). *P < 0.05; **P < 0.005; ***P < 0.0005.
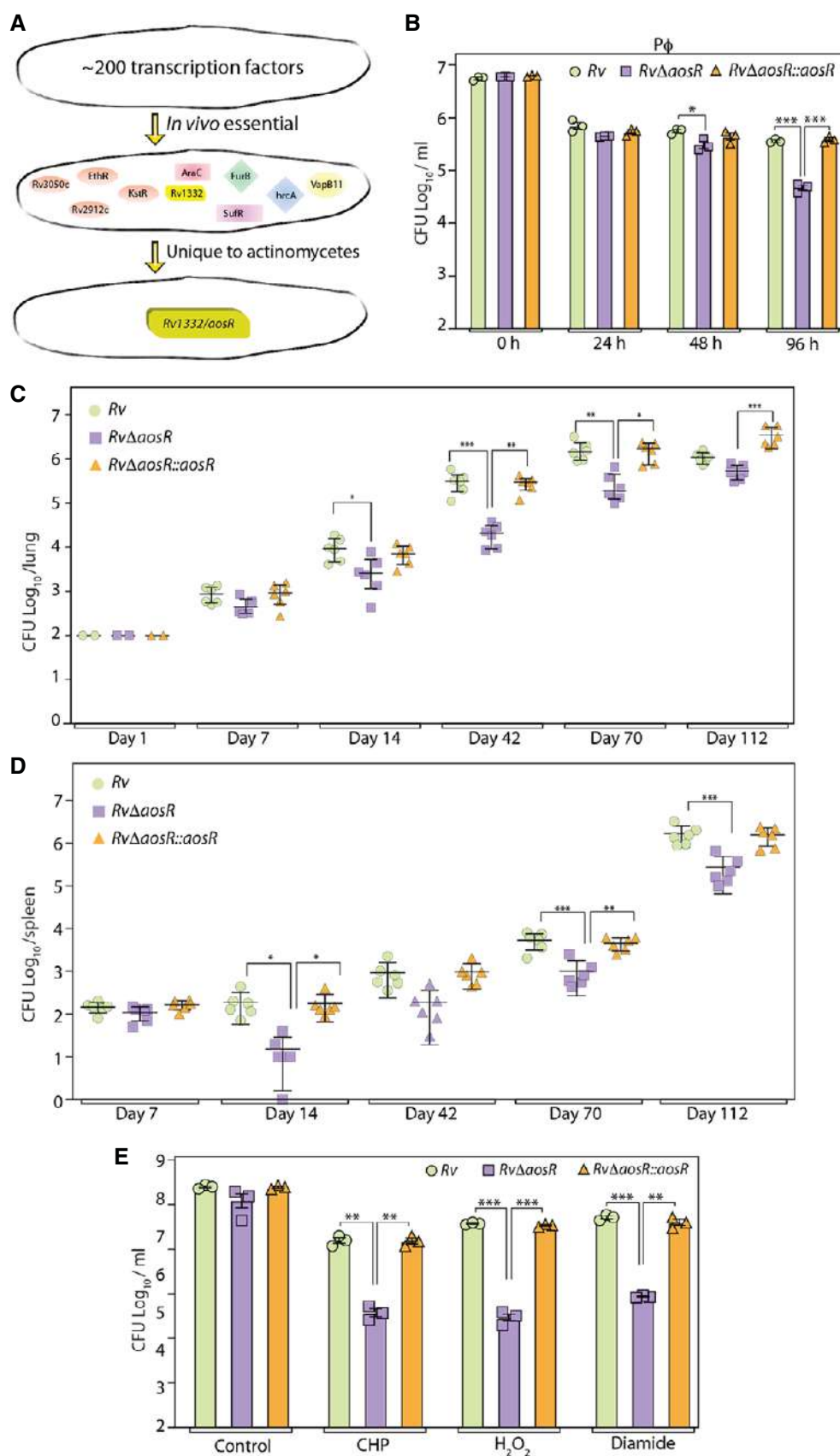
Source data are available online for this figure.

Figure 1.

Table 1. Orthologs of AosR.

Organism	Members
Rhodococcusjostii RHA1	RHA1_RO01440
Gordoniaalkanivorans NBRC 16433	GOALK_078_00080
Mycobacterium colombiense CECT 3035	MCOL_04000
Gordoniapolyisoprenivorans VH2	AFA72901.1
Nocardiacyriacigeorgica GUH-2	NOCYR_1171
Mycobacterium sp. JLS	MJLS_3838
Corynebacteriumefficiens YS-314	HMPREF0290_2449
Corynebacteriumglutamicum ATCC 13032	CG2770, NCGL2428
Mycobacterium marinum M	MMAR_4066
Rhodococcuserythropolis PR4	RER_38830
Mycobacterium smegmatis str. MC^{2}155	MSMEG_4909
Nocardiafarcinica IFM 10152	NFA_10870
Mycobacterium avium subsp. paratuberculosis K-10	MAP_2428C
Mycobacterium leprae TN	ML1166
Corynebacteriumjeikeium K411	JK0494
Frankiaalni ACN14a	FRAAL1497
Mycobacterium gilvum PYR-GCK	MFLV_2350
Mycobacterium vanbaalenii PYR-1	MVAN_4295
Saccharopolysporaerythraea NRRL 2338	SACE_1202
Amycolicicoccussubflavus DQS3-9A1	AS9A_3630
Actinosynnemamirum DSM 43827	AMIR_1006
Saccharomonosporaviridis DSM 43017	SVIR_29220
Nakamurellamultipartita DSM 44233	NAMU_1695
Corynebacteriumurealyticum DSM 7109	CU1471
Tsukamurellapaurometabola DSM 20162	TPAU_1288
Corynebacteriumaccolens ATCC 49725	HMPREF0276_1596
Corynebacteriumlipophiloflavum DSM 44291	HMPREF0298_0966
Corynebacteriumpseudogenitalium ATCC 33035	HMPREF0305_11966
Corynebacterium striatum ATCC 6940	HMPREF0308_0275
Gordoniabronchialis DSM 43247	GBRO_1961
Corynebacteriumaurimucosum ATCC 700975	CAURI_2101
Corynebacteriumglucuronolyticum ATCC 51867	HMPREF0294_1367
Corynebacteriumamycolatum SK46	CORAM0001_1195
Corynebacteriummatruchotii ATCC 14266	HMPREF0299_7141
Mycobacterium kansasii ATCC 12478	MKANA1_010100009241
Mycobacterium abscessus ATCC 19977	MAB_1476
Corynebacteriumgenitalium ATCC 33030	HMPREF0291_11003
Streptomyces sp. AA4	SSMG_06113
Rhodococcusopacus B4	ROP_11490
Segniliparusrotundus DSM 44985	SROT_1516
Gordonianeofelifaecis NRRL B-59395	SCNU_18918
Corynebacteriumkroppenstedtii DSM 44385	CKROP_1403
Corynebacteriumammoniagenes DSM 20306	HMPREF0281_01200
Corynebacteriumresistens DSM 45100	CRES_0430

Table 1 (continued)

Organism	Members
Pseudonocadiadioxanivorans CB1190	PSED_1507
Segniliparusrugosus ATCC BAA-974	HMPREF9336_02788
Rhodococcusequi 103S	REQ_17860
Corynebacteriumdiphtheriae PW8	CDPW8_1828
Mycobacterium rhodesiae NBB3	MYCRHN_3862
Amycolatopsis mediterranei U32	AMED_7716
Mycobacterium tuberculosis H37Rv	RV1332
Corynebacteriumvariabile DSM 44702	CVAR_0731
Mycobacterium sp. JDM601	JDM601_1338
Corynebacteriumpseudotuberculosis I19	CPI19_1669
Corynebacteriumulcerans BR-AD22	CULC22_01834

exacerbated upon the addition of IFNγ (Fig 2B). The differences in survival were nullified when pΦ were isolated from IFNγ$^{-/-}$ mice (Fig 2C). To delineate the role of AosR in mitigating ROS and RNS stress independently or together, the survival of mycobacterial strains was evaluated in pΦ isolated from WT and phox$^{-/-}$ in the presence or absence of iNOS inhibitor. *Rv∆aosR* displayed survival advantages (~7- to 8-fold) in pΦ isolated from phox$^{-/-}$ mice as well as upon the inhibition of iNOS when compared with the WT (Figs 2D and EV4B). However, inhibition of ROS and RNS independently was insufficient to completely abate the survival differences observed between *Rv* and *Rv∆aosR* or *Rv∆aosR* and *Rv∆aosR::aosR* strains (Figs 2D and EV4B). Importantly, inhibition of both ROS and RNS by treating pΦ from phox$^{-/-}$ with iNOS inhibitor completely overcame the survival defects of the *Rv∆aosR* (Figs 2D and EV4B). These results suggest that AosR is critical for mycobacterial defense against both host-derived ROS and RNS. However, this is in contrast with the *in vitro* data, wherein we observed marginal differences in the susceptibility of the *Rv∆aosR* strain upon the addition of DETA-NO (Fig EV3D). We speculate that the discrepancy between *in vitro* and *ex vivo* results is most likely due to the crosstalk between ROS and RNS pathways in the host (Fig EV4A). To validate these findings *in vivo*, we infected WT, phox$^{-/-}$, and IFNγ$^{-/-}$ mice with *Rv*, *Rv∆aosR*, and *Rv∆aosR::aosR* and monitored their survival at 4 weeks p.i. Bacillary survival in the lungs of infected animals at day 1 indicated equal deposition. As observed in Fig 1C, *Rv∆aosR* displayed attenuated survival compared with *Rv* and *Rv∆aosR::aosR* in WT mice at 4 weeks p.i (Figs 2E and EV4C). Importantly, the survival differences between the strains were abolished in phox$^{-/-}$ and IFNγ$^{-/-}$ mice (Figs 2E and EV4C). These results indicate that AosR detoxifies host-derived ROS and RNS facilitating the mycobacterial growth in the host.

AosR rewires the transcriptome in response to oxidative stress

To gain insights into the mechanism by which AosR modulates the cell's response to oxidative stress, RNAseq analyses of *Rv* and *Rv∆aosR* cells in the absence and presence of oxidative stress were carried out (Appendix Fig S1; Dataset EV1–EV5). Compared with the untreated controls, the addition of CHP to *Rv* and *Rv∆aosR* resulted in the differential expression of 301 and 358 genes,
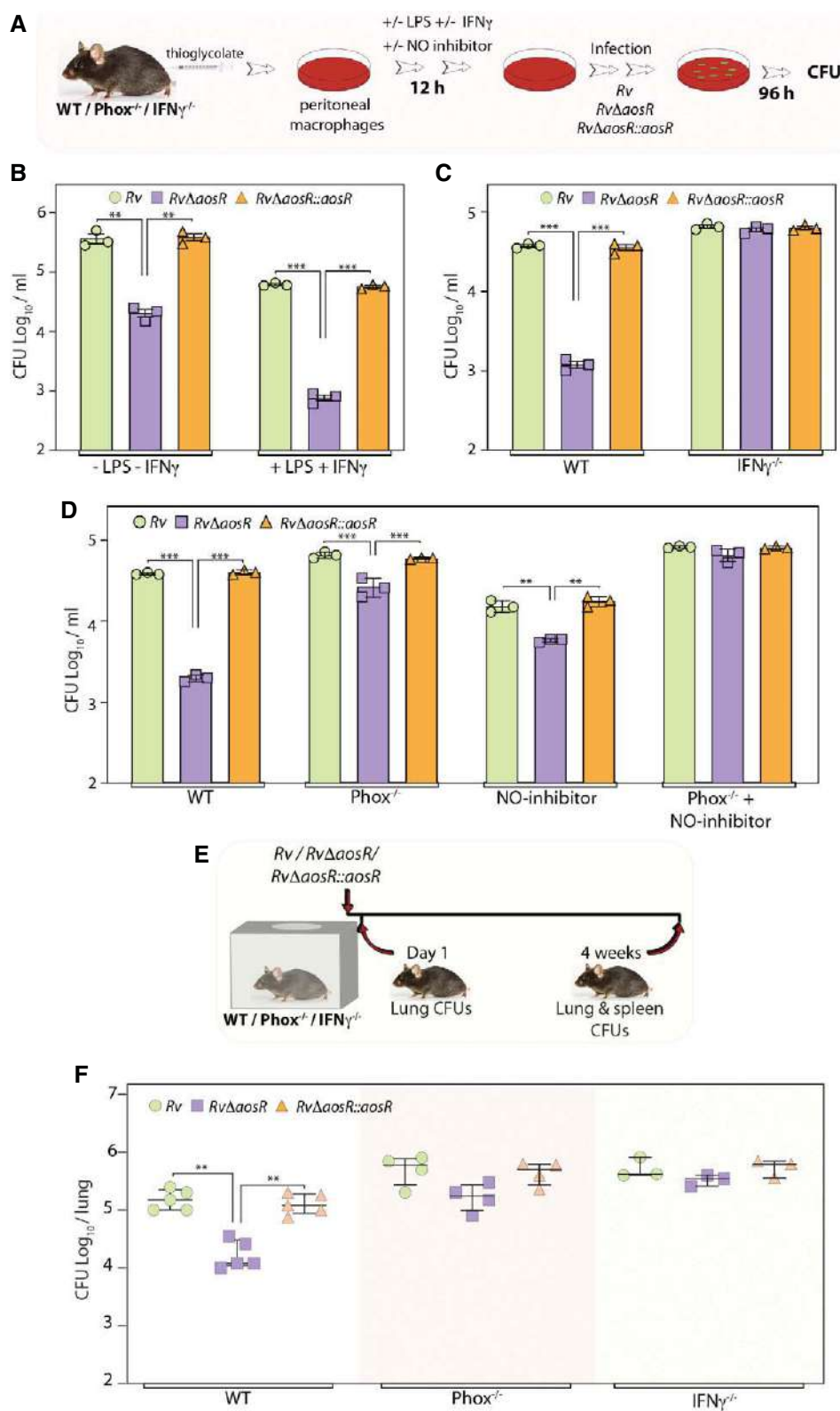
Figure 2.

Figure 2. AosR protects the pathogen from phagocyte-derived reactive oxygen and nitrogen species.

A Schematic outline of pΦ infection experiments. pΦ isolated from C57BL/6, phox$^{-/-}$, IFNγ$^{-/-}$ mice were either left untreated or activated with IFNγ 12 h and LPS for the last 2 h prior to infection. Where indicated, NO inhibitor 1,400 W was added along with IFNγ. The intracellular bacterial viability was enumerated 96 h p.i.

B Untreated and activated pΦ from C57BL/6 mice were infected, and intracellular bacillary survival was monitored 96 h p.i. Data are presented as mean CFU $\log_{10}$/ml $\pm$ SEM and are representative of two biologically independent experiments, each performed in triplicates ($n = 3$).

C, D pΦ isolated from indicated genotypes were activated, and either left untreated or treated with NO inhibitor, 1400W. Intracellular bacillary survival was monitored 96 h p.i. Data are presented as mean CFU $\log_{10}$/ml $\pm$ SEM and are representative of two biologically independent experiments, each performed in triplicates ($n = 3$).

E Schematic outline of murine infection experiments. C57BL/6 ($n = 5$), phox$^{-/-}$ ($n = 4$), IFNγ$^{-/-}$ ($n = 3$) mice were aerosolically challenged with *Rv*, *RvΔaosR*, and *RvΔaosR::aosR* strains.

F Each data point represents $\log_{10}$ CFU/lung of an infected animal, and the error bar depicts the median with interquartile range for each group.

Data information: Statistical significance was drawn in comparison with *RvΔaosR* using one-way ANOVA followed by a *post hoc* test (Tukey test; GraphPad prism).
**$P < 0.005$; ***$P < 0.0005$.
Source data are available online for this figure.

respectively. While we found only 23 genes to be differentially expressed (4 downregulated and 19 upregulated) between both strains under normal growth conditions (Fig 3A and B), the addition of CHP resulted in 434 genes to be differentially modulated. Among these genes, 156 genes overlapped with those that were differentially regulated due to CHP stress in *RvΔaosR* (Fig 3C and Dataset EV3), signifying that their regulation is likely to be independent of AosR (Fig 3D). Excluding these, the stress-responsive AosR regulon thus appears to consist of 278 genes (233 upregulated and 45 downregulated in *Rv* compared with *RvΔaosR*), suggesting AosR to be a probable transcriptional activator (Fig 3E; Dataset EV4). Intermediary metabolism and respiration were the most prominent functional category among the AosR-regulated genes (Fig 3F). We further analyzed these 278 genes to identify the ones that are clustered in the same operon (Appendix Fig S1), as they are likely to be directly regulated by AosR (Dataset EV5). Of the 57 genes that shared an operon with one or more other members of the group, the differential regulation of seven highly upregulated genes and two downregulated genes was further validated by qRT–PCRs (Fig 3G). To confirm that their regulation was indeed AosR-dependent, we analyzed the expression of the same genes in *Rv* and *RvΔaosR* cells treated with CHP (Fig 3H). Up- or downregulation observed in *Rv* upon CHP-induced stress was nullified in CHP-treated *RvΔaosR*, suggesting that the regulation is mediated through AosR. Taken together, global transcriptome profiling suggests that AosR influences the expression of ~6% of *Mtb's* genes in response to oxidative stress.

AosR regulates non-canonical cysteine biosynthesis pathway

In analyzing the differentially expressed genes, of particular intrigue was the observation that *rv1334* was upregulated in *Rv* in response to CHP (Fig 3G) and downregulated in *RvΔaosR* compared with *Rv* in response to CHP (Fig 3H). This gene, also known as *mec*, has been predicted to be a part of an eleven-gene operon (*rv1331* to *rv1341*) that also includes *aosR* (*rv1332*) (Appendix Fig S2A). To confirm the genetic architecture of this predicted operon, we performed RT–PCRs using primer combinations from different genes of the operon and established that *Rv1331-Rv1341* is indeed part of a single operon (Appendix Fig S2B). While the functions of most of the genes of the operon are uncharacterized, genes encoding for *mec, cysO*, and *cysM*, participate in a non-canonical actinomycete-specific cysteine biosynthesis pathway (Fig EV5) (Burns *et al*, 2005). The pathway commences by the transfer of sulfur from a yet unidentified source to the C-terminus of the CysO protein by a reaction catalyzed by the enzyme MoeZ (Rv3206), to form thiocarboxylated CysO (CysO-SH). The CysM protein then utilizes O-phosphoserine and CysO-SH as substrates to catalyze the formation of a CysO-cysteine adduct, which is subsequently cleaved by the protease Mec, to produce cysteine and CysO(Burns *et al*, 2005) (Fig 4A). This is proposed to be the primary route to L-cysteine biosynthesis inside the host (Rengarajan *et al*, 2005; Hatzios & Bertozzi, 2011).

Since genes *rv1331* to *rv1341* are part of the same operon, we hypothesized that during oxidative stress, AosR binds to the operon

Figure 3. AosR rewires transcriptome in response to oxidative stress.

A, B Volcano plots were obtained from DEseq2 analysis across three biological replicates of *Rv* vs *RvΔaosR*. DEGs are highlighted as red dots ($\log_2$ fold change < 1; $P_{adj} < 0.1$). *P* values were calculated using DEseq2, which uses Wald test and were adjusted for multiple testing using Benjamini–Hochberg method. Numbers in top quadrants reveal upregulated (in green) and downregulated (in red) in *Rv* compared with *RvΔaosR*. b. Heat map indicates log2 fold changes in enriched (green) and depleted (red) genes in *Rv* compared with *RvΔaosR*. Color intensity indicates relative higher upregulation and downregulation, respectively.

C Same as (A) under oxidative conditions.

D Venn diagram illustrating the common set of genes between *Rv* and *RvΔaosR* under oxidative conditions compared with *RvΔaosR* in normoxic and oxidative conditions.

E Same as (B) under oxidative conditions. DEGs are clustered according to their functional category. The analysis was performed as explained in Appendix Fig S1.

F Bar graphs depicting the percentage of enriched (green) and depleted (red) DEGs plotted in (E) belonging to a particular functional category.

G, H Relative gene expression of selected DEGs measured by qRT–PCR in *Rv* compared with *Rv* treated with CHP (G) and *Rv* as compared with *RvΔaosR* under oxidative conditions (H). Data were normalized with respect to 16s rRNA, and results are expressed as mean $\log_2$ fold change $\pm$ SD of three independent replicates and are representative of one of two biological replicates.

Data information: Statistical significance was analyzed using Student's *t*-test (two-tailed, unpaired). *$P < 0.05$; **$P < 0.005$; ***$P < 0.0005$.
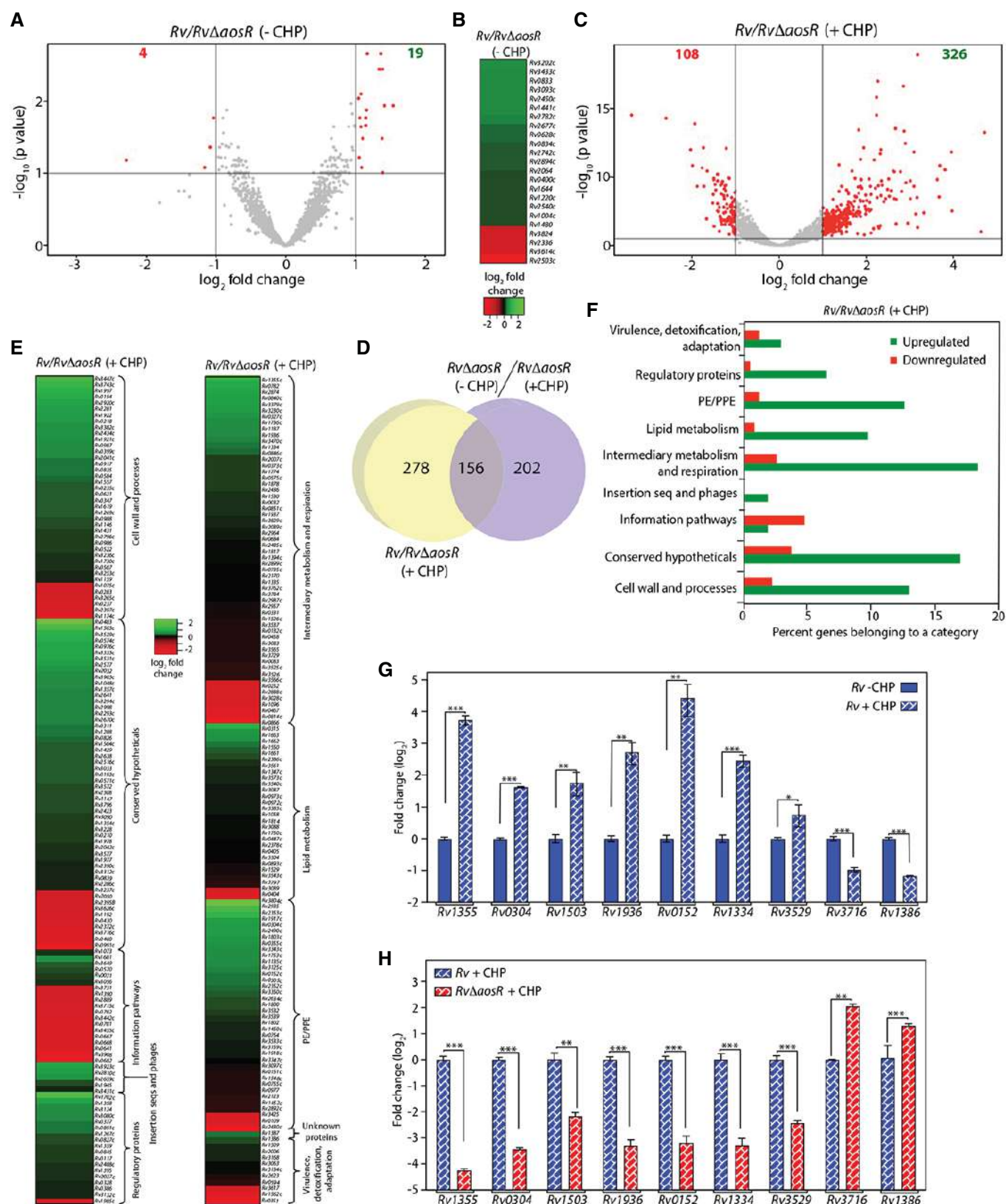Source data are available online for this figure.

Figure 3.

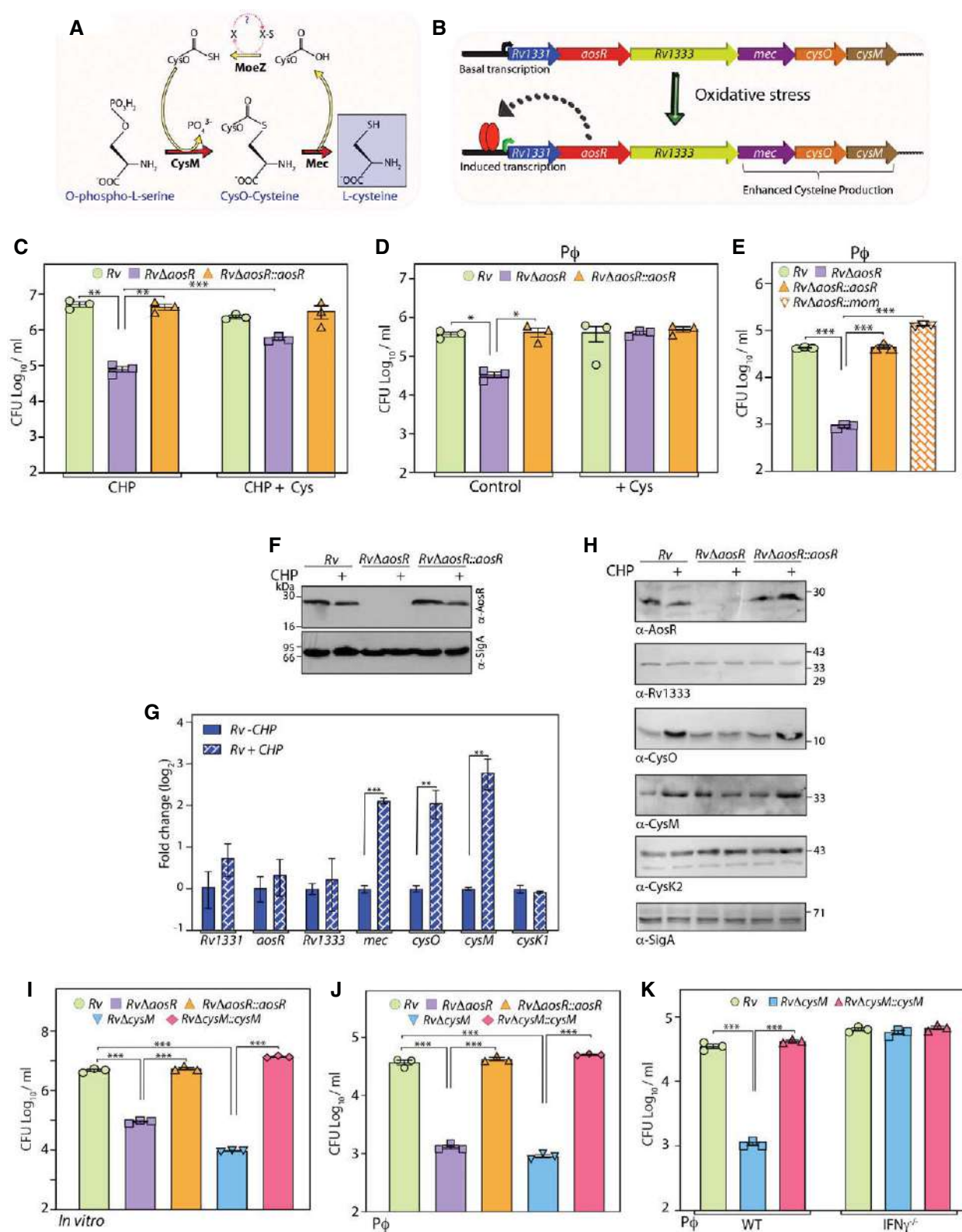Mehak Zahoor Khan et al

Figure 4.

Figure 4. AosR regulates non-canonical cysteine biosynthesis pathway.

A   Non-canonical pathway for cysteine biosynthesis in *Mtb*. MoeZ transfers sulfur from a yet unknown source to the C-terminus of CysO to form thiocarboxylated CysO (CysO-SH). CysM, a non-canonical cysteine synthase, utilizes O-phospho-L-serine (OPS) and CysO-SH as substrates to generate CysO-cysteine adduct, which is cleaved by a protease Mec, to release cysteine and regenerate CysO (Burns *et al*, 2005).

B   Hypothetical model for transcriptional regulation mediated by AosR. Upon oxidative stress, AosR binds to its promoter regulating the entire operon through a positive feedback loop, resulting in higher L-cysteine biosynthesis.

C   Early-log-phase cultures of indicated strains were subjected to 50 μM of CHP for 24 h, in the presence or absence of 1 mM L-cysteine, and CFUs were enumerated (mean ± SEM; $n = 3$).

D   Single-cell suspensions of indicated strains were used to infect pΦ from Balb/C at 1:10 MOI. Cells were either supplemented with 0.2 mM L-cysteine or left untreated, and the CFUs were enumerated 96 h p.i. (mean ± SEM; $n = 3$).

E   pΦ from Balb/C were infected with indicated strains, and bacterial viability was monitored 96 h p.i (mean ± SEM; $n = 3$).

F   35 μg whole-cell lysates (WCL) of *Rv*, *RvΔaosR*, and *RvΔaosR::aosR* subjected to 0 or 50 μM of CHP for 24 h were resolved on 15% SDS–PAGE, transferred to nitrocellulose membrane, and probed with α-AosR and α-SigA antibodies.

G   Relative expression of indicated genes in *Rv* treated with 50 μM CHP for 24 h as compared with *Rv* as measured by qRT–PCR. Data were normalized with respect to 16s rRNA, and results are expressed as mean $\log_2$ fold change ± SD of three independent replicates and are representative of one of two biological replicates. Statistical significance was analyzed using Student's *t*-test (two-tailed, unpaired).

H   WCLs of *Rv*, *RvΔaosR*, and *RvΔaosR::aosR* subjected to 0 or 50 μM of CHP for 6 h were resolved on 15% SDS–PAGE, transferred to nitrocellulose membrane, and probed with indicated antibodies.

I   Early-log-phase cultures of indicated strains were subjected to 50 μM of CHP for 24 h, and the CFUs (mean ± SEM; $n = 3$) were enumerated.

J, K   pΦ from B6 were infected with indicated strains, and intracellular bacterial viability was monitored 96 h p.i (mean ± SEM; $n = 3$).

Data information: (C–E and I–K) Statistical significance was analyzed using one-way ANOVA followed by a *post hoc* test (Tukey test; GraphPad prism). *$P < 0.05$; **$P < 0.005$; ***$P < 0.0005$.

Source data are available online for this figure.

---

promoter upstream of *Rv1331*, thus inducing transcription of the entire operon (Fig 4B). If this were true, one would expect enhanced L-cysteine production, which would lead to the biosynthesis of antioxidants such as mycothiol and ergothioneine. Concordant with this, the addition of L-cysteine to the growth medium rescued the survival defect of *RvΔaosR* both *in vitro* and within pΦ (Fig 4C and D). To negate the possibility of the addition of L-cysteine itself perturbing the redox homeostasis, we examined if overexpression of *mec-cysO-cysM* can complement the *RvΔaosR* phenotype. We found that indeed the overexpression of *mec-cysO-cysM* (*mom*) cluster in the *RvΔaosR* strain could rescue the growth and survival defects both *in vitro* (Appendix Fig S3A) and *ex vivo* (Fig 4E), suggesting that the non-canonical L-cysteine biosynthesis pathway mitigates oxidative stress.

Contrary to the hypothesis that the entire operon might be upregulated under redox stress (Fig 4B), we observed the protein levels of AosR to be unaltered upon CHP treatment (Fig 4F). Moreover, gene expression analysis by qRT–PCR revealed that while *mec*, *cysO*, and *cysM* were significantly upregulated in response to redox stress, there was no difference in the expression of the first three genes of the operon *rv1331-Rv1333* (Fig 4G). While the transcript levels of *mec* and *cysM* peaked at 3 h post-treatment (Appendix Fig S3B), the corresponding protein levels peaked at 6 h post-CHP addition (Appendix Fig S3C). In agreement with the data in Fig 4F, neither transcriptional (Fig 4G) nor translational levels (Appendix Fig S3C) of AosR were altered upon CHP treatment. Most importantly, the expression levels of the other cysteine synthases, CysK1, and CysK2 (Fig EV5), also remained unaltered (Fig 4G and Appendix Fig S3C). Consistent with these results, quantitative analysis of protein levels 6 h post-CHP addition suggested a twofold to threefold increase in CysO and CysM (Appendix Fig S3D and E). Notably, CysO or CysM expression was not enhanced in CHP-treated *RvΔaosR*, a deficiency that was overcome upon complementation with *aosR* (Fig 4H). Taken together, these results supported the conclusion that the induction of CysM and CysO expression in response to oxidative stress is indeed AosR-dependent.

To conclusively demonstrate that *mec-cysO-cysM* augments *Mtb* defense against peroxide stress, we deleted the non-canonical cysteine synthase CysM (*RvΔcysM*) (Appendix Fig 4A and B) and examined its phenotype. The *RvΔcysM* mutant exhibited compromised survival during *in vitro* peroxide stress and within pΦ (Fig 4I and J). The survival defect in response to peroxide was more pronounced in *RvΔcysM* as compared with *RvΔaosR*, likely due to the absence of even basal levels of *cysM* expression. Importantly, similar to *RvΔaosR*, the attenuated survival of *RvΔcysM* was recuperated in pΦ isolated from IFNγ$^{-/-}$ mice (Fig 4K). Collectively, these results indicate that AosR-driven upregulation of *mec-cysO-cysM* combats host-induced stress.

AosR binds to a stress-inducible auxiliary promoter in conjunction with SigH

The results presented above suggested the possibility of an auxiliary AosR-dependent promoter upstream of *mec*, through which *mec-cysO-cysM* expression might be induced upon oxidative stress (Fig 5A). To examine this hypothesis, we fused the 500 bp immediately upstream sequence of the *mec* gene with the *luciferase* gene and analyzed luciferase activity in the absence or presence of CHP in *Rv* and *RvΔaosR*. In contrast to the control *sigA* promoter-*luciferase* construct, which supported *luciferase* expression regardless of the presence of CHP, the *mec* promoter drove *luciferase* expression only upon oxidative stress, suggesting the presence of an inducible auxiliary promoter (Fig 5B; left panel), importantly, while the *mec* promoter-driven luciferase activity could only be detected in *Rv* but not in *RvΔaosR*, indicating AosR to be a positive regulator of this promoter (Fig 5B).

While AosR is necessary for *mec-cysO-cysM* transcriptional activation, it alone might not be sufficient to do so. Thus, to identify an associated factor that contributes to AosR-mediated transcriptional regulation, we examined the AosR interactome. FLAG-AosR was immunoprecipitated (IP) from whole-cell lysates isolated from formaldehyde-treated *RvΔaosR::pN* or *RvΔaosR::pN-aosR* cells, in
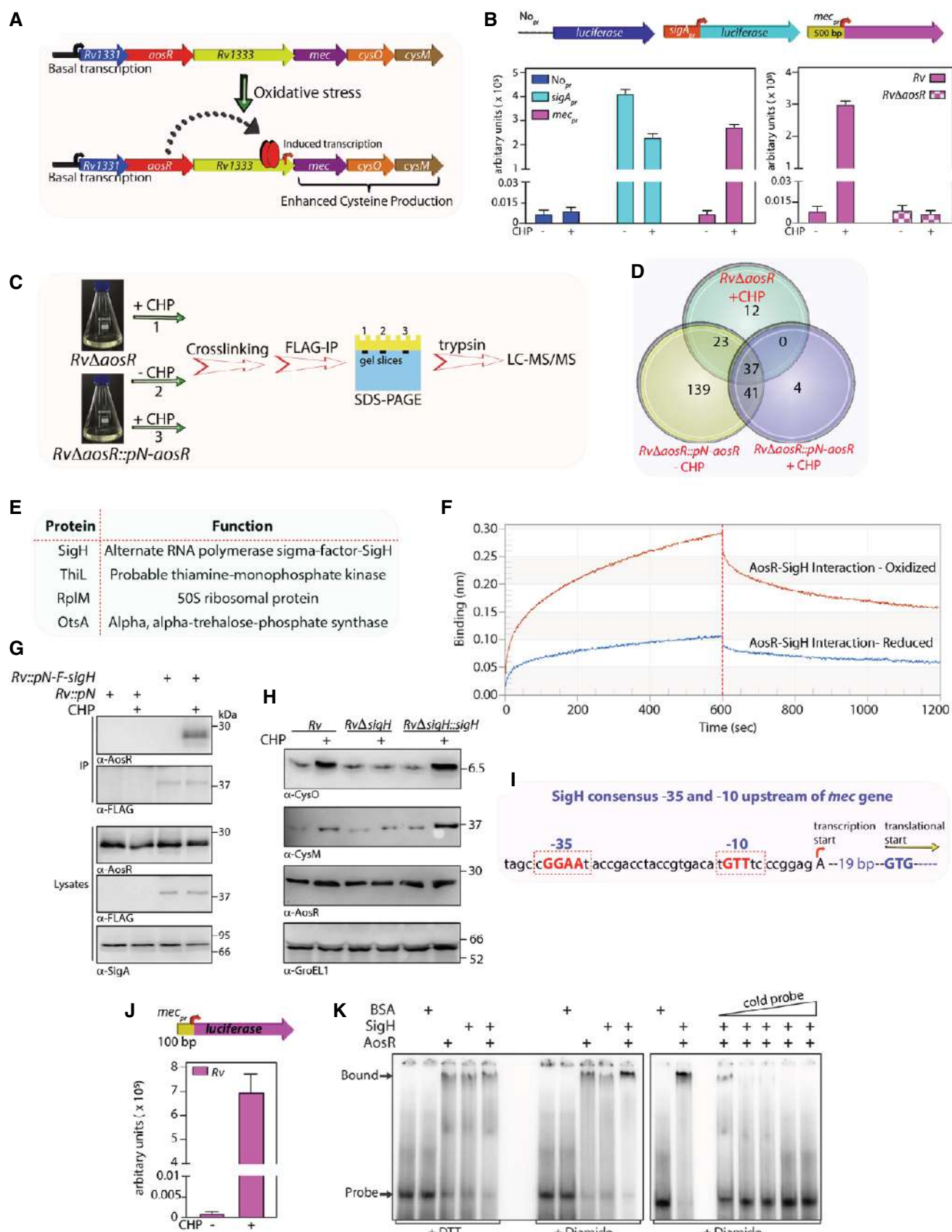
Figure 5.

Figure 5. AosR binds to a stress-inducible auxiliary promoter in conjunction with SigH.

A   Alternate model for the transcriptional regulation mediated by AosR. Upon oxidative stress, AosR regulates auxiliary promoter upstream of *mec-cysO-cysM* resulting in enhanced ʟ-cysteine biosynthesis.

B   The promoter of *sigA* and *mec* was fused to luciferase, and transformed cells were either left untreated or exposed to CHP stress for 6 h and luciferase activity was measured (mean ± SD; *n* = 6)

C   Outline of interactome experiment.

D   Venn diagram illustrating the overlaps among interacting partners found in different conditions.

E   Table listing the proteins that interact with AosR specifically under oxidative stress.

F   BLI sensorgram demonstrating relative binding affinities of 800nM His-AosR to immobilized His-SigH under oxidizing and reducing conditions.

G   *Rv::pN* and *Rv::pN-F-sigH* were either subjected to none or 50 μM of CHP for 6 h followed by cross-linking. 1 mg WCL was used to immunoprecipitate FLAG-SigH, and 1/10th IP was probed with α-FLAG and 9/10th IP with α-AosR. 50 μg WCLs were probed with α-FLAG, α-AosR, and α-SigA as controls.

H   Expression of CysO, CysM, AosR, and GroEL1 (control) was analyzed in WCLs of indicated bacterial strains treated with 0 or 50 μM of CHP for 6 h.

I   SigH-dependent promoter is present upstream of *mec*. The consensus −35 and −10 regions along with TSP are indicated (Sharp *et al*, 2016).

J   100 bp upstream of *mec* was fused to luciferase, and transformed cells were either left untreated or exposed to 50 μM CHP stress for 6 h and luciferase activity was measured (mean ± SD; *n* = 3)

K   5–7.5 × 10⁴ end labeled 100 bp double-stranded oligonucleotide was incubated with no protein (lanes 1 and 6) or 4 μM BSA (lanes 2 and 7) or 2 μM His-AosR + 2 μM BSA (lanes 3 and 8), or 2 μM His-SigH + 2 μM BSA (lanes 4 and 9) or 2 μM His-AosR + 2 μM His-SigH (lanes 5 and 10). The reactions were either incubated in the presence of 10 mM reduced DTT or 10 mM diamide to reduce or oxidize thiols, respectively, and resolved on 8% PAGE gel. Protein–DNA complexes (bound) and free probe are indicated by arrows. To confirm the specificity of DNA–protein interaction, EMSA reaction was performed in the presence of 5, 10, 25, 50, and 100 molar excess of unlabeled 100 bp double-stranded oligonucleotide.

Source data are available online for this figure.

the absence or presence of CHP. The co-immunoprecipitating proteins were identified using mass spectrometry (Fig 5C). As AosR regulates transcription in response to oxidative stress, interacting partners exclusively found in *RvΔaosR::pN-aosR*+CHP were of interest (Fig 5D). Only four proteins fell into this category, and one among these was SigH: an extracytoplasmic-function sigma factor (Fig 5E), known to respond to oxidative stress (Raman *et al*, 2001; Manganelli *et al*, 2002; Sharp *et al*, 2016).

To validate the interaction between SigH and AosR, we performed biolayer interferometry (BLI) with purified proteins. His-SigH protein was immobilized on the sensor, and increasing concentrations of His-AosR were allowed to interact. The binding of AosR to the SigH bound on the biosensor would increase the thickness of the layer on the sensor tip resulting in a wavelength shift that was measured. We found a significant shift in the association curve upon the addition of AosR in a concentration-dependent manner both in reduced and oxidized conditions (Appendix Fig S5A and B). The binding curves thus generated were fitted to a 1:1 binding model, and the equilibrium dissociation constant (Kd) values were calculated under both conditions (Appendix Fig S5A and B). The binding affinity of AosR toward SigH is higher under oxidizing conditions with a Kd value of ~ 300 nM compared with the reducing conditions wherein the Kd value was ~ 3,000 nM. Moreover, the response of the interaction was threefold higher under oxidizing conditions compared with the reducing conditions (Fig 5F). Oxidative-dependent interactions between SigH and AosR were further confirmed by performing a reverse IP wherein FLAG-SigH was found to interact with AosR specifically under oxidizing conditions (Fig 5G). If SigH-AosR interaction is indeed critical for AosR-mediated transcriptional activation of *mec-cysO-cysM*, one would expect that the genetic deletion of *sigH* (*RvΔsigH*) phenocopies the effects observed in *RvΔaosR*. Consistent with this hypothesis, neither CysM nor CysO protein levels were upregulated in *RvΔsigH* mutant upon peroxide stress, suggesting that both AosR and SigH are important for *mec-cysO-cysM* upregulation (Fig 5H).

SigH regulates genes involved in DNA repair, sulfate uptake, cysteine, and molybdopterin biosynthesis in response to heat or oxidative stress (Raman *et al*, 2001; Manganelli *et al*, 2002; Sharp *et al*, 2016). Its deletion compromises the ability of *Mtb* to combat oxidative stress (Manganelli *et al*, 2001, 2002; Raman *et al*, 2001). The SigH regulon identified through ChipSeq (Sharp *et al*, 2016) showed direct binding to the intragenic region upstream of *mec-cysO-cysM* (Fig 5I). Having established that SigH-AosR regulates *mec-cysO-cysM* upon peroxide stress, we next sought to determine whether either or both proteins could directly interact with the promoter region of *mec*. Toward this, we fused 100 bp upstream of *mec-cysO-cysM* harboring the SigH binding sequence identified through ChipSeq (Fig 5I), upstream of *the luciferase* gene. Luciferase activity evaluated in the absence and presence of CHP in *Rv* validated that the auxiliary promoter element necessary for stress-inducible response lies within the 100 bp region (Fig 5J). Next, we performed electrophoretic mobility shift assays (EMSA) with radio-labeled 100 bp fragment to examine the direct binding of AosR and SigH. EMSA indicated that both AosR and SigH bind 100 bp fragment both under reducing and oxidizing conditions. Importantly, the addition of both proteins together resulted in stronger binding under oxidizing conditions, compared with the reduced conditions indicating that the DNA binding is influenced by the redox environment (Fig 5K). We established the specificity of the observed shift in the EMSA by performing competition with fold excess of unlabeled 100 bp fragment (Fig 5K). Collectively, these results suggest that AosR and SigH are independently essential for the regulation of non-canonical cysteine biosynthesis pathway and that the two factors come together in the cell's response to oxidative stress, acting concertedly to activate transcription of the *mom* cluster.

Intracellular redox status governs activation of AosR

The alignment of the amino acid sequences of AosR from various mycobacterial species highlights the well-conserved primary sequence of this protein. Interestingly, while the DUF2017 domain is conserved in all orthologs, only two mycobacterium *sps.*, namely *Mtb* and *M. bovis*, encode for an extended N-terminus of 22 amino acid length (Fig 6A). The N-terminal region is largely unstructured
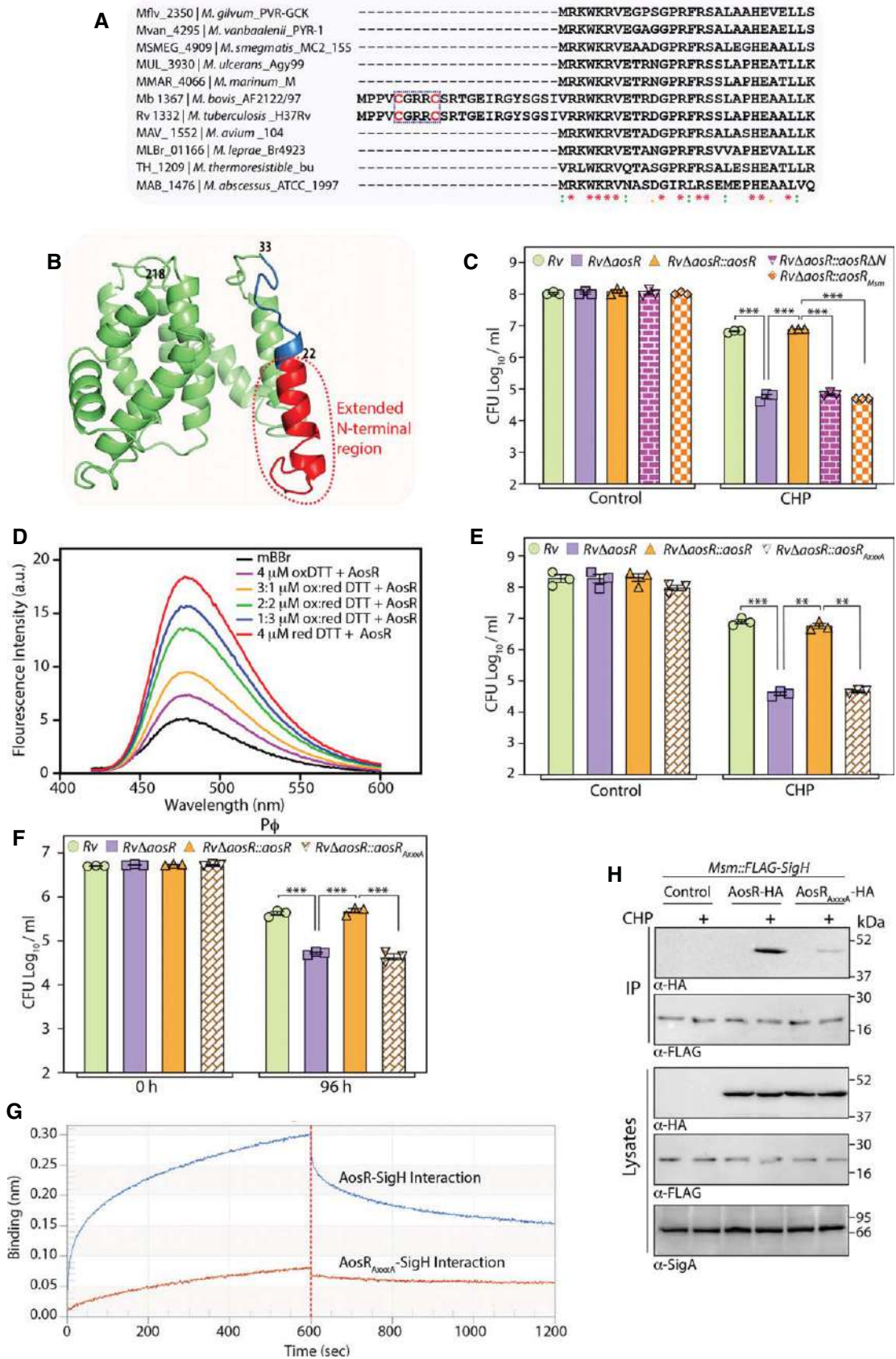
Figure 6.

Figure 6. Intracellular redox status governs activation of AosR.

A   Multiple sequence alignment of AosR from various mycobacterial species. CxxxC motif present within the N-terminus extension is highlighted using a blue box.
     ✳ perfect alignment ⦂ strong similarity and ᐧ represents weak similarity.
B   Secondary structure model of AosR predicted by I-Tasser Web server.
C   Early-log-phase cultures of indicated strains were subjected to 50 μM of CHP for 24 h, and CFUs were enumerated (mean ± SEM; $n = 3$). Control represents untreated cells.
D   1 μM AosR was treated with various ratios of oxidized to reduced DTT (ox:red DTT- 3:1, 2:2, 1:3), or only with 4 μM reduced or oxidized DTT. mBBr was added to the reaction mixture, and the fluorescence intensity was measured from 430–600 nm upon excitation at 390 nm wavelength. Reaction mixture without any protein was used as blank (mBBr). Each spectrum represents an average of three individual scans.
E   Early-log-phase cultures of indicated strains were subjected to 50 μM of CHP for 24 h, and CFUs were enumerated (mean ± SEM; $n = 3$). Control represents untreated cells.
F   pΦ from Balb/C were infected with indicated strains, and bacterial viability was monitored 0 and 96 h p.i. Data are presented as mean CFU $\log_{10}$/ml ± SEM and are representative of two biologically independent experiments, each performed in triplicates ($n = 3$).
G   BLI sensorgram illustrating relative binding affinities of 800 nM His-AosR and His-AosR$_{AxxxA}$ to immobilized His-SigH under oxidizing conditions.
H   *Msm::FLAG-SigH, Msm::FLAG-SigH-AosR-HA*, and *Msm::FLAG-SigH-AosR$_{AxxxA}$-HA* were either subjected to none or 50 μM of CHP for 3 h followed by cross-linking. 1 mg WCL was used to immunoprecipitate FLAG-SigH, and $1/10^{th}$ IP was probed with α-FLAG and $9/10^{th}$ IP with α-HA. 50 μg WCLs were probed with α-FLAG, α-HA, and α-SigA as controls.

Data information: Statistical significance was analyzed using one-way ANOVA followed by a *post hoc* test (Tukey test; GraphPad prism). **$P < 0.005$; ***$P < 0.0005$.
Source data are available online for this figure.

up to 33 amino acids except for a helix-turn-helix motif (Fig 6B). To evaluate the importance of the N-terminal region, we complemented *RvΔaosR* with either AosR lacking the N-terminal 22 aa (*RvΔaosR::aosRΔN*) or with an AosR ortholog from *M. smegmatis* (*RvΔaosR::aosR$_{Msm}$*), which does not have the extended N-terminus region (Fig 6C). While the expression of full-length AosR$_{Mtb}$ rescued the survival defects of *RvΔaosR* under oxidative stress, neither AosR::ΔN nor AosR$_{Msm}$ rescued the defective phenotype, highlighting the importance of the N-terminal region in mediating AosR function during oxidative stress (Fig 6C).

Examination of the primary amino acid sequence of the N-terminus extension revealed the presence of a CxxxC motif (Fig 6A). Further analysis revealed an intriguing fact that these are the only cysteine residues in the protein. CxxC/CxxxC motifs are ubiquitously found in redox-sensitive TFs including WhiB$_{Mtb}$ proteins that respond to O$_2$/NO, RsrA$_{Mtb}$, and Spx of *B. subtilis* that sense diamide, CatR of *S. coelicolor*, and FurS of *S. reticuli* that sense H$_2$O$_2$/diamide(Hillion & Antelmann, 2015). The ability of cysteines to form a disulfide bond in response to an oxidizing cellular environment may lead to the release of a metal ion coordinated by the cysteines, triggering a conformational change, which may, in turn, modulate their interactions with other proteins. Hence, we first assessed the oligomeric state of His-AosR through gel-filtration chromatography and found it to be a dimer (Appendix Fig S6). However, His-AosR$_{AxxxA}$ (wherein cysteines were mutated to alanines) also eluted as a dimer in GFC (Appendix Fig S6), suggesting that the CxxxC motif does not participate in dimer formation. Exposure to oxidants not only affects cysteine but also oxidizes several other amino acids including tyrosine, tryptophan, histidine, and methionine, which may influence oligomerization of the protein. Thus, we examined the dependence of AosR dimerization status on the redox environment. His-AosR, His-AosR$_{AxxxA}$, and His-AosR$_{Msm}$ eluted as dimers independent of the oxidizing nature of the environment (Appendix Fig S6). In line with this, analysis using the ClusPro protein–protein docking webserver predicted that the two chains of AosR interact through the C-terminal region. To investigate whether the two cysteine residues of the CxxxC motif form an intrasubunit disulfide bond, the recombinant AosR protein was incubated in monobromobimane (mBBr). mBBr reacts with the free thiol group

and results in the formation of an adduct that displays fluorescence, with a direct correlation between the intensity and the number of thiol groups. As observed in Fig 6D, an increasing ratio of reduced to oxidized DTT was coupled to an increase in fluorescence, suggesting that these cysteines participate in the formation of an intrasubunit disulfide bond that is attenuable in response to the external redox environment (Fig 6D).

Next, we examined the ability of the mutated protein AosR$_{AxxxA}$ to rescue the growth defects of the *RvΔaosR*. While the mutations did not affect AosR expression, it failed to rescue the survival defects of *RvΔaosR* both *in vitro* (Fig 6E) and in pΦ (Fig 6F). To understand the underlying mechanism, we tested whether CxxxC residues are important for the interaction of AosR to SigH. BLI experiments indicated while His-AosR could bind to His-SigH under oxidizing conditions, His-AosR$_{AxxxA}$ failed to do so (Fig 6G). To validate that these cysteine residues are indeed important for interaction in mycobacterial cells, FLAG-SigH was immunoprecipitated from *M. smegmatis* electroporated with pN-F-SigH and pS-AosR-HA$_{WT/mut}$. It is apparent from the data that the interaction of AosR with SigH could only be detected upon peroxide stress and mutation of CxxxC significantly reduced the affinity (Fig 6H). These results validate the importance of the redox environment as well as the CxxxC motif of AosR in mediating AosR-SigH interaction, which in turn is important for combating host-induced peroxide stress.

AosR is crucial for cellular-redox homeostasis

Cysteine-derived molecules such as mycothiol, ergothioneine, H$_2$S, and other Fe-S cluster-containing proteins alleviate oxidative stress (Rawat *et al*, 2004; Shatalin *et al*, 2011; Saini *et al*, 2016; Mishra *et al*, 2019). To investigate whether AosR-mediated regulation indeed influences cysteine-derived molecules, we estimated the free thiol protein content in *Rv, RvΔaosR,* and *RvΔaosR::aosR* under normal and oxidized conditions. As shown in Fig 7A, we observed a ~ 3-fold increase in the thiol content of *Rv* and *RvΔaosR::aosR* in oxidatively stressed cells compared with respective control groups. Importantly, the increase in thiol was found to be dependent on AosR (Fig 7A). Next, we quantified cysteine-derived highly abundant low molecular thiols, mycothiol, and ergothioneine using
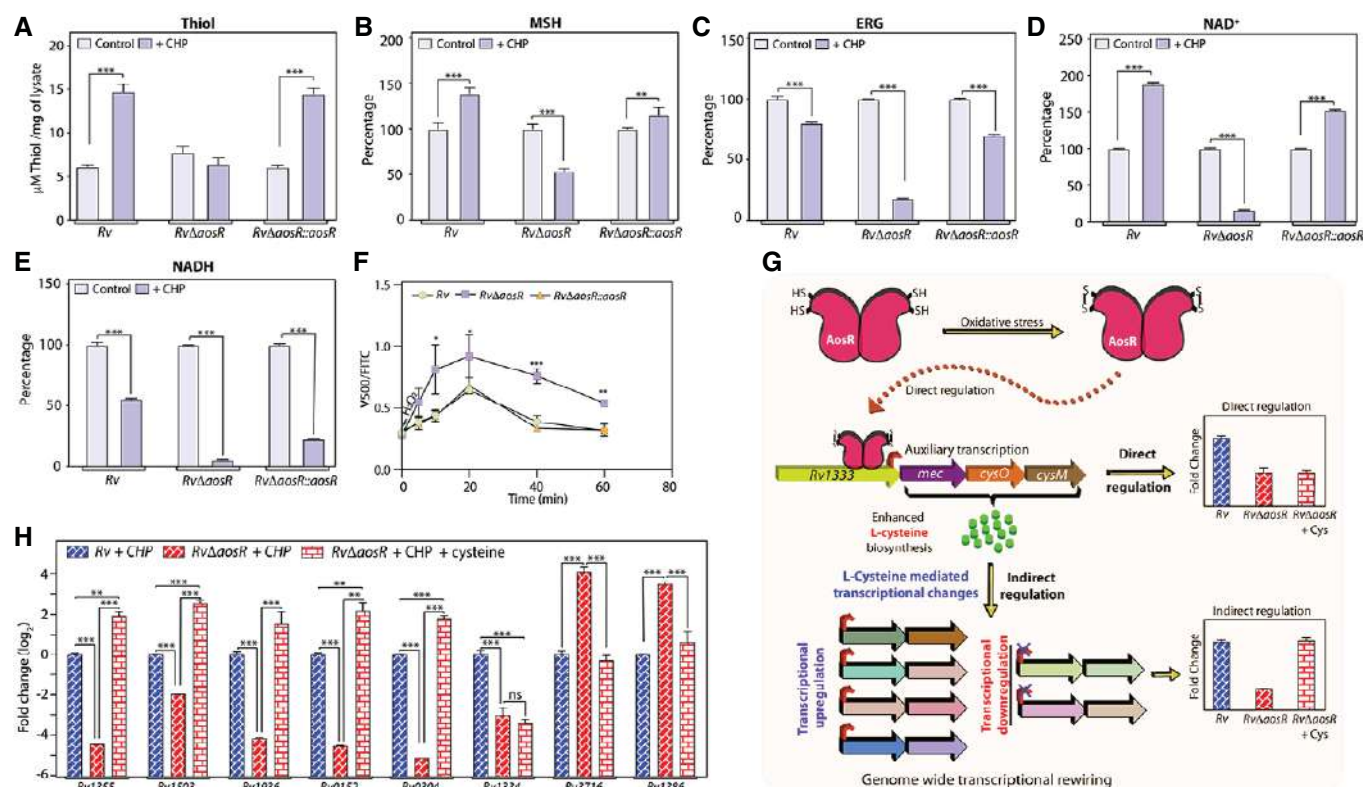
Figure 7. AosR is crucial for cellular-redox homeostasis.

A   Indicated bacterial strains were subjected to oxidative stress with 50 μM CHP for 6 h, and free thiol content was quantified. Data presented are representative of one of two biological replicates, each performed in triplicates ($n = 3$). Y-axis represents μM thiol/μg of WCL (mean ± SD).

B–E   Metabolite levels of reduced mycothiol, MSH (B) ergothioneine, ERG (C) NAD$^+$ (D) NADH (E) were measured in *Rv*, *RvΔaosR*, and *RvΔaosR::aosR* in normal and CHP stressed cells using LC-MRM MS/MS analysis. The absolute values obtained under normal conditions were normalized to 100% for each strain, and the relative values were calculated for samples processed from CHP-treated cells. The data indicate relative levels of metabolites (mean percent ± SD) of four replicates ($n = 4$).

F   To evaluate the contribution of AosR on the antioxidant capacity; *Rv*, *RvΔaosR*, and *RvΔaosR::aosR* cells were treated with 5 mM H$_2$O$_2$ and the ratiometric response (mean ± SD; $n = 3$) was measured at indicated time points.

G   Schematic depicting the pleiotropic role of AosR. Oxidative environment induces disulfide bond formation in AosR and transcription of *mec-cysO-cysM* through an auxiliary promoter resulting in enhanced L-cysteine biosynthesis. This further induces genome-wide transcriptome changes. The latter set of changes in indirectly regulated genes can be mitigated by the addition of L-cysteine in the media.

H   qRT–PCR measurements for the log$_2$ fold induction (mean ± SD, $n = 3$) for indicated genes in *RvΔaosR* and *RvΔaosR* treated with 1 mM L-cysteine as compared with *Rv*. All strains were treated with 50 μM CHP. Data were normalized with respect to 16s rRNA and were representative of one of two biological replicates.

Data information: Statistical significance was analyzed using Student's *t*-test (two-tailed, unpaired). *$P < 0.05$; **$P < 0.005$; ***$P < 0.0005$, ns = non-significant.
Source data are available online for this figure.

LC-MRM MS/MS analysis. The MSH levels were found to be similar in *Rv*, *RvΔaosR*, and *RvΔaosR::aosR* under normal conditions. While the addition of CHP resulted in ~30 and 15% and an increase in the MSH levels in *Rv* and *RvΔaosR::aosR*, we observed a ~ 50% decrease in *RvΔaosR*, indicating *Mtb* is unable to replenish MSH in the absence of AosR (Fig 7B). Similarly, levels of ergothioneine were found to be drastically lower in *RvΔaosR* (18%) as compared to *Rv* (~ 80%) and *RvΔaosR::aosR* (~ 70%) upon oxidative stress (Fig 7C). Consequently, the levels of redox cofactors NAD and NADH were also found to be lower in *RvΔaosR*, probably a metabolic consequence of death (Fig 7D and E). Next, we monitored the antioxidant response of *Rv*, *RvΔaosR*, and *RvΔaosR::aosR* by measuring changes in mycothiol redox potential (E$_{MSH}$) using a non-invasive, highly sensitive redox biosensor specific to mycobacteria

(Bhaskar *et al*, 2014). Redox status of *RvΔaosR* undergoes a more drastic shift upon exposure to oxidative stress compared with *Rv* and *RvΔaosR::aosR*. Moreover, while *Rv* and *RvΔaosR::aosR* were able to return to its ambient redox state within 60 min, *RvΔaosR* failed to do so (Fig 7F). Together, the data suggest that AosR is crucial in maintaining intra-mycobacterial redox homeostasis.

We have shown that either overexpression of *mec-cysO-cysM* or the addition of L-cysteine rescues the survival defects of *RvΔaosR* in response to oxidative stress (Fig 4). Moreover, these defects were mirrored in *RvΔcysM* (Fig 4), suggesting that the upregulation of the *mec-cysO-cysM* gene cluster might be the sole function of AosR *prima facie*. This hypothesis is divergent from the RNAseq data, which showed that under oxidative stress AosR regulates ~ 6% of the *Mtb* transcriptome (Fig 3). Thus, we propose that in addition to

directly modulating the *mec-cysO-cysM* gene cluster, AosR indirectly influences the expression of a larger set of genes as a result of L-cysteine deprivation and consequent redox imbalance (Fig 7G). If this is indeed true, the addition of the metabolic product L-cysteine should rescue the differential expression of indirectly regulated genes. Thus, we evaluated the expression profiles of previously validated genes (Fig 3) in *Rv*+CHP, *RvΔaosR*+CHP, and *RvΔaosR*+CHP+L-cysteine. The differential expression pattern between *Rv*+CHP and *RvΔaosR*+CHP for all nine genes was in line with data in Fig 3G. The addition of L-cysteine mitigated the expression differences of 8 genes: all except *mec*, suggesting that transcriptional modulation of *mec-cysO-cysM* is upstream of the metabolic consequences of redox perturbations (Fig 7H). Thus, failure of *RvΔaosR* to upregulate cysteine biosynthesis during oxidative stress ensues a domino effect, causing differential expression of 6% of *Mtb* genes resulting in attenuated survival (Fig 8).

Discussion

Bacterial transcription factors SoxR, OxyR, and FNR act as the primary sensors during NO and O_2 linked metabolic adaptation. However, functional orthologs of OxyR, SoxR, and FNR have not been identified in *Mtb*, indicating that *Mtb* may respond to oxidative stress differently (Deretic *et al,* 1995). Identification of oxidative stress-responsive transcriptional modulators in *Mtb* is largely based on sequence homology. The sigma factors SigH, SigB, and SigE, the two-component signaling systems SenX-RegX and DosS-DosT/DosR, as well as proteins WhiB3, WhiB4, and WhiB7, are among the well-characterized redox-sensing TFs (Manganelli *et al,* 2001, 2002; Kumar *et al,* 2007; Singh *et al,* 2009; Burian *et al,* 2012; Chawla *et al,* 2012; Singh & Kumar, 2015). In addition, antioxidant enzymes, cell wall-associated lipids, and the membrane-associated oxidoreductase complex act concertedly to neutralize the host-
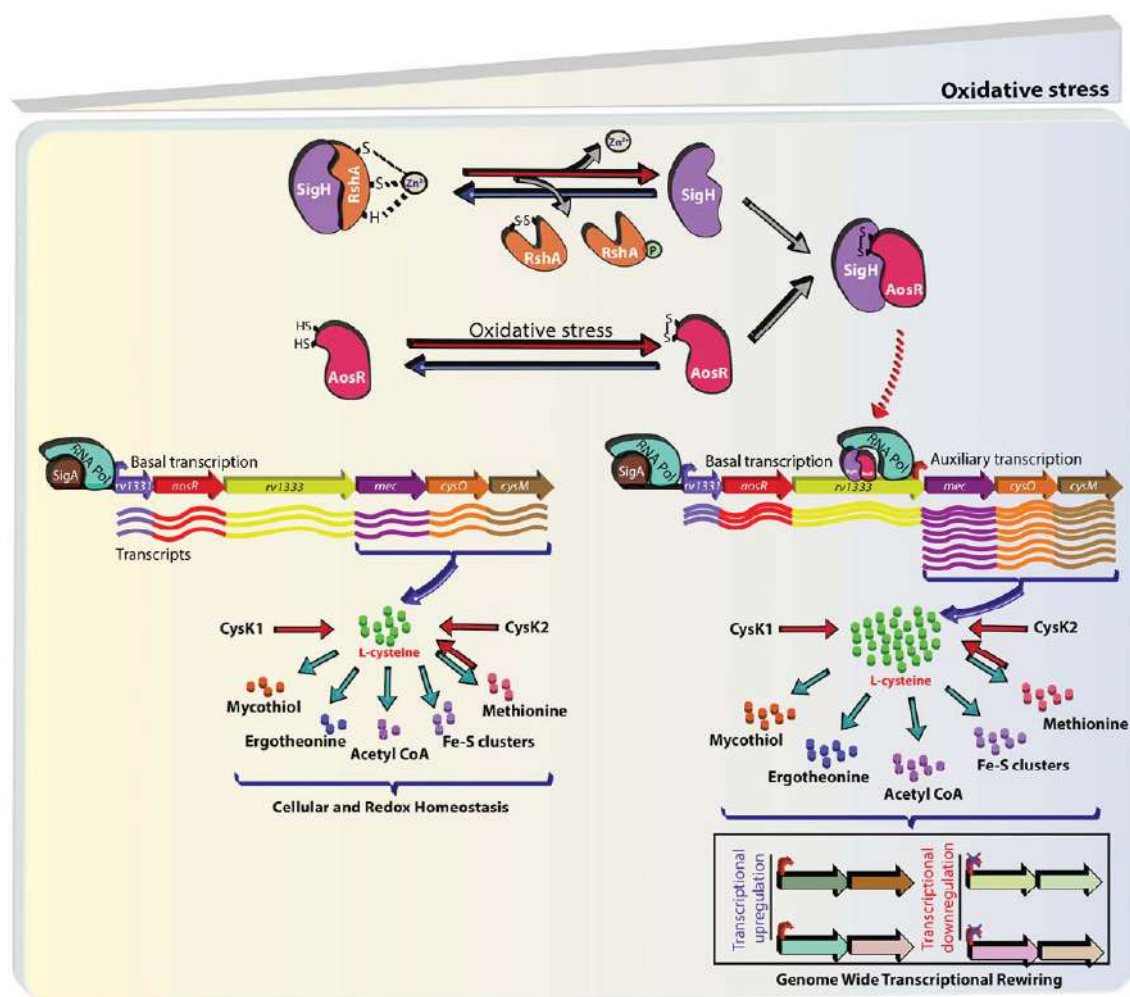

Figure 8. Model depicting the proposed role of AosR during oxidative stress.

In response to oxidative stress, SigH is liberated from its cognate anti-sigma factor (RshA) and an intramolecular disulfide bond is formed in the AosR (Fig 6D). This subsequently results in oxidative stress-dependent interaction between AosR and SigH (Fig 5F and G) that together binds to an auxiliary promoter upstream of *mec* (Fig 5J and K). Increased transcription of *mec-cysO-cysM* (Fig 4G) results in enhanced production of cysteine-derived antioxidant molecules (Fig 7A–C). Increased production of cysteine through non-canonical cysteine biosynthesis protects mycobacteria cells from phagocyte-derived oxidative and nitrosative stress (Fig 2). Inhibition of this redox-regulatory circuit results in genome-wide transcription changes (Figs 3 and 7H).

derived ROS (Edwards *et al*, 2001; Piddington *et al*, 2001; Nambi *et al*, 2015). Despite the identification of various enzymes that help *Mtb* withstand the oxidative and nitrosative insult, the transcriptional regulatory events that coordinate *Mtb's* response during redox stress are poorly understood. Here, we have employed an integrated approach involving genetics, transcriptomics, biophysical analyses, metabolite quantitation, *ex vivo*, and *in vivo* infections to uncover a redox-sensitive network regulated by a novel transcription factor, AosR, which facilitates bacterial adaptation to an inimical environment during oxidative stress.

The survival of *RvΔaosR* in murine lungs and spleen was comparable to wild type up to 2 weeks after the initiation of infection. This could be either due to the sufficient presence of reduced sulfur metabolites, or the mutant's ability to scavenge sulfated moieties from the host. With the progression of murine infection, enhanced recruitment of pro-inflammatory cells increases the levels of ROS and RNI (Nathan *et al*, 1983; Ehrt *et al*, 2001). At this stage, *RvΔaosR* fails to surmount the higher concentration of ROS and RNI generated by the host and thus shows compromised growth (Fig 1C–E). The phenotype observed was similar to what was found upon the deletion of the 5'APS reductase, CysH (Senaratne *et al*, 2006). In contrary to attenuated growth *in vivo*, the mutant exhibited decline in CFUs in the peritoneal macrophages. This apparent discrepancy in phenotype observed with *ex vivo* and *in vivo* infection experiments might probably due to the pre-activated status of peritoneal macrophages. Data show that the attenuated growth of *RvΔaosR* is mitigated in *phox*$^{-/-}$ and *Ifnγ*$^{-/-}$ mice (Fig 2E), confirming the specific requirement of this pathway in response to host-induced oxidative stress. Restricted amounts of sulfated moieties in *RvΔaosR* inside the host may limit its ability to withstand host-generated oxidative and nitrosative radicals and hence result in attenuated survival. This is corroborated by the ability of L-cysteine supplementation or overexpression of Mec-CysO-CysM to reverse *RvΔaosR* susceptibility to oxidative stress (Fig 4C–E). Moreover, the phenotype of *RvΔaosR* is mirrored in *RvΔcysM* (Fig 4I–K), confirming that observed protection against oxidative stress by AosR is due to the regulation of the genes of CysM-dependent pathway.

Mtb encodes for three cysteine synthases—CysK1, CysK2, and CysM (Fig EV5), with 22–36% sequence identity among them (Appendix Fig S7). In addition to this, *Mtb* can also synthesize cysteine from methionine through the reverse trans-sulfuration pathway (Wheeler *et al*, 2005). However, the relative contributions of these biosynthetic pathways and their regulation are yet unknown. It is presumed that during regular growth conditions cysteine biosynthesis relies primarily on the classical CysK1 pathway, whereas CysM-driven biosynthesis operates in the phagosomal environment of the host (Brunner *et al*, 2016). Transcriptome profiles reveal the upregulation of all CysM pathway genes—*mec*, *cysO*, and *cysM* under oxidative stress (Manganelli *et al*, 2002; Voskuil *et al*, 2011). This is consistent with our RNAseq analysis, wherein we observe the upregulation of *mec* and *cysO* in *Rv* upon CHP stress (Fig 3). In other bacteria, L-cysteine biosynthesis is regulated by TFs such as CysB, CymR, and McbR at multiple nodes (Kredich, 1992; Rey *et al*, 2003; Even *et al*, 2006). Interestingly, similar transcriptional regulators have not been identified in mycobacteria. The RNAseq and qRT–PCR data presented in Fig 3 establish that the regulation of the CysM-dependent L-cysteine biosynthesis pathway

is mediated by the transcription factor AosR, which is encoded by the same operon.

While CysK1 and CysK2 transcript and protein levels did not alter under CHP-induced stress, we found CysM to be upregulated under these conditions (Fig 4G and K). Our study suggests that in response to the aggravating conditions inside the host *Mtb* elects to upregulate L-cysteine biosynthesis specifically through the CysM pathway. This could be due to the higher stability of its acceptor substrate O-phospho-L-serine compared with the CysK1 substrate O-acetyl-L-serine (Agren *et al*, 2008), and higher resistance of donor thiocarboxylates to oxidation compared with thiols, the sulfur donor of CysK1 (Burns *et al*, 2005). In accordance with this, transposon mutants with insertions in *mec*, *cysO*, and *cysM* exhibit attenuated survival inside the host (Sassetti & Rubin, 2003; Rengarajan *et al*, 2005; Agren *et al*, 2008). Our findings are incongruent with a recently published study that showed the survival of *Mtb* during *in vitro* oxidative stress to be unaffected by the deletion of *mec-cysO-cysM* (Burns-Huang & Mundhra, 2019). This could be due to the presence of catalase in the broth and agar that quenches oxidative radicals, or different experimental conditions such as the concentrations of the oxidant and the duration of exposure to the oxidizing conditions. However, the study also reported the *mec-cysO-cysM* cluster to be essential upon clofazimine (a peroxide-producing drug) (Burns-Huang & Mundhra, 2019). Taken together, we conclude that Mec-CysO-CysM mitigates exogenous and host-derived oxidative stress, which would also explain the selective essential nature of AosR *in vivo* (Figs 1 and EV2).

Sharp *et al* (2016) performed ChipSeq of SigH$_{Mtb}$ and showed that it regulates genes involved in thiol metabolism including enzymes involved in sulfur uptake and cysteine and molybdopterin biosynthesis. Interestingly, the authors noted a discrepancy between their ChipSeq and qRT–PCR expression data, which was suggested to be due to interactions with stress-specific co-regulators (Sharp *et al*, 2016). Our data fit well with this observation: the interaction of SigH and AosR specifically under oxidative stress. Even though we observed only ~ 10-fold lower affinity of SigH-AosR in reduced compared with oxidative conditions (Fig 5F), it is important to note that mycobacterial cells inhibit SigH-AosR interaction under normal conditions through spatial regulation. SigH is liberated free from its cognate anti-sigma factor, RshA, only upon oxidative stress. This is reflected in our IP data wherein we found interaction specifically under oxidative stress (Fig 5G). This additional layer of stringency could be important to protect the precarious redox state of *Mtb*, especially due to the high toxicity and reactivity of L-cysteine. SigH and AosR together bound to 100 bp upstream of *mec* Fig 5J), resulting in *mec-cysO-cysM* transcription that was abrogated upon deletion of either *aosR* or *sigH* (Figs 4H and 5H).

Redox-responsive proteins such as PknG, WhiB, RsrA, and Trx possess CxxC/CxxxC motifs (Hillion & Antelmann, 2015). A reversible disulfide bond is formed between the cysteine residues of the motif in response to the external redox environment, triggering conformational changes that result in their activation. In consonance with this, we found that mutation of the CxxxC motif present in the unique N-terminal extension of AosR$_{Mtb}$ failed to rescue the *RvΔaosR* defective phenotypes (Fig 6C and E). Importantly, cysteine residues of the CxxxC motif are capable of forming intrasubunit disulfide bonds in an oxidizing environment (Fig 6D), suggesting that the formation of a bridge between these residues in AosR,

which in turn is important for SigH-AosR interaction (Fig 6G and H). In accordance with this, RNAseq analysis revealed ~ 6% of *Mtb* genes are regulated by AosR in response to oxidative stress (Fig 3).

Cysteine is the source of sulfur for multiple cellular components including biotin, lipoic acid, coenzyme A, methionine, molybdopterin, thiamine, and Fe-S clusters. Importantly, the redox-active moiety of the major cytosolic redox buffers—mycothiol and ergothioneine—is also derived from cysteine. Interestingly, an excess concentration of L-cysteine is cytotoxic, and hence, multiple bacteria utilize cysteine-inducible cysteine-specific efflux pumps for its export (Dassler *et al*, 2000; Franke *et al*, 2003; Takumi & Nonaka, 2016). However, such transporters have not been identified in *Mtb*, indicating that the regulation could be at the level of biosynthesis and through metabolic redistribution. This is also in line with the finding that the intracellular concentration of L-cysteine in *Mtb* is limiting in comparison with other amino acids (Laxman *et al*, 2013). Thus, our efforts to measure cysteine through commercially available kits and mass spectrometry were unsuccessful. In response to the increased need for antioxidant molecules in hostile conditions such as oxidative stress, *Mtb* actively upregulates CysM-dependent L-cysteine biosynthesis through AosR and SigH, which in turn enhances the production of cysteine-derived antioxidants including mycothiol and ergothioneine (Fig 7B and C). Inhibition of this redox-regulatory pathway leads to an extensive pleiotropic effect affecting multiple biological processes (Fig 7G and H). Collectively, this study broadens our understanding of how *Mtb* employs unique transcriptional networks and metabolic pathways to self-serve its nutritional needs while effectively combating the host immune system (Fig 8). The apparent essentiality of the numerous metabolic products and the absence of cysteine synthases in humans showcase the vulnerability of this pathogen pathway that can be exploited to develop anti-mycobacterial drugs. We propose that this newly discovered regulatory pathway acts as a rheostat of cysteine enabling *Mtb* enabling adaptation to a sudden heightened requirement for antioxidant molecules during oxidative burst (Fig 8).

Materials and Methods

Bacterial strains and culturing

Bacterial strains used in the study are listed in Appendix Table S2. Mycobacterial strains were cultured in Middlebrook 7H9 medium (BD Biosciences) supplemented with 10% albumin, dextrose, NaCl, catalase (ADC) along with 0.2% glycerol (Sigma) and 0.05% Tween-80 (Sigma), or 7H11 agar (BD Biosciences) with 10% OADC (oleic-acid added to ADC) and 0.2% glycerol. Susceptibility to different *in vitro* stresses was ascertained as previously described (Khan *et al*, 2017). For oxidative stress, the mycobacterium culture was grown in 7H9-ADS (ADC without catalase) to A_{600} ~ 0.2–0.3 followed by exposure to cumene hydroperoxide (CHP; 50 μM) for 24 h, and then plated on 7H11-OADS (OADC without catalase).

Creation of mutants by gene replacement

All knockouts were generated using recombineering (van Kessel & Hatfull, 2007). Approximately 800 bp regions upstream (LHS) and downstream (RHS) of the gene of interest (including ~150 bp of the gene at both ends) were amplified from *Rv* genomic DNA using specific primers (Appendix Table S3). The amplicons were appropriately digested and ligated with two fragments of compatible ends: the fragment containing the *oriE*+cosλ sequences from plasmid pYUB1474 (Jain *et al*, 2014), and the hygromycin resistance (*hyg*^r) cassette from pENTR-Hyg to generate the allelic exchange substrate (AES). The AES was digested with SnaBI to excise out the donor LHS-*hyg*^r-RHS fragment, which was electroporated into the recombineering proficient *Rv*-ET strain expressing RecET from plasmid pNit-ET (Wei *et al*, 2011). Ten to twenty *hyg*^r colonies were analyzed by PCRs across the deletion junctions to screen for legitimate recombination events at the native loci. Mutants were confirmed by Western blotting with the appropriate antibody and then cured of pNit-ET (and thereby kanamycin resistance) through negative selection by plating them on 7H11 agar plates containing 2% sucrose and hygromycin.

Generation of plasmid constructs and strains

Sequences of oligonucleotides used to generate various plasmid constructs and details of the plasmid constructs used in this study are listed in Appendix Tables S2 and S3, respectively. For complementation experiments, the full-length *aosR* gene (*Rv1332*) and the 500 bp region immediately upstream of the *Rv1331* coding region were amplified from *Rv* genomic DNA using specific primers and Phusion DNA polymerase (Thermo Scientific). The amplicons were digested with ScaI-SapI and SapI-HindIII, respectively, and cloned into the ScaI-HindIII sites in pST-Ki (Parikh *et al*, 2013), to generate pST-AosR. The *aosR* mutant CxxxC→AxxxA was constructed with the help of overlap PCR using suitable primers. The amplicon was cloned in pST-Ki under its native promoter (the 500 bp fragment upstream of *Rv1331*) to generate pST-AosR_AxxxA. The *aosR–ΔN* mutant was generated by amplification using a forward primer starting at nucleotide 67 of the *aosR* gene in combination with the gene-specific reverse primer. The coding region of *Msmeg_4909* was amplified from *mc²155* using gene-specific primers. The *mec-cysO-cysM* cluster was amplified from *Rv* genomic DNA using *mec* forward primer in combination with *cysM* reverse primer. The coding region of *cysM* was similarly amplified using gene-specific primers. Amplicons of *aosR-ΔN*, *msmeg_4909* (*aosR_Msm*), *mec-cysO-cysM* (*mom*), *and cysM* were digested with NdeI-HindIII and cloned into the corresponding sites in pNit-3F. pST-aosR, pST-aosR_AxxxA, pNit-AosR-ΔN, pNit-AosR_Msm, pNit-mom, and pNit-CysM constructs were electroporated into *RvΔaosR* to generate *RvΔaosR::aosR, RvΔaosR::aosR_AxxxA, RvΔaosR::aosR-ΔN, RvΔaosR::aosR_Msm, RvΔ aosR::mom,* and *RvΔaosR::cysM* strains, respectively. pNit-CysM was also electroporated into *RvΔcysM* to generate the *RvΔcysM::cysM* strain.

Growth kinetics and *in vitro* stress susceptibility

To evaluate the impact of gene deletions on *in vitro* growth of *Mtb*, wild type (*Rv*), knockout (*RvΔaosR*), and complemented (*RvΔaosR:: aosR*) strains were inoculated into 7H9-ADC at A_{600} ~ 0.05 or into Sauton's medium at A_{600} ~ 0.1. Aliquots were withdrawn to measure A_{600} at the indicated time points, and the bacteria serially diluted before plating to enumerate colony-forming units (CFUs).

To evaluate the susceptibility of *Mtb* strains to oxidative stress, mycobacterial strains were grown to mid-log-phase (A_{600} ~ 0.6–0.8)

in 7H9-ADS. The cells were collected by centrifugation, washed twice with PBS containing 0.05% Tween 80 (PBST), and inoculated into 7H9-ADS medium at A_{600} ~ 0.05. CHP (Sigma; 50 μM) was added when A_{600} reached ~ 0.2–0.3, and CFUs were enumerated on 7H11-OADS agar 24 h later.

For assessing the impact of acidic stress, early–mid-log-phase cultures were washed with PBST and single-cell suspension was inoculated into acidified 7H9-ADC, pH 4.5 (supplemented with 0.02% tyloxapol instead of Tween 80) at A_{600} of 0.05. Serial dilutions of cultures were plated on 7H11-OADC agar after 7 days of incubation. Log-phase cultures were inoculated at A_{600} of 0.3, and the viability of strains was enumerated in the presence of 0.1% sodium dodecyl sulfate for 3 h (SDS, Sigma), PBS for 7 days, or 1 mM DETA/NO for 2 days.

Macrophage infection experiments

Balb/c, C57BL/6 (B6), and mice with targeted deletions of gp91phox (B6.129S6-Cybbtm1Din/J; JAX# 002365) or IFN-γ (B6.129S7-Ifngtm1Ts/J; JAX#002287) were obtained from The Jackson Laboratory. NADPH phagocyte oxidase (gp91) breeder pair-homozygous null mice (gp91$^{-/-}$; Jackson Lab) and heterozygous female (gp91$^{+/-}$; Jackson Lab) were procured from Dr. Apurva Sarin's laboratory with due permission from The Jackson Laboratory. Only the homozygous null litters confirmed by PCRs (using primer sets mentioned in Appendix Table S3) were used for the experiment. 4- to 6-week-old mice of either sex were injected with 4% thioglycolate (Hi-Media) into the peritoneum cavity of the mice. 4 days post-injection, peritoneal macrophages were extracted and maintained at 37°C with 5% CO_2 in RPMI 1640 medium (Invitrogen) supplemented with 10% heat-inactivated fetal bovine serum (FBS, Gibco). The cells were either left untreated or activated overnight with 10 ng/ml IFNγ (BD Biosciences), followed by incubation with 10 ng/ml lipopolysaccharide (LPS, Sigma) for 2 h. For the inhibition of iNOS, cells were treated overnight with 100 μM 1,400 W (Sigma). For experiments with cysteine supplement in the medium, host cells were pretreated with 0.2 mM cysteine prior to mycobacterial infection. Macrophage cells were infected with single-cell suspensions of mycobacterial strains at 1:10 (cells:bacteria) multiplicity of infection (MOI). Cells were washed thrice with warm RPMI to remove non-phagocytosed Mtb 4h post-infection (p.i), and replenished with complete RPMI containing IFNγ, 1,400 W, or cysteine, as desired. For analysis at the specified time points after infection, the infected cells were thoroughly washed with sterile PBS, lysed with 0.05% SDS, and CFUs enumerated on 7H11-OADC plates after serial dilutions.

Screening of phox mutant mice

The final concentration of components in PCR was; Buffer 1×, Primers (oMIR0517, oMIR0518, oMIR0519) 1 μM each, 200 μM dNTP Mix, 0.5 U/reaction Taq polymerase (NEB), with 50–100 ng genomic DNA isolated from the mice tail. The PCR was set in a thermocycler (Bio-Rad) with the following parameters: 98°C for 3 min, [12 cycles of 94°C for 20 s, 64°C for 30 s (−0.5 deg per s cycle) and 72°C for 35 s], followed by [25 cycles of 94°C for 20 s, 58°C for 30 s and 72°C for 35 s], then 72°C for 2 min, 4°C hold. For positive control, genomic DNA isolated from C57BL/6 served as the template. The expected size of amplicon from the null mutant and wild type

was 195 and 240 bp, respectively. The presence of both the bands suggested that the mouse is heterozygous for the gp91 gene.

Infection experiment in mice

Mice (four to six weeks old of either sex) were housed in individually ventilated cages at Tuberculosis Aerosol Challenge Facility, International Centre for Genetic Engineering and Biotechnology (New Delhi, India). Mice (n = 6 at a minimum, per time point) were infected by aerosol route using the Madison Aerosol Chamber (University of Wisconsin, Madison, WI) which is pre-calibrated to deliver ~ 100 bacilli/mice. Two mice for each Mtb strain were euthanized at 24 h post-infection to assess the bacterial deposition. At selected time points, lung and spleen were removed aseptically and CFUs in the homogenates were enumerated on 7H11 agar-PANTA plates.

Purification of recombinant proteins, generation of antibodies, and gel-filtration chromatography

aosR, cysK1, cysK2, cysM, clpS, cysO, and rv1333 genes were PCR amplified using specific primers (Appendix Table S3) and cloned into NdeI-HindIII sites in pQE2 vector. The expression constructs were transformed into E. coli DH5α, and expression was induced at A_{600} ~ 0.6, with 0.1 mM IPTG (isopropyl-D-thiogalactopyranoside) at 22°C for 14 h for His-AosR and 18°C for 16 h for other proteins. The cells were washed with PBS, and resuspended in lysis buffer [20 mM sodium phosphate, (pH 7.4), 50 mM NaCl, 5 mM imidazole, 10 mM β-mercaptoethanol, 1 mM DTT], and lysed. Following clarification, the supernatant was nutated with equilibrated Ni^{2+}-NTA Beads (Sigma) 4°C for 12 h and washed with 10-bed volumes of lysis buffer containing 200 mM NaCl and 10 mM imidazole. The proteins were eluted in elution buffer [20 mM sodium phosphate, (pH 7.4), 50 mM NaCl, 10 mM β-mercaptoethanol] containing different concentrations of imidazole. Peak fractions were dialyzed against dialysis buffer (10 mM Tris–HCl pH 7.5, 20 mM NaCl, and 20% glycerol) and stored at −70°C. 400 μg of purified His-tagged protein in PBS was mixed with Freund's incomplete adjuvant (Sigma) in 1:1 ratio to a final volume of 1.2 ml. 200 μl of the emulsion was injected subcutaneously at two sites into six mice. In the case of ClpS, Rv1333, CysK2, Coomassie-stained bands were excised from the gel, and the emulsion was prepared. Three booster doses were given every two weeks. Final bleed was collected 7 days following final injection, and Western blotting was performed to assess antibody specificity and sensitivity of the antibody.

For Western blotting, 20–60 μg of Mtb whole-cell lysate was resolved on SDS–PAGE, transferred onto nitrocellulose membrane, and probed with α-AosR, α-CysK1, α-CysK2, α-CysM, α-ClpS, α-CysO, and α-Rv1333 antibodies raised in mice at 1:1,000 dilution or α-SigA and α-GroEL-1 antibodies (used as controls) raised in the rabbit at 1:10,000 dilution. Monoclonal α-FLAG M2 (Sigma-F1804) antibody was used at 1:2,500 dilution. The target proteins were detected with the help of a chemiluminescent HRP substrate reagent (Millipore, USA), captured on ImageQuant LAS 500 (GE), and quantified using ImageJ.

Gel filtration chromatography (GFC) was performed in buffer; 30 mM Tris-pH 7.5, 150 mM NaCl, 5% glycerol, and 25 mM arginine containing either 2 mM oxidized or reduced DTT. The protein was concentrated using a centricon filter with a 10 kDa

cut-off and loaded onto a HiLoad 16/60 Superdex 75 column (GE healthcare).

Monobromobimane assay

Monobromobimane reagent (mBBr; Sigma) forms a conjugate with free thiol groups, and this conjugate exhibits fluorescence with absorption/emission maxima of 394/490 nm. The AosR protein (1 μM) was incubated in buffers containing different molar ratios of oxidized and reduced DTT (4:0, 3:1, 2:2, 1:3, and 0:4), followed by the addition of 10 μM mBBr (dissolved in 100% acetonitrile). The mixes were incubated in the dark at 25°C for 1 h, followed by measurement of the fluorescence emission spectra at 25°C from 430 to 600 nm after excitation at 390 nm wavelength, using a Cary Eclipse fluorescence spectrophotometer (Agilent Technologies, Santa Clara, USA). Protein-free solution was taken as blank. Each reading represents an average of three independent readings.

RNA isolation and qRT–PCRs

RNA was isolated from exponentially growing cultures equivalent to 10 $O.D._{600}$ units. The collected cells were resuspended in TRIzol reagent (Invitrogen), lysed using a bead beater (MP FastPrep system, MP Biomedicals) as per manufacturer's instructions, and the TRIzol-lysed cell mix was extracted with chloroform, followed by precipitation of RNA using isopropanol. The RNA pellet was dissolved in RNase-free water (30 μl with 2 μl of RiboLock (Thermo Scientific)). DNA contamination was removed by DNase I (Invitrogen) treatment, and the RNA was further purified using RNeasy mini columns (Qiagen). RNA (500 ng) was reverse transcribed using iScript cDNA Synthesis Kit (Bio-Rad), and qRT–PCRs were performed using iTaq Universal SYBR GreenSupermix (Bio-Rad) in a MasterCycler Real Plex real-time PCR system (Eppendorf, Germany). Normalization of the data was performed with respect to 16s rRNA (*rrs* gene) expression levels (Appendix Table S4). The $2^{(-\Delta\Delta Ct)}$ method was used to analyze the relative changes in gene expression.

RNA sequencing and analysis

The RNA sequencing workflow is outlined in Appendix Fig S1. Total RNA isolated from three biological replicates of *Rv* and *RvΔaosR* cultures grown in the presence or absence of CHP (50 μM) was analyzed using Agilent 2100 BioAnalyzer (Agilent RNA 6000 Nano Kit). Samples with RIN values higher than 7.5 were submitted for RNAseq analysis to Bencos Research Solutions Pvt Ltd (Bangalore, India). Transcriptome sequencing was performed using the Illumina NovaSeq 6000 Platform with read length 100 bp, generating 20 million paired-end reads per sample. Raw reads were uploaded on www.galaxy.org, and the quality of raw sequencing reads was assessed with the help of FastQC software, ensuring the quality score to be above 30. The reference genome sequence for *Rv* was downloaded from the Ensembl, and a custom annotation file was prepared. The paired ends were combined with the help of the BAM tool and were aligned with the reference genome using Bowtie2. HTSeq-count was used to calculate the read counts per gene. Genes with less than 300 total reads were discarded, and the rest were analyzed using a custom python script to identify differentially expressed genes (DEGs) using DESeq2 (1 $\log_2$ fold change, $P_{adj} < 0.1$).

Figures were generated using custom scripts in python3. For identification of the AosR regulon during oxidative stress, DEGs exclusively found in the *Rv*+CHP/*RvΔaosR*+CHP but not in *RvΔaosR*/*RvΔaosR*+CHP were plotted in the form of a heat map using heatmapper.ca.

Identification of operon by intergenic PCR

To identify *the aosR* operon, cDNA was prepared from log-phase culture of *Rv*. The PCR was set up with 2 μl cDNA, 2 μl 5X GC buffer, 0.25 μl dNTP Mix (final concentration 12.5 mM), 1 μl of 10 μM Primer Mix, 0.3 μl 100% DMSO, and 0.2 U Phusion DNA Polymerase (Thermo Scientific). The PCR was set in a thermocycler (ProFlex PCR System, Applied Biosystems) with the following parameters: denaturation at 98°C for 3 min, 35 cycles of "98°C for 10 s, 65°C for 30 s and 72°C for 20 s" and one extension cycle for 3 min at 72°C. Genomic DNA from *Rv* served as the template for positive control and reaction performed in the absence of reverse transcriptase served as the negative control.

Luciferase reporter assay

The 500 bp or 100 bp sequence immediately upstream of the *mec* or *sigA* start codon was cloned in ScaI-NdeI sites of a Tweety integrative shuttle vector. The coding region of the luciferase gene was cloned in the NdeI-HindIII sites, with either no promoter upstream of it, or linked to the *sigA* or *mec* promoter. The constructs were electroporated into *Rv* and *RvΔaosR*. The resulting strains were grown in 7H9-ADS to early-log-phase ($OD_{600} \sim 0.3$) and subjected to oxidative stress with 50 μM CHP for 6 h. Lysates prepared from cultures in the absence of oxidative stress (untreated) were used as controls. Equal concentrations of lysates were used for measuring the luciferase activity using RenillaGlo Luciferase Assay Kit (Promega).

Electrophoretic mobility shift assay (EMSA)

100 nt long complementary oligonucleotides corresponding to the template and non-template strands sequence upstream *mec were commercially synthesized (Sigma). The template strand was end-labeled with 20* μCi [γ-^{32}P]ATP using T4 polynucleotide kinase (PNK) in a 20 μl reaction at 37°C for 30 min as per the manufacturer's instructions. PNK was heat-inactivated, and reaction volume was made up to 50 μl and purified using sephadex G-50 mini-columns (Bio-Rad). 5'-end-labeled template oligo was mixed with twofold molar excess of complementary unlabeled non-template oligo in 1 × binding buffer (50 mM Tris–HCl pH-7.5, 1 mM EDTA, 2 mM $MnCl$), heated at 90°C for 5 min, centrifuged for 30 s, and left at RT for 2 h followed by overnight at 4°C to form double-stranded EMSA substrate. An aliquot of the reaction was resolved on 12% PAGE gel in 0.5 × TBE buffer to confirm the formation of double-stranded DNA. EMSA reactions were performed with 5–7.5 × 10^4 cpm oligonucleotide/sample in the presence of 10 mM DTT (reduced conditions) or diamide (oxidized conditions) in a 20 μl 1× binding buffer containing 4 μM BSA or 2 μM His-AosR + 2 μM BSA, or 2 μM His-SigH + 2 μM BSA or 2 μM His-AosR + 2 μM His-SigH for 15 min at RT followed by 30 min at 4°C. The protein–DNA complexes were resolved on 8% Native PAGE; gels were dried and imaged using a phosphorimager (GE).

Biolayer interferometry (BLI)

The binding kinetics of AosR and AosR$_{AxxxA}$ with SigH were evaluated by BLI using Octet Red96® instrument using Amine Reactive 2nd Generation (AR2G) Biosensors (ForteBio, Inc.). Sensors were pre-incubated with MQ water for 10–15 min, followed by activation with a mixture of EDC and NHS for 420 s. Sensors were incubated with 200 ml of 250 nM SigH for 600 s to the levels of 1.5–2.0 nm in 10 mM sodium acetate pH 6.0. Subsequently, the activated carboxylate groups on the surface were blocked with 1.0 M ethanolamine pH 8.5 and the uncoupled His-SigH washed from the biosensor. The SigH captured sensors were equilibrated in running buffer (10 mM HEPES pH 7.4, 150 mM NaCl, and 3 mM EDTA pH 8.0) for 120 s, and sensors were then dipped in various concentrations (125–1,000 nM) AosR or AxxxA protein wells in the running buffer in the presence of 4 mM oxidized or reduced DTT for the binding assay experiment. The association kinetics was monitored for 600 s followed by moving sensors to buffers only to measure dissociation for the next 600 s. The surface was regenerated with a buffer consisting of 50 mM NaOH for 5 s. All the data were recorded at 25°C with an agitation speed of 1,000 rpm. The equilibrium dissociation constant (Kd) was obtained by fitting the binding data in a nonlinear regression analysis to a global 1:1 ligand interaction model. Data were processed using Octet Analysis software 10.0 provided by the manufacturer.

In vitro measurement of mycothiol redox potential (E$_{MSH}$)

pMV762-Mrx1roGFP2 (Bhaskar *et al*, 2014) plasmid was modified to insert chloramphenicol resistance casette in HpaI site. The resulting plasmid was electroporated in *Rv, RvΔaosR*, and *RvΔaosR::aosR*, and the intracellular redox state was measured as described previously (Khan *et al*, 2017). Briefly, bacilli expressing Mrx1-roGFP2 bioprobe were treated with 5 mM H$_2$O$_2$ for various time points. 10 mM nethylmaleimide (Sigma) was added for 5 min to block the redox state of roGFP2 (Bhaskar *et al*, 2014). Cells were fixed with 4% PFA and analyzed by flow cytometry using FITC (495 nm excitation, 519 nm emission) and V500 (415 nm excitation, 500 nm emission) channels. The 405/488 ratios were normalized by treating cells with 2 mM CHP (100% oxidation; 405/488 ratio set to 1) and 50 mM DTT (100% reduction; 405/488 ratio set to 0.1).

Thiol estimation

Protein thiol was estimated using a commercially available kit (Invitrogen—Cat no. EIARSHF) as per the manufacturer's instructions. The kit contains a non-fluorescent molecule that covalently binds free thiol in the sample to produce a fluorescent product. *Rv, RvΔaosR*, and *RvΔaosR::aosR* were either left untreated or subjected to CHP stress for 6 h. WCLs were prepared in the presence of DTT to reduce oxidized thiols. The concentration of thiols in μM/μg WCL was estimated with respect to the standard curve obtained using different concentrations of N-acetylcysteine.

Mass spectrometry-based multiple reaction monitoring analysis to quantitate metabolites

Rv, RvΔaosR, and *RvΔaosR::aosR* strains at A$_{600}$ ~ 0.2 were either treated or left untreated with 50 μM CHP for 24 h. Bacterial cultures

corresponding to A$_{600}$ ~ 10 / sample were washed thrice with Tris–HCl, pH 7.4 and were quenched in liquid nitrogen. Cell pellets were resuspended in pre-chilled methanol and lysed with help of a bead beater, and the lysates were clarified. The remaining metabolites were extracted from the pellet with 100% methanol and subsequent to clarification; the pellet was subjected to a third-round extraction with 50% methanol. Clarified lysates from all three extractions were pooled and dried using a speed vac (Savant, SPD 1010, Thermo Electron Corporation). Metabolite extracts from *Mtb* were reconstituted in 90 μl of sample reconstitution buffer (6:4-acetonitrile:LC-MS Grade water). The mass spectrometry-based multiple reaction monitoring (MRM) analysis was performed in a positive ionization mode on a 4000 QTRAP triple quadrupole mass spectrometer (AB SCIEX, Foster City, CA) equipped with Shimadzu Prominence binary pump HPLC system (Shimadzu Corporation, Japan). Prior to sample injection into the liquid chromatography (LC) system, 10 μl of internal standard d$_2$ L-phenylalanine (25 ng/μl) was added to the metabolite extracts. The LC-MRM MS/MS-targeted metabolomic profiling was undertaken for mycothiol (MSH), ergothioneine (ERG), nicotinamide adenine dinucleotide (NAD$^+$) and the reduced form of NAD$^+$ (NADH). The pure analytical standards for each metabolite were procured from Sigma-Aldrich except for MSH. Acquisition protocol for MSH was kindly provided by Dr. Sunil Laxman, Institute for Stem Cell Biology and Regenerative Medicine (inStem), Bangalore, India. 10 μl of the metabolite extract was injected through the HPLC autosampler on a 4.6 mm × 150 mm XBridge 5 μm HILIC column (Waters, Milford, MA). The mobile phases used for HILIC chromatography were 10 mM ammonium formate in LC-MS grade water with 0.1% formic acid (mobile phase A) and 0.1% formic acid in acetonitrile (mobile phase B). The sample was eluted at 0.7 ml/min flow rate with a 35 min total chromatography run time. The gradient started from 95% mobile phase B, reaching up to 20% mobile phase B over a period of 25 min. The column was kept at 20% mobile phase B for 2 min then returned to 5% mobile phase A for an 8-min equilibration step. The four parameters were optimized for the MRM acquisition of the four metabolites using analytical standards. Declustering potential (DP), entrance potential (EP), collision energy (CE), and collision cell exit potential (CXP) were the parameters that were optimized. For MSH, DP of 65, EP of 12, CE of 21, and CXP of 12 were optimized to analyze the MRM transitions of *m/z* 487.5 (Q1)/134.1 (Q3). In the case of ERG, DP of 47, EP of 9, CE of 26, and CXP of 22 were optimized for the MRM transitions of m/z 230.0 (Q1)/127.2 (Q3). NAD$^+$, the optimized value for DP was 45, EP was 10, CE was 60, and CXP was 8 for acquiring the MRM transitions of *m/z* 664.1 (Q1)/136.06 (Q3). For NADH, the DP value was optimized at 96, EP at 10, CE at 25, and CXP at 28 to acquire the MRM transitions of *m/z* 666.0 (Q1)/649.13 (Q3). The 4000 QTRAP system was operated at the following values: curtain gas at 30, ion spray voltage at 5500, the temperature at 550, ion source gas at 40. Data acquisition and analysis were performed on the Analyst 1.5 software platform (Sciex, Foster City, CA). The samples were acquired in a randomized order at the time of acquisition. To check the instrument performance over time, the internal standard peak areas were utilized. Four technical replicates of each sample were analyzed using the LC-MRM MS/MS analysis. Further, the peak areas obtained after integration were exported to Microsoft excel file format in a matrix form.

Interactome

Three biological replicates of *RvΔaosR* and *RvΔaosR::pN-aosR* early-log cultures grown in 7H9-ADS medium containing inducer isovaleronitrile (IVN; 5 μM; Sigma) were subjected to CHP (50 μM) treatment for 24 h. Two biological replicates of untreated induced *RvΔaosR::pN-aosR* were used as an additional control. The cultures were fixed using 1% formaldehyde for 15 min, followed by the addition of 250 mM glycine to neutralize the cross-linking. Samples were lysed in a buffer containing protease inhibitors. Lysates were analyzed for the expression of AosR using anti-FLAG antibody, and FLAG-tagged AosR was immunoprecipitated from 2 mg of lysate using FLAG-M2 agarose beads (Sigma). The samples were loaded on 12% SDS–PAGE and resolved till the dye front was ~ 2 cm into the resolving gel. The bands were excised, dehydrated, reduced, alkylated, and digested with trypsin overnight. Proteomics analyses were performed using quantitative LC-MS/MS, as described previously (Jain *et al*, 2018).

Statistical analysis

Unless mentioned otherwise, experiments described in the manuscript were executed independently at least twice, being performed minimally in triplicates each time. The significance of the results was analyzed using one-way ANOVA followed by a *post hoc* test (Tukey test) unless otherwise specified. GraphPad Prism 5 was used to plot the acquired data sets and calculate statistical significance and modified using Adobe Illustrator. *P* values < 0.05 were considered as statistically significant. Source data of this study are available from the corresponding author upon request.

Data availability

RNAseq data are available at the NCBI Gene Expression Omnibus Database, accession number GSE161190 (https://www.ncbi.nlm.nih.gov/geo/query/acc.cgi?acc=GSE161190).

Expanded View for this article is available online.

Conflict of interest

The authors declare that they have no conflict of interest.

Animal experimentation

The animal experimental protocol was approved by the Animal Ethics Committee of the National Institute of Immunology, New Delhi, India (IAEC#409/16 & IAEC#462/18), as per the guidelines issued by the Committee for the Purpose of Control and Supervision of Experiments on Animals (CPCSEA), Government of India.

References

Agren D, Schnell R, Oehlmann W, Singh M, Schneider G (2008) Cysteine synthase (CysM) of *Mycobacterium tuberculosis* is an O-phosphoserine sulfhydrylase: evidence for an alternative cysteine biosynthesis pathway in mycobacteria. *J Biol Chem* 283: 31567–31574

Bellerose MM, Proulx MK, Smith CM, Baker RE, Ioerger TR, Sassetti CM (2020) Distinct bacterial pathways influence the efficacy of antibiotics against *Mycobacterium tuberculosis*. *mSystems* 5: e00396-20

Bhaskar A, Chawla M, Mehta M, Parikh P, Chandra P, Bhave D, Kumar D, Carroll KS, Singh A (2014) Reengineering redox sensitive GFP to measure mycothiol redox potential of *Mycobacterium tuberculosis* during infection. *PLoS Pathog* 10: e1003902

Brunner K, Maric S, Reshma RS, Almqvist H, Seashore-Ludlow B, Gustavsson AL, Poyraz O, Yogeeswari P, Lundback T, Vallin M *et al* (2016) Inhibitors of the cysteine synthase CysM with antibacterial potency against dormant *Mycobacterium tuberculosis*. *J Med Chem* 59: 6848–6859

Burian J, Ramon-Garcia S, Howes CG, Thompson CJ (2012) WhiB7, a transcriptional activator that coordinates physiology with intrinsic drug resistance in *Mycobacterium tuberculosis*. *Expert Rev Anti Infect Ther* 10: 1037–1047

Burns KE, Baumgart S, Dorrestein PC, Zhai H, McLafferty FW, Begley TP (2005) Reconstitution of a new cysteine biosynthetic pathway in *Mycobacterium tuberculosis*. *J Am Chem Soc* 127: 11602–11603

Burns-Huang K, Mundhra S (2019) *Mycobacterium tuberculosis* cysteine biosynthesis genes mec+-cysO-cysM confer resistance to clofazimine. *Tuberculosis* 115: 63–66

Chawla M, Parikh P, Saxena A, Munshi M, Mehta M, Mai D, Srivastava AK, Narasimhulu KV, Redding KE, Vashi N *et al* (2012) *Mycobacterium tuberculosis* WhiB4 regulates oxidative stress response to modulate survival and dissemination in vivo. *Mol Microbiol* 85: 1148–1165

Das B, Kashino SS, Pulu I, Kalita D, Swami V, Yeger H, Felsher DW, Campos-Neto A (2013) CD271(+) bone marrow mesenchymal stem cells may provide a niche for dormant *Mycobacterium tuberculosis*. *Sci Transl Med* 5: 170ra113

Dassler T, Maier T, Winterhalter C, Bock A (2000) Identification of a major facilitator protein from *Escherichia coli* involved in efflux of metabolites of the cysteine pathway. *Mol Microbiol* 36: 1101–1112

DeJesus MA, Gerrick ER, Xu W, Park SW, Long JE, Boutte CC, Rubin EJ, Schnappinger D, Ehrt S, Fortune SM *et al* (2017) Comprehensive

essentiality analysis of the *Mycobacterium tuberculosis* genome via saturating transposon mutagenesis. *MBio* 8: e02133-16

Deretic V, Philipp W, Dhandayuthapani S, Mudd MH, Curcic R, Garbe T, Heym B, Via LE, Cole ST (1995) *Mycobacterium tuberculosis* is a natural mutant with an inactivated oxidative-stress regulatory gene: implications for sensitivity to isoniazid. *Mol Microbiol* 17: 889−900

Edwards KM, Cynamon MH, Voladri RK, Hager CC, DeStefano MS, Tham KT, Lakey DL, Bochan MR, Kernodle DS (2001) Iron-cofactored superoxide dismutase inhibits host responses to *Mycobacterium tuberculosis*. *Am J Respir Crit Care Med* 164: 2213−2219

Ehrt S, Schnappinger D, Bekiranov S, Drenkow J, Shi S, Gingeras TR, Gaasterland T, Schoolnik G, Nathan C (2001) Reprogramming of the macrophage transcriptome in response to interferon-gamma and *Mycobacterium tuberculosis*: signaling roles of nitric oxide synthase-2 and phagocyte oxidase. *J Exp Med* 194: 1123−1140

Eum SY, Kong JH, Hong MS, Lee YJ, Kim JH, Hwang SH, Cho SN, Via LE, Barry 3rd CE (2010) Neutrophils are the predominant infected phagocytic cells in the airways of patients with active pulmonary TB. *Chest* 137: 122−128

Even S, Burguiere P, Auger S, Soutourina O, Danchin A, Martin-Verstraete I (2006) Global control of cysteine metabolism by CymR in *Bacillus subtilis*. *J Bacteriol* 188: 2184−2197

Fontan P, Aris V, Ghanny S, Soteropoulos P, Smith I (2008) Global transcriptional profile of *Mycobacterium tuberculosis* during THP-1 human macrophage infection. *Infect Immun* 76: 717−725

Franke I, Resch A, Dassler T, Maier T, Bock A (2003) YfiK from *Escherichia coli* promotes export of O-acetylserine and cysteine. *J Bacteriol* 185: 1161−1166

Hatzios SK, Bertozzi CR (2011) The regulation of sulfur metabolism in *Mycobacterium tuberculosis*. *PLoS Pathog* 7: e1002036

Hillion M, Antelmann H (2015) Thiol-based redox switches in prokaryotes. *Biol Chem* 396: 415−444

Huerta-Cepas J, Szklarczyk D, Forslund K, Cook H, Heller D, Walter MC, Rattei T, Mende DR, Sunagawa S, Kuhn M *et al* (2016) eggNOG 4.5: a hierarchical orthology framework with improved functional annotations for eukaryotic, prokaryotic and viral sequences. *Nucleic Acids Res* 44: D286−293

Huerta-Cepas J, Szklarczyk D, Heller D, Hernandez-Plaza A, Forslund SK, Cook H, Mende DR, Letunic I, Rattei T, Jensen LJ *et al* (2019) eggNOG 5.0: a hierarchical, functionally and phylogenetically annotated orthology resource based on 5090 organisms and 2502 viruses. *Nucleic Acids Res* 47: D309−D314

Jain P, Hsu T, Arai M, Biermann K, Thaler DS, Nguyen A, González PA, Tufariello JM, Kriakov J, Chen B *et al* (2014) Specialized transduction designed for precise high-throughput unmarked deletions in *Mycobacterium tuberculosis*. *MBio* 5: e01245-01214

Jain P, Malakar B, Khan MZ, Lochab S, Singh A, Nandicoori VK (2018) Delineating FtsQ mediated regulation of cell division in *Mycobacterium tuberculosis*. *J Biol Chem* 293: 12331−12349

van Kessel JC, Hatfull GF (2007) Recombineering in *Mycobacterium tuberculosis*. *Nat Methods* 4: 147−152

Khan MZ, Bhaskar A, Upadhyay S, Kumari P, Rajmani RS, Jain P, Singh A, Kumar D, Bhavesh NS, Nandicoori VK (2017) Protein kinase G confers survival advantage to *Mycobacterium tuberculosis* during latency-like conditions. *J Biol Chem* 292: 16093−16108

Kredich NM (1992) The molecular basis for positive regulation of cys promoters in *Salmonella typhimurium* and *Escherichia coli*. *Mol Microbiol* 6: 2747−2753

Kumar A, Toledo JC, Patel RP, Lancaster Jr JR, Steyn AJ (2007) *Mycobacterium tuberculosis* DosS is a redox sensor and DosT is a hypoxia sensor. *Proc Natl Acad Sci USA* 104: 11568−11573

Laxman S, Sutter BM, Wu X, Kumar S, Guo X, Trudgian DC, Mirzaei H, Tu BP (2013) Sulfur amino acids regulate translational capacity and metabolic homeostasis through modulation of tRNA thiolation. *Cell* 154: 416−429

Manganelli R, Provvedi R, Rodrigue S, Beaucher J, Gaudreau L, Smith I (2004) Sigma factors and global gene regulation in *Mycobacterium tuberculosis*. *J Bacteriol* 186: 895−902

Manganelli R, Voskuil MI, Schoolnik GK, Smith I (2001) The *Mycobacterium tuberculosis* ECF sigma factor sigmaE: role in global gene expression and survival in macrophages. *Mol Microbiol* 41: 423−437

Manganelli R, Voskuil MI, Schoolnik GK, Dubnau E, Gomez M, Smith I (2002) Role of the extracytoplasmic-function sigma factor sigma(H) in *Mycobacterium tuberculosis* global gene expression. *Mol Microbiol* 45: 365−374

Mishra R, Kohli S, Malhotra N, Bandyopadhyay P, Mehta M, Munshi M, Adiga V, Ahuja VK, Shandil RK, Rajmani RS *et al* (2019) Targeting redox heterogeneity to counteract drug tolerance in replicating *Mycobacterium tuberculosis*. *Sci Transl Med* 11: eaaw6635

Nambi S, Long JE, Mishra BB, Baker R, Murphy KC, Olive AJ, Nguyen HP, Shaffer SA, Sassetti CM (2015) The oxidative stress network of *Mycobacterium tuberculosis* reveals coordination between radical detoxification systems. *Cell Host Microbe* 17: 829−837

Nathan CF, Murray HW, Wiebe ME, Rubin BY (1983) Identification of interferon-gamma as the lymphokine that activates human macrophage oxidative metabolism and antimicrobial activity. *J Exp Med* 158: 670−689

Ng VH, Cox JS, Sousa AO, MacMicking JD, McKinney JD (2004) Role of KatG catalase-peroxidase in mycobacterial pathogenesis: countering the phagocyte oxidative burst. *Mol Microbiol* 52: 1291−1302

Parikh A, Kumar D, Chawla Y, Kurthkoti K, Khan S, Varshney U, Nandicoori VK (2013) Development of a new generation of vectors for gene expression, gene replacement, and protein-protein interaction studies in mycobacteria. *Appl Environ Microbiol* 79: 1718−1729

Piddington DL, Fang FC, Laessig T, Cooper AM, Orme IM, Buchmeier NA (2001) Cu, Zn superoxide dismutase of *Mycobacterium tuberculosis* contributes to survival in activated macrophages that are generating an oxidative burst. *Infect Immun* 69: 4980−4987

Raman S, Song T, Puyang X, Bardarov S, Jacobs Jr WR, Husson RN (2001) The alternative sigma factor SigH regulates major components of oxidative and heat stress responses in *Mycobacterium tuberculosis*. *J Bacteriol* 183: 6119−6125

Rawat M, Uppal M, Newton G, Steffek M, Fahey RC, Av-Gay Y (2004) Targeted mutagenesis of the *Mycobacterium smegmatis* mca gene, encoding a mycothiol-dependent detoxification protein. *J Bacteriol* 186: 6050−6058

Rengarajan J, Bloom BR, Rubin EJ (2005) Genome-wide requirements for *Mycobacterium tuberculosis* adaptation and survival in macrophages. *Proc Natl Acad Sci USA* 102: 8327−8332

Rey DA, Puhler A, Kalinowski J (2003) The putative transcriptional repressor McbR, member of the TetR-family, is involved in the regulation of the metabolic network directing the synthesis of sulfur containing amino acids in *Corynebacterium glutamicum*. *J Biotechnol* 103: 51−65

Rohde KH, Veiga DF, Caldwell S, Balazsi G, Russell DG (2012) Linking the transcriptional profiles and the physiological states of *Mycobacterium tuberculosis* during an extended intracellular infection. *PLoS Pathog* 8: e1002769

Saini V, Cumming B, Guidry L, Lamprecht DA, Adamson J, Reddy V, Chinta K, Mazorodze JH, Glasgow J, Richard-Greenblatt M *et al* (2016) Ergothioneine maintains redox and bioenergetic homeostasis essential for drug susceptibility and virulence of *Mycobacterium tuberculosis*. *Cell Rep* 14: 572−585

Sassetti CM, Rubin EJ (2003) Genetic requirements for mycobacterial survival during infection. *Proc Natl Acad Sci USA* 100: 12989–12994

Senaratne RH, De Silva AD, Williams SJ, Mougous JD, Reader JR, Zhang T, Chan S, Sidders B, Lee DH, Chan J *et al* (2006) 5'-Adenosinephosphosulphate reductase (CysH) protects *Mycobacterium tuberculosis* against free radicals during chronic infection phase in mice. *Mol Microbiol* 59: 1744–1753

Sharp JD, Singh AK, Park ST, Lyubetskaya A, Peterson MW, Gomes AL, Potluri LP, Raman S, Galagan JE, Husson RN (2016) Comprehensive definition of the SigH regulon of *Mycobacterium tuberculosis* reveals transcriptional control of diverse stress responses. *PLoS One* 11: e0152145

Shatalin K, Shatalina E, Mironov A, Nudler E (2011) H2S: a universal defense against antibiotics in bacteria. *Science* 334: 986–990

Singh A, Crossman DK, Mai D, Guidry L, Voskuil MI, Renfrow MB, Steyn AJ (2009) *Mycobacterium tuberculosis* WhiB3 maintains redox homeostasis by regulating virulence lipid anabolism to modulate macrophage response. *PLoS Pathog* 5: e1000545

Singh N, Kumar A (2015) Virulence factor SenX3 is the oxygen-controlled replication switch of *Mycobacterium tuberculosis*. *Antioxid Redox Signal* 22: 603–613

Takumi K, Nonaka G (2016) Bacterial cysteine-inducible cysteine resistance systems. *J Bacteriol* 198: 1384–1392

Tornack J, Reece ST, Bauer WM, Vogelzang A, Bandermann S, Zedler U, Stingl G, Kaufmann SH, Melchers F (2017) Human and mouse hematopoietic stem cells are a depot for dormant *Mycobacterium tuberculosis*. *PLoS One* 12: e0169119

Voskuil MI, Bartek IL, Visconti K, Schoolnik GK (2011) The response of *Mycobacterium tuberculosis* to reactive oxygen and nitrogen species. *Front Microbiol* 2: 105

Wei JR, Krishnamoorthy V, Murphy K, Kim JH, Schnappinger D, Alber T, Sassetti CM, Rhee KY, Rubin EJ (2011) Depletion of antibiotic targets has widely varying effects on growth. *Proc Natl Acad Sci USA* 108: 4176–4181

Wheeler PR, Coldham NG, Keating L, Gordon SV, Wooff EE, Parish T, Hewinson RG (2005) Functional demonstration of reverse transsulfuration in the *Mycobacterium tuberculosis* complex reveals that methionine is the preferred sulfur source for pathogenic Mycobacteria. *J Biol Chem* 280: 8069–8078

Wolf AJ, Linas B, Trevejo-Nunez GJ, Kincaid E, Tamura T, Takatsu K, Ernst JD (2007) *Mycobacterium tuberculosis* infects dendritic cells with high frequency and impairs their function in vivo. *J Immunol* 179: 2509–2519

ARTICLE

LipidII interaction with specific residues of *Mycobacterium tuberculosis* PknB extracytoplasmic domain governs its optimal activation

Prabhjot Kaur[1], Marvin Rausch [2,3], Basanti Malakar[1], Uchenna Watson[4], Nikhil P. Damle[1,6], Yogesh Chawla[1,7], Sandhya Srinivasan[5], Kanika Sharma[5], Tanja Schneider[2,3], Gagan Deep Jhingan[5], Deepak Saini[4], Debasisa Mohanty[1], Fabian Grein [2,3] & Vinay Kumar Nandicoori [1]

The *Mycobacterium tuberculosis* kinase PknB is essential for growth and survival of the pathogen in vitro and in vivo. Here we report the results of our efforts to elucidate the mechanism of regulation of PknB activity. The specific residues in the PknB extracytoplasmic domain that are essential for ligand interaction and survival of the bacterium are identified. The extracytoplasmic domain interacts with mDAP-containing LipidII, and this is abolished upon mutation of the ligand-interacting residues. Abrogation of ligand-binding or sequestration of the ligand leads to aberrant localization of PknB. Contrary to the prevailing hypothesis, abrogation of ligand-binding is linked to activation loop hyperphosphorylation, and indiscriminate hyperphosphorylation of PknB substrates as well as other proteins, ultimately causing loss of homeostasis and cell death. We propose that the ligand-kinase interaction directs the appropriate localization of the kinase, coupled to stringently controlled activation of PknB, and consequently the downstream processes thereof.

---

[1] National Institute of Immunology, Aruna Asaf Ali Marg, New Delhi 110067, India. [2] Institute for Pharmaceutical Microbiology, University Hospital Bonn, University of Bonn, Bonn 53105, Germany. [3] German Center for Infection Research (DZIF), Partner Site Bonn-Cologne, Bonn 53105, Germany. [4] Department of Molecular Reproduction, Development and Genetics, Indian Institute of Science, Bengaluru 560012, India. [5] Vproteomics, Valerian Chem Private Limited, Green Park Main, New Delhi 110016, India. [6] Present address: BIOSS, Center for Biological Signaling Studies, University of Freiburg, Freiburg 79104, Germany. [7] Present address: Department of Microbiology and Immunology, Weill Cornell Medical College, New York 10065 NY, USA. These authors contributed equally: Marvin Rausch, Basanti Malakar. Correspondence and requests for materials should be addressed to V.K.N. (email: vinaykn@nii.ac.in)

Protein phosphorylation has come forth as a preeminent circuitry regulating a vast number of physiological processes in the bacterial kingdom. A particular class of receptor-type serine-threonine kinase called PASTA (Penicillin binding proteins And Serine Threonine Associated) kinase is widespread across gram-positive firmicutes and actinomycetes and is known for its functions associated with bacterial cell growth[1]. These protein kinases have an intracellular kinase domain, which shows sequence and structural homology to the eukaryotic serine/threonine kinases, and an extracytoplasmic (Ec) domain made up of varying number of PASTA domains. PASTA kinases are usually required by bacteria under stress conditions like nutrient starvation, antibiotic stress, biofilm formation etc., and are non-essential for their vegetative growth[2]. However, in the pathogenic bacterium *Mycobacterium tuberculosis* (*Mtb*) the PASTA kinase PknB (PknB_{Mtb}) is an essential gene[3–5] and is proposed to be one of the master regulators of serine/threonine phosphorylation-mediated signaling[6].

The essential nature of PknB in mycobacteria stems from its ability to influence the activity of a large repertoire of substrates involved in cell wall synthesis, cell growth, cellular metabolism, transcription, and translation[7]. Over-expression or depletion of PknB impacts cellular morphology and survival of *Mtb*[5,8], which suggests that the expression and activity of this kinase must be critically fine-tuned inside the bacterium. PknB levels are modulated under different conditions of mycobacterial growth: for instance its levels are down regulated during dormancy[9] and nutrient starvation[10] and are up regulated during exponential growth[8] and resuscitation[9]. The dynamicity of PknB_{Mtb} regulation implies that the receptor kinase actively monitors its environment and responds accordingly, in an effort to provide survival advantage. PknB is believed to respond to environmental signals through PASTA domain interactions with the specific ligand, identified to be non-crosslinked peptidoglycan (PG) fragments called muropeptides[11]. In line with this, purified PASTA domains of PknB_{Mtb} interact and bind with a synthetic muropeptide containing isoglutamine (iGln) and meso-diaminopimelic acid (mDAP) residues at the second and third position of the stem peptide in vitro (Fig. 1a)[11,12].

The prevailing hypothesis suggests that the interaction of the extracytoplasmic domain with the ligand results in the dimerization of intracellular kinase domain, which is required for the activation of the kinase through activation loop phosphorylations (Fig. 1b)[13]. The hypothesis is based on the front-to-front and back-to-back dimeric crystal structures of cytosolic kinase domain[14,15] and surface plasmon resonance-based in vitro binding experiments of PASTA domain with the muropeptides[11]. In consonance with this we have previously reported that the extracytoplasmic PASTA domains are indispensable for the function of PknB and survival of *Mtb*[5]. Deletion of the terminal PASTA domain (PASTA4) alone results in compromised survival[5], suggesting that it plays a leading role in kinase-ligand interactions. To date, the hypothesis with respect to PknB_{Mtb} activation has not been tested in vivo. Here we set out to answer the following questions: (i) Is PASTA4 sufficient for PknB_{Mtb} signaling?, (ii) What are the ligand binding residues in the extracytoplasmic domain?, (iii) What is the impact of abrogating ligand binding on the localization and activation of PknB?, (iv) What are the physiological ligands that interact with PASTA domains? and (v) What is the impact of abrogating ligand binding on the phosphorylation of target substrates of PknB?

Here we identify ligand interacting residues and show that mutating these residues caused abolition of ligand binding. Abrogation of ligand binding triggers aberrant localization and hyperactivation of PknB, which in turn results in hyperphosphorylation of both canonical and non-canonical downstream

target substrates, eventually leading to cell death. Results suggest that interaction with the ligand is critical for appropriate localization and regulation of the kinase activity.
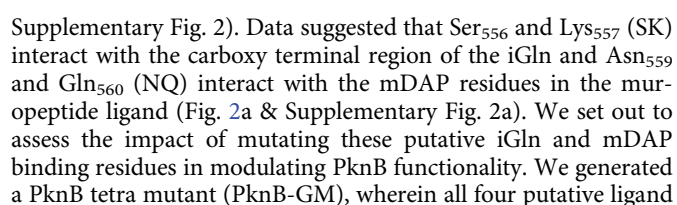
Results

PASTA4 and domain length are essential for PknB function. We have previously shown that the deletion of the PASTA4 domain (Fig. 1c; PknB-123) compromises the in vivo functionality of PknB[5]. The terminal PASTA domain of StkP, a *Streptococcus pneumoniae* ortholog of the PknB_{Mtb}, was demonstrated to be necessary and sufficient for it's signaling[16]. Thus we sought to determine the role of the terminal PASTA4 in the context of shorter total domain length. We employed previously described *Mtb* conditional mutant of *pknB* (*RvΔB*), wherein the native locus has been modified to bring its expression under pristinamycin inducible promoter, which allows the bacterium to grow efficiently in the presence of pristinamycin but not in its absence[5,17] (Supplementary Fig. 1a). To assess the effect of PknB mutations, we generated wild type or mutant constructs in pNit-3F (Supplementary Fig. 1b), which could be induced with isovaleronitrile and owing to the presence of 3X-FLAG tag, the ectopically expressed PknB migrates slower compared with the endogenous protein (Supplementary Fig. 1c).

To investigate the role of PASTA4 as well as the domain length, we have generated PknB-234, lacking PASTA1 wherein the terminal PASTA4 is retained, and PASTA-1212, a chimera of appropriate domain length where PASTA1-2 were repeated (Fig. 1c). Western blot analysis confirmed the efficient depletion of PknB in the absence of pristinamycin as well as efficient expression of 3X-FLAG tagged wild-type and mutant proteins (Fig. 1d). On examining the ability of wild-type and mutant PknB proteins to complement the in vivo functionality of PknB (Fig. 1e), it was observed that vector-transformed *RvΔB* showed significantly compromised survival in the absence of pristinamycin while the ectopic expression of 3F-PknB rescued the growth defects (Fig. 1e). Even though PknB-234 was marginally better compared to either PknB-123 or PknB-1212 (~1.5 vs 2 log fold) in rescuing the growth defects, growth was significantly compromised in all three strains when compared with the wild type (Fig. 1e). To assess the impact in an infection scenario, we evaluated the survival in differentiated THP1 cells (Fig. 1f). The data resembled the in vitro growth results, wherein PknB-234 showed slightly better survival as compared with PknB-1212 or PknB-123. These results suggest that while the PASTA4 domain is quite distinct and important, yet the appropriate length of the entire domain is also vital for efficient PknB_{Mtb} function.

mDAP and iGln interacting residues influence the survival. The structure of the PASTA domains has been derived with the help of NMR as well as X-ray crystallography[18,19]. Nonetheless, the residues that are responsible for the interaction with the proposed muropeptide ligand have not yet been identified. As PASTA4 is critical for PknB functionality, we examined a possible role for it in ligand binding. As PknB is hypothesized to dimerize upon ligand binding[14], we assumed that the PASTA domains interact with the muropeptide as a dimer. With the help of in silico molecular simulations, we identified a potential dimerization interface between the PASTA4 domains (Fig. 2a), which predominantly comprises of residues that are conserved across the PASTA4 domains of prokaryotic kinases (Supplementary Fig. 2). The initial simulation data suggested that ligand binding might be extending into the PASTA3 domain; hence, the dimeric PASTA3-4 domain was employed for further analysis. The ligand-binding domain majorly comprised of residues in the linker regions between PASTA3 and 4 domains (Fig. 2a &

Supplementary Fig. 2). Data suggested that Ser_{556} and Lys_{557} (SK) interact with the carboxy terminal region of the iGln and Asn_{559} and Gln_{560} (NQ) interact with the mDAP residues in the muropeptide ligand (Fig. 2a & Supplementary Fig. 2a). We set out to assess the impact of mutating these putative iGln and mDAP binding residues in modulating PknB functionality. We generated a PknB tetra mutant (PknB-GM), wherein all four putative ligand interacting residues have been mutated simultaneously (Fig. 2b). The $Rv\Delta B$ strain was transformed with pNit-3F-PknB and pNit-3F-PknB-GM and the expression of both proteins was confirmed (Fig. 2c). While the wild type could successfully rescue the phenotype both in vitro and ex vivo, the tetra mutant failed to do so (Fig. 2d, e). The growth phenotype did not vary even when the expression of PknB from pNit-3F constructs was not induced

Fig. 1 PASTA4 and domain length are essential for PknB function. **a** Chemical structure of suggested muropeptide ligand for PknB. **b** Schematic outline of prevailing hypothesis vis-a-vis PknB activation, wherein the ligand binding is proposed to result in dimerization and phosphorylation of the activation loop residues in the intracellular kinase domain. **c** Schematic representation of full-length PknB, PknB-PASTA domain deletion mutants, and the chimera. **d** RvΔB strain was electroporated with pNit-3F, pNit-3F-PknB, pNit-3F-PknB-123, pNit-3F-PknB-234, and pNit-3F-PknB-1212 to generate RvΔB::V, RvΔB::B, RvΔB::123, RvΔB::234, and RvΔB::1212. Whole-cell lystaes (WCLs) were prepared from cultures initiated at A_{600} of ~0.05 and grown for 5 days in the presence or absence of of pristinamycin. IVN was added in the absence of pristinamycin to the cultures to induce the expression of episomal copy. Ten microgram each of WCLs were resolved on 8% SDS-PAGE, transferred to nitrocellulose membrane, and western blotted with α-PknB and α-GroEL1 antibodies. The endogenous and episomally expressed PknB are indicated by arrow. **e** Rv and RvΔB transformants were inoculated at initial A_{600} of ~0.05 and grown in the presence or absence of pristinamycin. IVN (0.2 μM) was added in the absence of pristinamycin to the cultures to induce the expression of episomal copy. After 6 days of in vitro growth, Colony forming Units (CFU) were enumerated by plating appropriate dilutions on 7H11 agar plates containing pristinamycin. Data is representative of three biologically independent experiments with each experiment being performed in triplicates. **f** Rv and RvΔB transformants grown in the presence of pristinamycin till A_{600} of ~0.6–1.0 were washed thrice with PBS to remove inducer. These cultures were used to infect differentiated THP-1 human macrophages at 1:10 M.O.I. IVN was added in the media to induce the expression of episomal copy and CFUs were evaluated 72 h post infection (p.i). Data are representative of one of the two biologically independent experiments and each experiment was performed in triplicates. Statistical analysis was performed with the unpaired t-test using Graphpad software. Data shown represents mean + standard deviation (SD). **p < 0.005, ***p < 0.0005. Source data are provided as a Source Data file

with isovaleronitrile, suggesting that the results are not due to overexpression artifacts (Supplementary Fig. 2b, c). Thus, putative iGln and mDAP interacting residues in the PASTA domain of PknB seem to be necessary for its functionality.

iGln/mDAP interacting residues are independently essential. Next we sought to assess the impact of individually mutating the amino acid pairs, which we believed to interact with iGln or mDAP residues. Hence we generated PknB-G and PknB-M, wherein **SK** or **NQ** residues were mutated to **AA** or **DE** residues, respectively (Fig. 3a). Western blot showed efficient expression of 3F-PknB, 3F-PknB-G, and 3F-PknB-M in the complemented strains (Fig. 3b). Compared with the tetra mutant (Fig. 2d), strains complemented with either PknB-G or PknB-M showed partial growth defects, albeit to different extents (Fig. 3c, e). PknB-G (RvΔB::B-G) showed one and half-fold poorer survival compared with PknB (RvΔB::B), while it showed ~3 log folds better survival compared with the control (RvΔB::V) (Fig. 3c). On the other hand, PknB-M (RvΔB::B-M) showed 3 log fold lower survival compared with RvΔB::B and one and half-log-fold better survival compared with the control (Fig. 3e). These results suggested that mDAP interacting residues play a more critical role compared with iGln interacting residues. However in a THP1 infection model (Fig. 3d, f), both the mutants were equally abrogated and showed defects similar to the tetra mutant (Fig. 2e). THP1 infection experiment performed at lower MOI (1:4) showed similar defects as those observed at higher MOI (1:10) (Figs 2e and 3d, f). Data suggests that both iGln and mDAP interacting residues are individually critical for PknB functionality, especially during the ex vivo infection scenario where even marginal perturbations in ligand binding are not endured.

Mutations in the PknB-Ec abrogate its binding to LipidII. PG synthesis at the poles and septum region involves two stages. In the first stage, which happens in the cytoplasm, LipidII is synthesized from UDP-GlcNAc precursor by sequential action of multiple Mur family enzymes[20]. LipidII is composed of N-acetylglucosamine (NAG)-N-acetylmuramic acid (NAM)-pentapeptide (stem peptide) connected to the membrane anchored decaprenyl phosphate through a pyrophosphate link (Supplementary Fig. 3a). LipidII is then translocated/flipped into the periplasmic region, which provides the NAG-NAM-pentapeptide moieties to the growing PG layer[20]. The nature of the lipid moiety, the amino acids in the stem peptides and modification in the NAG and NAM sugars, vary from species to species[21]. The Staphylococcus aureus PknB ortholog (PknB_sa) has been shown to

interact strongly with LipidII through PASTA domains (1:2 molar ratio of LipidII:PknB_sa)[22]. Thus we sought to explore the possibility of an interaction between PknB_Mtb and LipidII. Unlike S. aureus, wherein the LipidII stem peptide contains a lysine residue at the third position, the LipidII in Mtb carries mDAP at the analogous position in the stem peptide[21] (Supplementary Fig. 3a).

It is apparent from the data presented in Figs. 2 and 3 that PASTA linker mutants were defective in rescuing PknB function, which may be due to major conformational changes. To assess the conformation changes, His-tagged PknB and the mutants of extracytoplasmic PASTA domains (PknB-Ec) were purified and CD analysis was performed (Fig. 4a–c). CD analysis indicated absence of gross conformational changes in the secondary structure (Fig. 4a–c). Next we sought to examine the interaction between the PknB-Ec (Fig. 4d) and lysine- or mDAP-containing LipidII molecules (Supplementary Fig. 3b). When mDAP-containing LipidII was used in the assay, there was no detectable LipidII upon extraction at 4:1 molar ratio of PknB-Ec:LipidII, indicating a strong interaction (Fig. 4e). This interaction could be abrogated upon treating the complex with trypsin, which would degrade the protein (Fig. 4e). Interestingly, lysine-containing LipidII could not be sequestered into a complex by PknB-Ec even at a molar ratio of 8:1 (protein:LipidII; Fig. 4e). We then evaluated the ability of mutants to bind with mDAP-LipidII. It is evident from the data presented in Fig. 4f that neither double nor the tetra mutant showed any binding with the mDAP-LipidII (Fig. 4d, f). The results show that the extracytoplasmic domain of PknB_Mtb binds specifically with mDAP-containing LipidII and the binding is abrogated upon mutating ligand-interacting residues.

Abrogation of ligand binding perturbs localization of PknB. Nascent PG biosynthesis takes place at the poles and mid cell (septum) regions[23] and hence the precursors such as LipidII and muropeptides are anticipated to be concentrated at these niches. Interestingly, PknB also localizes to both polar and mid-cell regions and the extracytoplasmic PASTA domains govern the localization[11]. Thus the rational supposition would be that the localization of PknB is probably dictated by the interaction between PASTA domain and PG precursors. However, the hypothesis has not been tested till date, perhaps due to the non-availability of PknB mutants that fail to interact with the ligand. We examined the localization of GFP-PknB and GFP-PknB-GM mutants in M. smegmatis pknB conditional mutant (mc²ΔB), following the reasoning that in the absence of endogenous PknB; GFP-PknB or GFP-PknB-GM would be the sole PknB in the cell
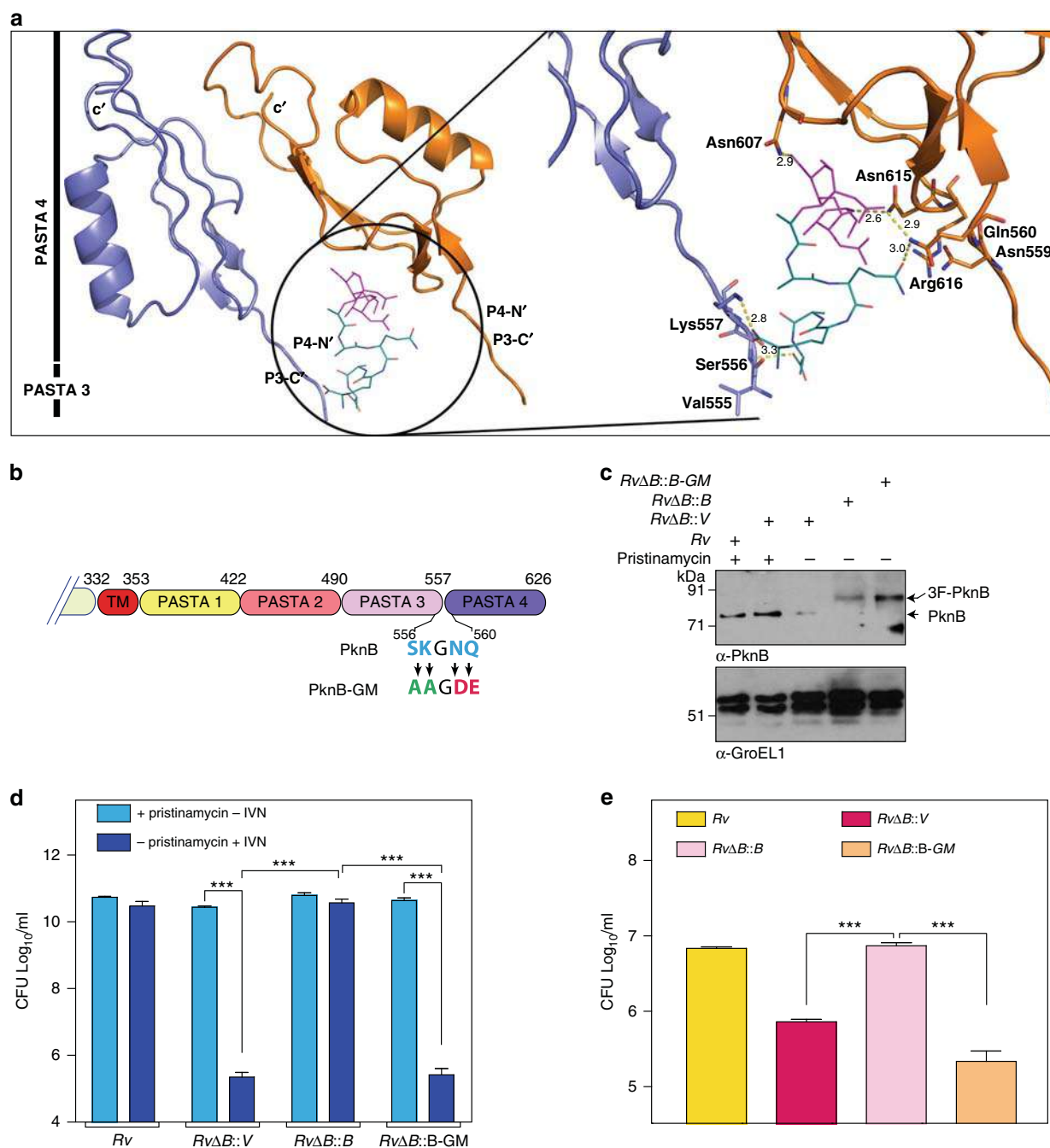
Fig. 2 mDAP and iGln interacting residues influence the survival. **a** Model of *Mtb* PknB PASTA3-4 dimer in complex with the muropeptide ligand. Inset panel shows a magnified view of the interactions between the mDAP and iGln residues of the muropeptide with polar amino acids between the PASTA3 and 4 domains of PknB. **b** Schematic representation of extra-cytoplasmic PASTA domain of PknB and the residues in the PASTA3-4 linker region suggested to be involved in interaction with iGln (SK) and mDAP (NQ) residues in the muropeptide. The mutations introduced in the linker region to generate PknB-GM are indicated. **c** Western blot analysis of WCLs prepared from *Rv* and *RvΔB* transformants. The transformants were seeded at A_{600} of ~0.05 in the presence of pristinamycin or IVN as indicated for 5 days and WCLs were resolved on 8% SDS-PAGE and probed with α-PknB and α-GroEL1 antibodies. **d** Cultures of *Rv* and *RvΔB* transformants were initiated at A_{600} of ~0.05 and grown in the presence of 1.5 μg/ml pristinamycin or 0.2 μM IVN as indicated for 6 days. CFUs were evaluated by plating appropriate dilution on 7H11 agar plates containing pristinamycin. Data are representative of the three biologically independent experiments and each experiment was performed in triplicates. **e** Human monocytic cell line THP-1 was differentiated to macrophages and was infected at 1:10 M.O.I. with *Rv* and *RvΔB* transformants grown to A_{600} of ~0.6–1.0 in the presence of pristinamycin. IVN was added in the media to induce the expression of episomal copy and CFUs were enumerated 72 h p.i. Data are representative of one of the two biological replicates and each experiment was performed in triplicates. Data represents mean + SD. Statistical analysis was performed with the unpaired *t*-test using Graphpad software. ***$p < 0.0005$. Source data are provided as a Source Data file

and hence phenotypic impact in terms of localization can be clearly visualized. Although GFP-PknB shows a strong punctate distribution at the polar and mid cell regions, GFP-PknB-GM mutant shows aberrant localization throughout the cell (Fig. 5a), suggesting that abrogation of ligand binding results in aberrant localization. Quantification of pole/septa vs. aberrant localization

drives home the message (Fig. 5b). If this was indeed accurate, the converse experiment wherein the ligand is sequestered should also result in aberrant localization. Thus, we asked what would happen to PknB localization when LipidII is sequestered into a complex with antibiotic "nisin", which binds through the pyrophosphate group resulting in membrane pore formation and
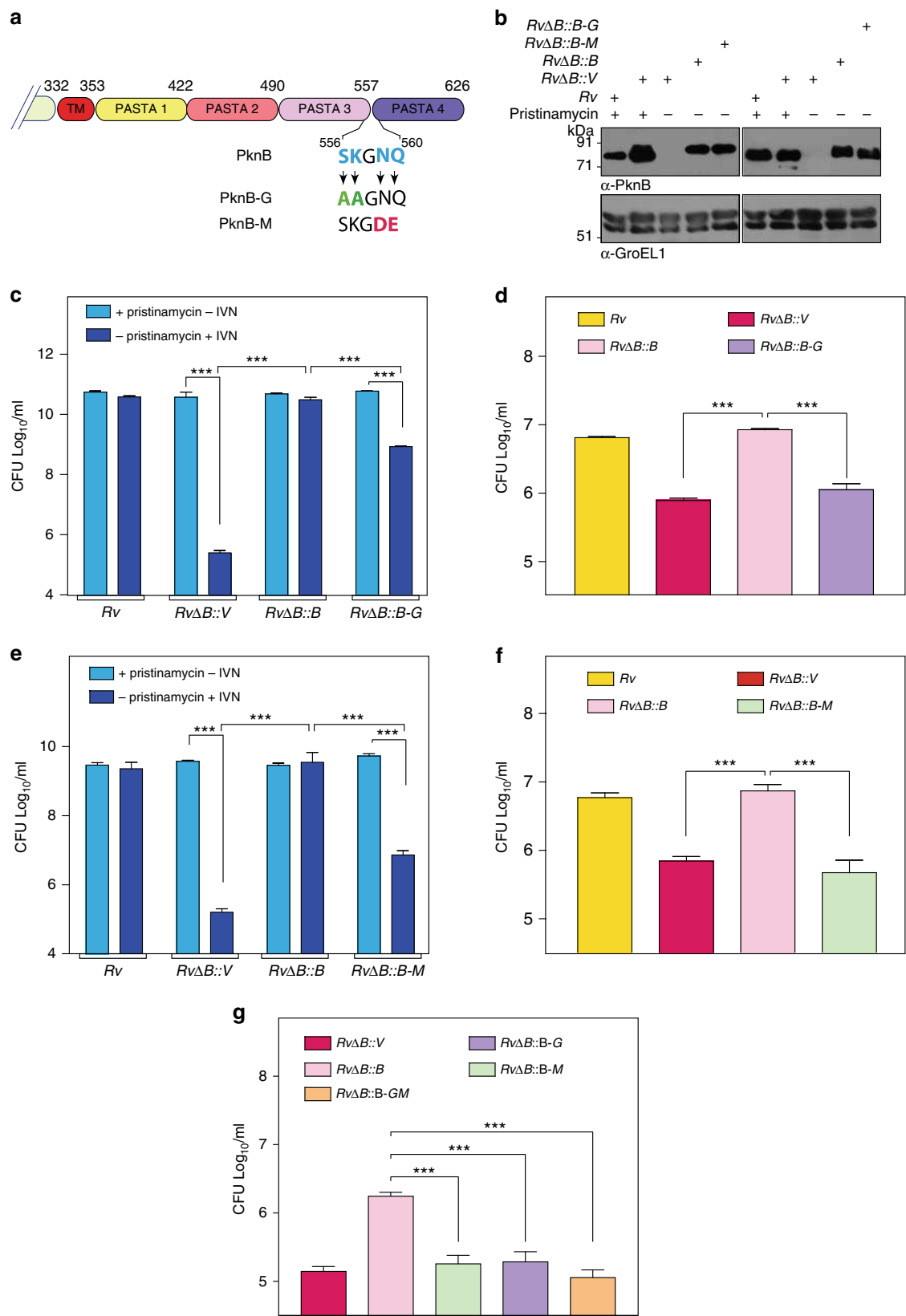
Fig. 3 iGln or mDAP interacting residues are independently essential. **a** Schematic outline of the PknB and the PknB-mutants. The mutations introduced in the linker region to abrogate either iGln (SK → AA) or mDAP (NQ → DE) binding are indicated. **b** WCLs prepared from cultures of Rv and $Rv\Delta B$ transformants inoculated at A_{600} of ~0.05 in the presence of pristinamycin or IVN and grown for 5 days were probed with α-PknB and α-GroEL1 antibodies. **c**, **e** Rv and $Rv\Delta B$ transformants were inoculated at initial A_{600} of ~0.05 and grown for 6 days in the presence of pristinamycin or IVN. CFUs were enumerateed on 7H9 plates containing pristinamycin. Data are representative of the three biologically independent experiments with each experiment being performed in triplicates. **d**, **f**, **g** Differentiated THP-1 cells were infected at 1:10 (**d**, **f**) or 1:4 (**g**) M.O.I. with Rv and $Rv\Delta B$ transformants grown to A_{600} of ~0.6–1.0 in the presence of pristinamycin. Pristinamycin was removed from cultures prior to infection by washing with $PBST_{80}$ and PBS. IVN was added in the media to induce the expression of episomal copy and CFUs were enumerated 72 h p.i. Data are representative of one of the two biological experiments and each experiment was performed in triplicates. Data represents mean + SD. Statistical analysis was performed with the unpaired t-test using Graphpad software. ***$p < 0.0005$. Source data are provided as a Source Data file

eventual cell death[24–26]. The antibiotic isoniazid (INH) that does not interact with LipidII was used as the control (Fig. 5c). Although we observed distinct puncta with $mc^2\Delta B::GFP$-B in the absence of any antibiotic or in the presence of INH, aberrant number/mislocalized puncta were observed (>3) upon nisin treatment (Fig. 5c). Quantification showed a significant increase in the number of cells with more than 3 puncta or localization all through the cell (Fig. 5d). These results suggest that LipidII is likely to be the major intracellular ligand of PknB, and importantly, ligand binding is essential for the appropriate localization. Since the PknB-GM fails to interact with the ligand and does not localize to pole and septum, we reasoned that it might impact the diffusion dynamics. We investigated the rate of recovery of GFP-PknB and GFP-PknB-GM upon photobleaching by performing FRAP (Fluorescence Recovery After Photobleaching) experiments (Fig. 5e). Although GFP-PknB showed relatively slower recovery ($t_{1/2} = 111$ s), GFP-PknB-GM mutant showed substantially higher dynamicity with $t_{1/2} = 90.56$ s (Fig. 5f), suggesting that ligand binding also plays a role in modulating molecular dynamics.

PknB-GM is hyper-phosphorylated in the activation loop. If the prevailing hypothesis with respect to the activation of PknB shown in Fig. 1b is accurate, abrogation of ligand binding should result in decreased phosphorylation of the activation loop residues. PknB is auto-phosphorylated at the T171 and T173 residues within the activation loop in vitro, and mutating these residues significantly diminishes its activity[27], (Fig. 6a). PknB is also phosphorylated in vitro in the juxtamembrane domain[27,28], (Fig. 6a); however, there are no reports about the influence of these phosphorylations its function. To scrutinize the roles of T171 and T173 residues, we generated PknB-TATA (T171A, T173A) mutant (Supplementary Figs. 4a and 6a), and the activity was analyzed using GarA as the substrate (Supplementary Fig. 4b–d). In agreement with the previous report[27], the PknB-TATA mutant showed significantly compromised activity (Supplementary Fig. 4c, d). To examine their in vivo role, PknB or PknB-TATA clones made using integrative vector as backbone were electroporated into $Rv\Delta B$ cells. The expression of PknB and PknB-TATA from the integrated construct was comparable to that of inducible PknB at the native locus (Fig. 6b). Compared with $Rv\Delta B::V$, $Rv\Delta B::B$-$TATA$ showed better survival; nonetheless, the mutant was significantly compromised when compared with $Rv\Delta B::B$, indicating the essentiality of activation loop phosphoryaltions (Fig. 6c). Importantly, in the ex vivo model of infection, both $Rv\Delta B::V$ and $Rv\Delta B::B$-$TATA$ were found to be equally compromised (Fig. 6d).

To determine the extent of activation loop and juxtamembrane phosphorylations, we resorted to isobaric TMT labeling (Fig. 6e). Western blot and quantitative mass spectrometry analysis of total proteome demonstrated depletion of PknB and similar expression of 3F-PknB and 3F-PknB-GM (Fig. 6f, g). However, the levels of PknB protein in $Rv\Delta B::B$ & $Rv\Delta B::B$-GM

were ~1.2–1.5 ($\log_2$) fold higher compared with PknB in $Rv\Delta B$ (+pristinamycin; Fig. 6g; Supplementary Table 1a). Intriguingly, contrary to the current belief, we observed hyperphosphorylation of both activation loop and juxtamembrane domain in the 3F-PknB-GM mutant compared with 3F-PknB (Fig. 6h & Supplementary Table 1b). Although the role of activation loop phosphorylation is known, the role of juxtamembrane phosphorylation needs further investigation. Thus the data suggests that abrogation of ligand binding results in hyper phosphorylation of PknB, strongly suggesting that the ligand binding plays a regulatory role.

PknB-GM hyperphosphorylates specific & non-specific targets. We identified a total of 632 (Supplementary Fig. 6a & Supplementary Data 1) and 258 (Supplementary Fig. 6b) proteins in the proteomic and phosphoproteomic samples, respectively. Of the 258 phosphoproteins, 242 had common phosphopeptides (total = 390 phosphopeptides) in all three replicates. Among them, 147 proteins encompassing 257 phosphopeptides were present in both, proteomic and phosphoproteomic samples (Supplementary Fig. 6c & Supplementary Data 2). The intensity ratios of these 257 phosphopeptides were normalized with respect to the whole-protein intensity ratios (Supplementary Data 1) and the mean normalized ratios (Supplementary Data 3) were converted to $\log_2$ values (Supplementary Table 2) and plotted as a heatmap (Fig. 7a). The 147 phosphoproteins were distributed across all the functional categories (Fig. 7b) with a majority of the phosphorylations on threonine (68%), followed by serine (~23%) and tyrosine (~9%), residues, a trend universal to all mycobacterial phosphoproteomic studies[29–31]. Among the 257 phosphopeptides, a total of 111 phosphopeptides mapping to 73 different proteins (which included multiple well-characterized substrates such as Ef-Tu, Wag31, and HupB)[8,32,33] were potentially the products of PknB-mediated phosphorylation (Fig. 7b, c; Supplementary Table 3a). Recently, Carette et al. have identified 46 potential targets of PknA and PknB with the help of a specific inhibitor[34]. Nine of these identified targets were found to be among the 73 potential targets of PknB identified in this study (Supplementary Table 3b). Interestingly, we also identified 8 putative PknB-dependent tyrosine phosphorylated peptides (Fig. 7d; Supplementary Table 4a, b), in agreement with a previous study[35] where PknB was suggested to be a dual specificity kinase.

The analysis of the activation loop phosphorylations in PknB suggested that PknB-GM is hyperphosphorylated (Fig. 6h), which led us to infer it to be a hyperactive kinase. In line with this prediction, complementation with the PknB-GM mutant seems to have resulted in the remarkable hyperphosphorylation of cellular proteins (Fig. 7a; Supplementary Table 2). The data in Fig. 7a can be further divided into three clusters (Supplementary Table 4c): cluster 1 where the phosphorylation is unperturbed by depletion of PknB as well as complementation with ectopic expression of PknB or PknB-GM; cluster 2 representing direct
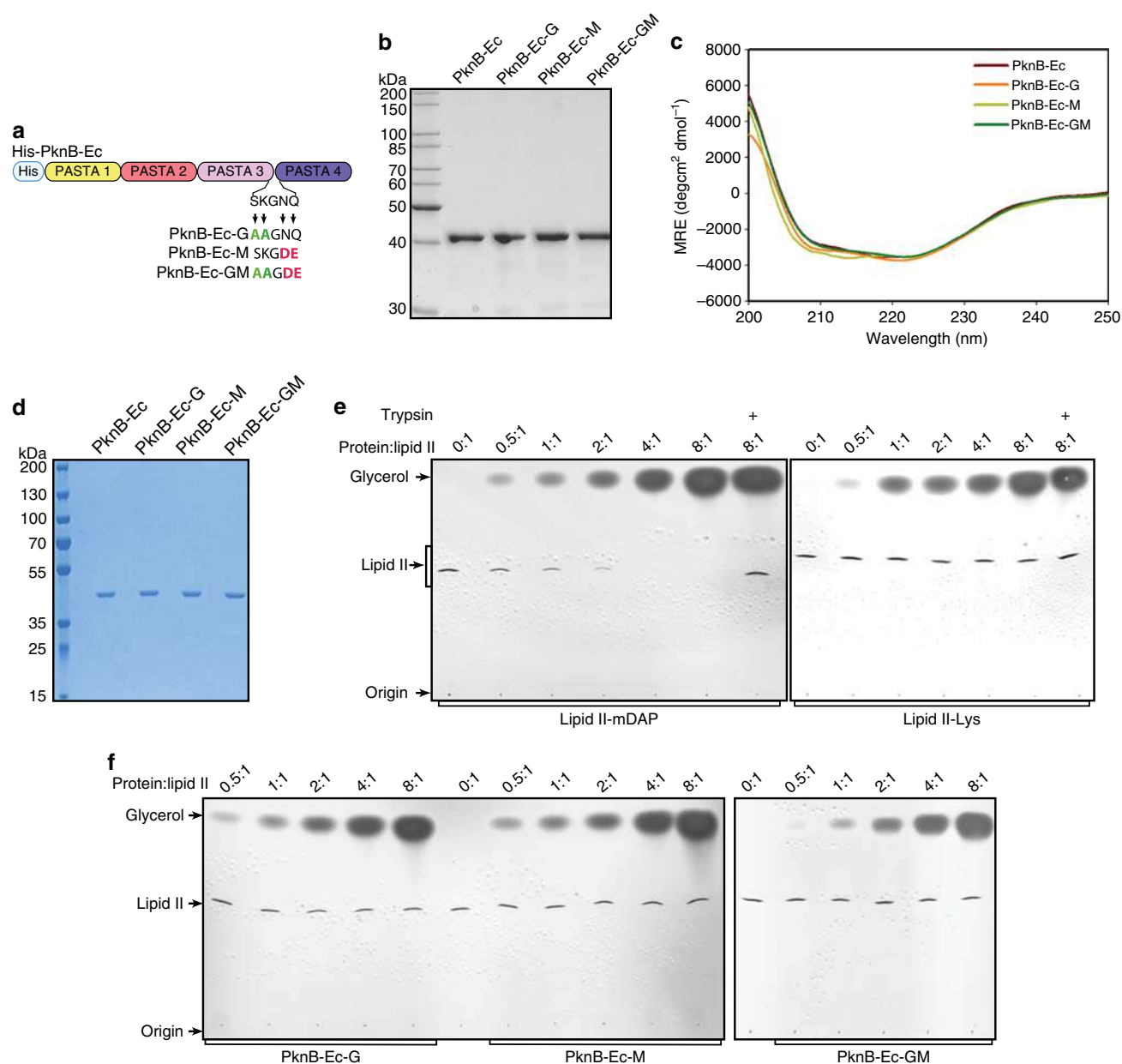
Fig. 4 Abrogation of ligand binding perturbs localization of PknB. **a** Schematic depicting hexa-His tagged extracytoplasmic region of PknB (PknB-Ec) and PknB-Ec mutants. **b** His-PknB wild type and mutants were purified as described in methods and 2 μg of purified PknB-Ec$_{wt/mutant}$ proteins were resolved on SDS-PAGE and stained with commassie. The purified proteins were used for the CD experiment in **c**. **c** CD spectrum of PknB-EC$_{wt/mutant}$ proteins in far-UV range (200–250 nm) CD data is depicted as MRE values (deg cm^2 dmol^{-1}) in the Y-axis plotted against wavelength (nm) in X-axis. **d** 1 μg each of His-PknB-Ec$_{wt/mutant}$ purified for the LipidII binding experiment were resolved on SDS-PAGE and stained with coommassie as a loading control for experiments shown in **e**, **f**. **e** 2 nmol of mDAP or Lys containing LipidIIs were incubated with increasing mole:mole ratio of His-PknB-Ec$_{wt}$ with respect to LipidII. Addition of Trypsin to degrade His-PknB-Ec$_{wt}$ in the reaction mixture is indicated. The samples were extracted with BuOH/PyrAc and resolved on TLC to analyze the presence of extractable LipidII. LipidII trapped in a stable complex with PknB Ec$_{wt}$ resides in the water phase and free LipidII is extracted and migrates to a defined position on the chromatogram. The intensity of the LipidII bands relative to the control is shown. **f** 2 nmol of mDAP containing LipidII was incubated with increasing mole:mole ratio of His-PknB-Ec$_{wt/mutant}$. The samples were extracted with BuOH/PyrAc. Addition of Trypsin to degrade His-PknB-Ec$_{wt}$ in the reaction mixture is indicated. The samples were extracted with organic solvent and resolved on TLC to analyze the presence of extractable LipidII. Source data are provided as a Source Data file

targets of PknB; and cluster 3 represents the proteins that are not the direct targets of PknB, wherein phosphorylation does not alter significantly upon depletion or complementation with the wild-type PknB. (Fig. 7e; Supplementary Table 4c). Interestingly, we observed that both cluster 2 and cluster 3 proteins were hyperphosphorylated by the mutant PknB-GM, exemplifying both specific as well as promiscuous hyperphosphorylation (Fig. 7e; Supplementary Table 4c).

Hyperphosphorylation is a result of increased activity. To confirm that mutant is indeed hyper-phosphorylated in the activation loop (Fig. 6), we raised phosphospecific antibodies that are capable of recognizing phosphorylated T171 and T173 residues (Fig. 8a). The specificity and sensitivity of the antibodies were characterized (Supplementary Fig. 5). Consistent with mass spectrometry data, we observed ~1.5-fold increase in the normalized activation loop phosphorylation in the
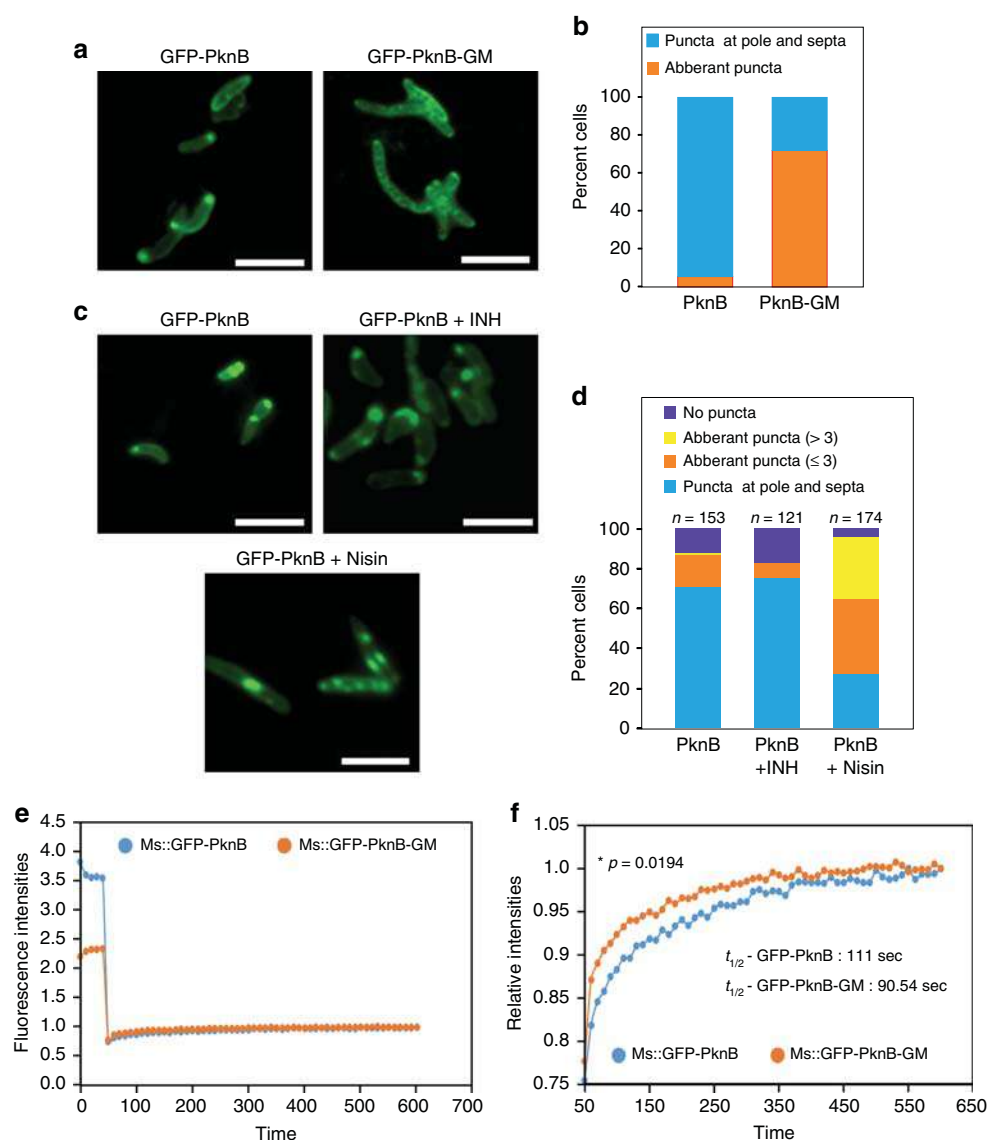
Fig. 5 Abrogation of ligand binding perturbs localization of PknB. **a** *M. smegmatis pknB* conditional mutant (*mc²ΔB*) was electroporated with pNiT-GFP-PknB or pNit-GFP-PknB-GM constructs to generate *mc²ΔB::GFP-B* or *mc²ΔB::GFP-B-GM* strains. The strains were cultured in the presence of 50 ng per ml ATc and 0.2 μM IVN till A_{600} of ~0.8. The cultures were washed thrice with $PBST_{80}$ to remove ATc and the cultures were grown for 6 hours in 7H9 media containing 1 μM IVN. Florescence images were captured using ×100 oil-immersion Zeiss Imager. M1 microscope. Scale bar- 5 μm. **b** 200 *mc²ΔB::gB* or *mc²ΔB::gB-GM* cell from **a** were analyzed for the localization of GFP-PknB$_{wt/mutant}$. The aberrant puncta collectively represents cells without any distinct localization or showing puncta at regions other than poles and septa. **c** *mc²ΔB::gB* strain cultured till A_{600} of ~0.8 were washed and grown for 3 hours in 7H9 media containing 1 μM IVN in the presence or absence of 25 μg per ml nisin or 250 ng per ml INH. Scale bar- 5 μm. **d** Between 120 and 174 cells (as indicated) of *mc²ΔB::gB* cell from **c** were analyzed for the localization of GFP-PknB$_{wt}$. The no puncta phenotype has been mentioned as a distinct feature from aberrant puncta in this case for better analysis of phenotype. Scale bar- 5 μm. **e**, **f** *M. smegmatis mc²155* strain was electroporated with GFP-PknB or GFP-PknB-GM to generate *mc²::gB* or *mc²::gB-GM*. Cultures of *mc²::gB* or *mc²::gB-GM* grown in the presence of 0.2 μM IVN were used for the FRAP analysis. **e** The graph represents the mean fluorescence intensity plotted as a function of time by normalizing the intensity at each time point (I_t) to the first time point (I_0, $t = 0$ s) i.e., I_t/I_0. The values obtained were subtracted from the intensity at the time point of bleaching (I_b). **f** The time frames from 50 to 600 s are depicted, which highlight the difference in recovery times of GFP-PknB and GFP-PknB-GM. The $t_{1/2}$ values of recovery obtained are an indication of the time taken for half the maximal recovery after bleaching in three biologically different experiments. Statistical analysis was performed with the unpaired *t*-test using Graphpad software. Source data are provided as a Source Data file

ligand binding mutant PknB-GM (Fig. 8b). GarA has previously been demonstrated to be a robust in vitro substrate for PknA, PknB, and PknG[36], hence we performed *in vitro* kinase assays with immunoprecipitated 3F-PknB and 3F-PknB-GM using GarA as the substrate. It is apparent from the data that PknB-GM showed higher activity compared with the PknB (Fig. 8c, d), which could be a combinatorial effect of higher phosphorylation of loop as well as the juxtamembrane residues. Even though GarA is a robust in vitro substrate for PknB, in in vivo it is majorly phosphorylated by PknG on T21 residue[36,37]. In agreement with this we observed that phosphorylation of GarA on T21 is unperturbed by depletion of PknB as well as complementation (Fig. 7e). On the other hand, phosphorylation of TatA on T60 was found to be PknB dependent, which showed hyperphosphorylation upon complementation with PknB-GM (Fig. 7e). In an independent
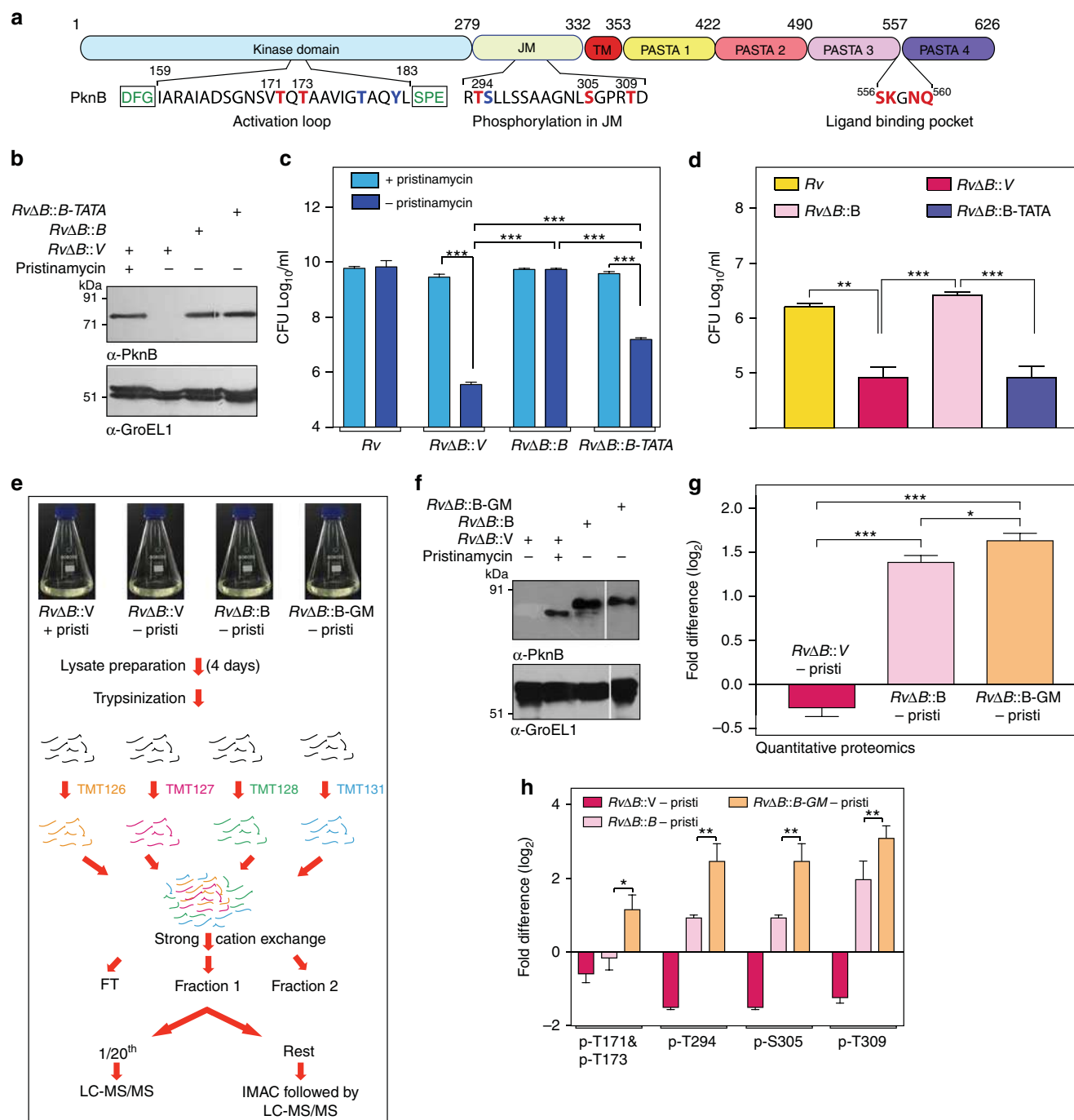
study, phosphorylation of TatA on T60 was shown to be dependent on PknA and PknB[34].

We sought to validate the data by quantitating the peak area in an independent mass spec experiment for phosphopeptides corresponding to GarA(T21) and TatA(T60). Depletion of PknB in the absence of inducer and expression of PknB and PknB-GM was confirmed by western blots (Fig. 8e). In concurrence with the TMT data (Fig. 7), phosphopeptide corresponding to GarA-T21 showed similar peak area in $Rv\Delta B$ & $Rv\Delta B::B$-GM samples, with slight decrease in $Rv\Delta B::B$ sample (Fig. 8f). On the other hand, phosphopeptide corresponding to TatA showed distinct hyper-phosphorylation in $Rv\Delta B::B$-GM compared with $Rv\Delta B$ & $Rv\Delta B::B$ (Fig. 8f). To further substantiate the data, we performed parallel reaction monitoring (PRM) to quantitate the TatA-T60

phosphopeptide (Supplementary Figs. 7 and 8g). Quantitation of TatA-T60 phosphopeptide with respect to the corresponding heavy peptide using PRM evidently demonstrated ~2-fold (31.2 fmoles) increase in its levels in $Rv\Delta B::B$-GM sample compared with $Rv\Delta B$ & $Rv\Delta B::B$ (18.6 and 16.4 fmoles) samples. Collectively, these data demonstrate that the abrogation of ligand binding perturbs the normal regulatory circuits of PknB, resulting in aberrant localization, hyperactivation of the kinase, and indiscriminate target-specific and promiscuous phosphorylation events, leading to eventual cell death (Fig. 8h)

Discussion

Since the domain structure of bacterial STPKs are similar to their eukaryotic counterparts[28,38,39], the hypotheses with respect to

Fig. 6 PknB-GM is hyper-phosphorylated in the activation loop. **a** Threonine and tyrosine residues that are be known to be phosphorylated are highlighted by red or blue color. The phosphorylations that are identified in the current study are shown in bold red. The ligand binding residues are also indicated. **b** $Rv\Delta B$ strain was electroporated with integrating pST-CiT, pST-CiT-PknB, and pST-CiT-PknB-TATA to generate $Rv\Delta B::V$, $Rv\Delta B::B$, and $Rv\Delta B::B$-TATA, respectively. The transformanats grown in the presence of pristinamycin were seeded at A_{600} of ~0.05 and grown for 5 days in the presence or absence of pristinamycin. WCLs were resolved on SDS-PAGE and probed with α-PknB and α-GroEL1 antibodies. **c** Cultures of Rv and $Rv\Delta B$ transformants were inoculated at A_{600} of ~0.05 and grown in the presence or absence of pristinamycin for 6 days and CFUs were enumerated. Data are representative of one of the three biological experiments and each experiment was performed in triplicates. **d** Cultures of Rv and $Rv\Delta B$ transformants grown till A_{600} of ~0.6–1.0 were washed thrice and used for infecting differentiated THP-1 cells (1:10 M.O.I). CFUs were enumerated at 72 h p.i. on plates containing pristinamycin. **e** Outline of the protocol used for TMT-based quantitative phosphoproteomics analysis. **f** $Rv\Delta B$ transformed with pNit-3F or pNit-3F-PknB or pNit-3F-PknB-GM were grown in presence of pristinamycin or IVN for four days and WCLs prepared were probed with α-PknB and α-GroEL1 antibodies. **g** The absolute PknB levels in depleted and complemented strains were assessed by quantitative TMT-based proteomics approach. Each data point is represented by TMT intensities obtained from three technical replicates. Data represents mean + SD. *$p < 0.05$, ***$p < 0.0005$. **h** The levels of phosphorylation of various residues in PknB activation loop and juxtamembrane regions were estimated from the TMT experiment. Phosphorylated peptides from three replicates normalized to their corresponding PknB protein intensities were considered for this analysis. The data is represented as log2 values and the raw data of the experiment is presented in Supplementary Table 1. Data represents mean + SD. Statistical analysis was performed with the unpaired t-test using Graphpad software. *$p < 0.05$, **$p < 0.005$, ***$p < 0.0005$. Source data are provided as a Source Data file

their activation and regulation are influenced by the findings in eukaryotic kinases. There are two major mechanisms by which the activity of a protein kinase is regulated: (a) by modulating protein expression levels and (b) by limiting the levels of activity through phosphorylation and dephosphorylation of the activation loop residues. In case of PknB, the following findings have cumulatively led to the formulation of the activation mechanism hypothesis presented in Fig. 1b: (i) $PknB_{Mtb}$ is autophosphorylated in the activation loop and this phosphorylation is necessary and sufficient for its activity in vitro[27], (Supplementary Fig. 4). (ii) $PknB_{Mtb}$ forms both back-to-back[15] and front-to-front PknB[14] dimers, and dimerization is a pre-requisite for activation loop phosphorylations[13] (iii). The PASTA domain interacts with mDAP-containing muropeptides, and this domain is adequate for appropriate localization of the protein[11]. Interestingly, PknB protein expression levels are downregulated during dormancy[9] and nutrient starvation[10] and are upregulated during exponential growth[8] and resuscitation[9], suggesting that PknB activity may also be regulated through the modulation of its expression pattern.

The PASTA domains across the bacterial kingdom share a highly conserved globular structure, although their sequences are diverse[40]. Various PASTA kinases have been demonstrated to harbor specific unique features. For example, a conserved arginine in PASTA3 has been shown to be a determining factor for ligand-binding in PrkC, the *Bacillus subtilis* PknB ortholog[41]. Similarly, three putative muropeptide binding sites in the hinge regions have been suggested to be the ligand binding pockets in StkP[42]. Recently, a unique citrate-binding site[19] and a hydrolase (LytB)-binding region[16] have been defined in the terminal PASTA domains of PknB and StkP, respectively, thus implicating other roles for the domain in addition to muropeptide binding. In *S. pneumoniae*, the terminal PASTA domain of StkP is both necessary and sufficient for its function[16]. In *Mtb*, we have previously reported that the terminal PASTA4 is absolutely essential for the function of PknB[5]. However, unlike in *S. pneumoniae*, we observe that the terminal PASTA4 is not sufficient; rather, appropriate length of the total PASTA domain is also vital (Fig. 1). The fact that PASTA4 plays an indispensible role is reinforced by the finding that SK and NQ residues in the PASTA3-4 linker region, serve as the putative ligand interacting residues (Fig. 2). In contrast to the tetra mutant that shows a drastic phenotype (Fig. 2), we observed varying levels of compromise in case of double mutants, with the data suggesting a greater role for mDAP-interacting residues compared with iGln-interacting residues (Fig. 3). Interestingly, both the double mutants as well the tetra mutant are similarly compromised in

their ability to functionally complement PknB depletion ex-vivo, suggesting that PknB plays a very stringent role at the time of infection and under these circumstances even minor perturbations are not tolerated (Figs. 2 and 3).

Muropeptides are widely acknowledged as the ligands for the PASTA domains of $PknB_{Mtb}$[11,12]. However, some experimental observations suggest that they may not be the primary ligand: for example, in vitro binding affinity of muropeptides to purified PknB-Ec is relatively weak, with micromolar concentrations of muropeptide being required for the binding[2,11,12], and the growth inhibition due to overexpression of PknB-Ec could not be ameliorated upon the addition of muropeptides mixtures[43]. Optimal binding occurs only when the MurNAc sugar and the stem-pentapeptide (muramyl pentapeptide) are present in the ligand. The other possible source of PknB ligand is peptidoglycan precursors such as LipidII, also present in the periplasmic space. LipidII possesses all the signatures of the muropeptide ligand and is also spatio-temporally localized to the same niche as PknB. In line with this, $PknB_{sa}$ was recently shown to bind very efficiently with LipidII molecules[22]. Our data also demonstrates efficient binding of PknB-Ec with mDAP-LipidII (Fig. 4). The weaker binding affinity compared to $PknB_{sa}$ could be either due to the fact that we tested only the PknB-Ec, or could be due to the lack of additional modifications (such as amidation), known to be present in mDAP as well as iGlu residues in *Mtb*[44]. Importantly, all three PknB-Ec mutants failed to interact with the mDAP-LipidII, clearly showing abrogation of ligand binding (Fig. 4).

The extracytoplasmic PASTA domain by itself has previously been shown to be sufficient for appropriate localization of PknB, which suggested that the interaction of this domain with the ligand may dictate the localization[11]. The data presented in Figs. 4 and 5 of this study suggest that LipidII may be the primary intracellular ligand, as incubating the cells with sub-lethal doses of the drug "nisin" results in an aberrant distribution pattern of PknB in the cell. Previous studies have shown that the addition of purified intracellular PASTA domain to the culture also inhibits the growth of *Mtb*[43]. Considering this fact with the data in Fig. 5, it is evident that incubating the cells with purified extracytoplasmic PASTA domain or nisin results in sequestration of available LipidII, thus compromising the functionality of PknB. The NMR structure of PASTA domain suggests that it is a linear domain. It is not clear as to how the muropeptide moiety in the LipidII interacts with the linear PASTA domain. It is possible that the interaction occur once the muropeptide is cleaved from the decaprenyl moiety. Alternatively, in the cellular context the PASTA domains may not be linear in structure. The regulation
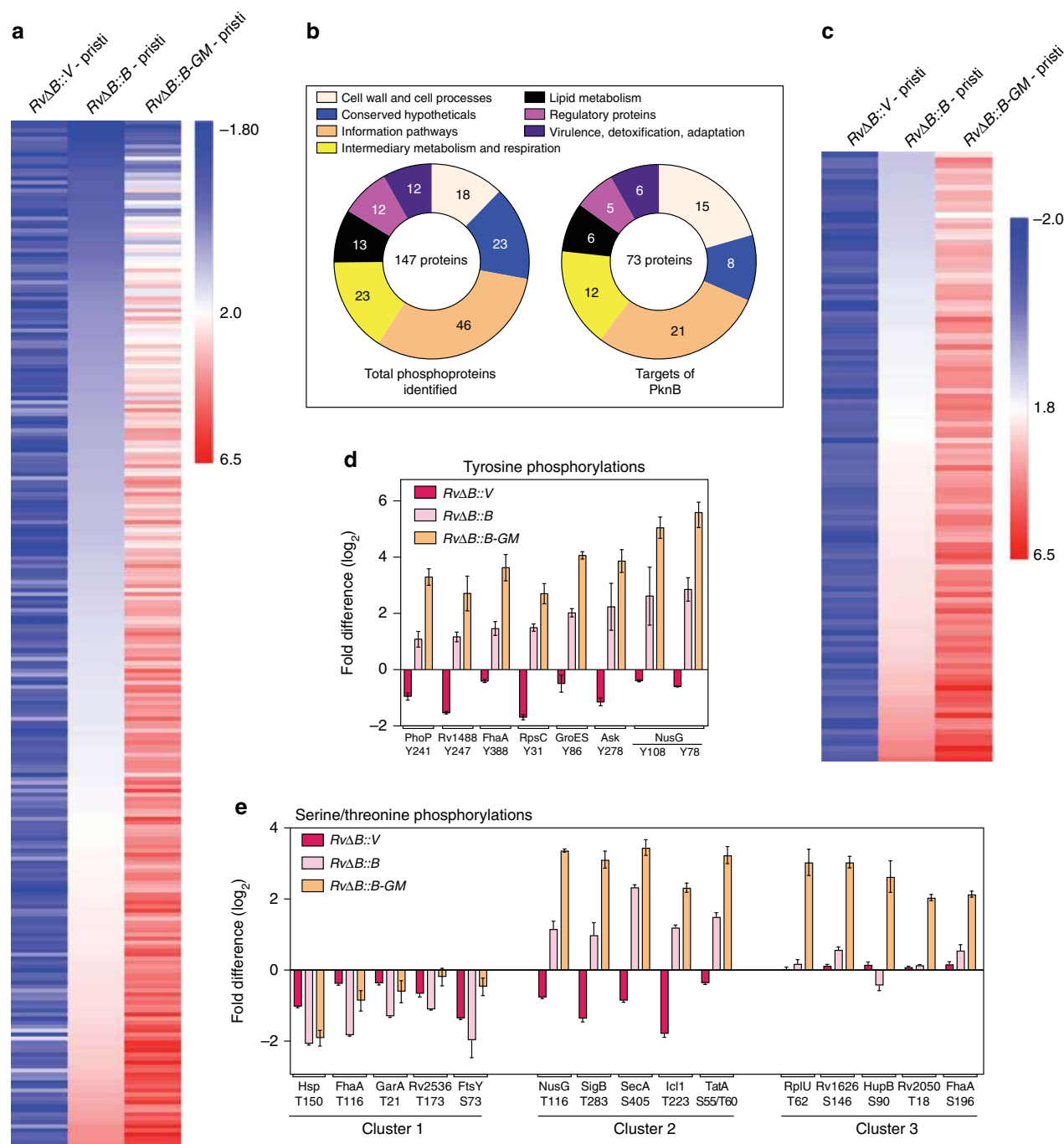
Fig. 7 Ligand binding mutation causes global hyperphosphorylation of specific and non-specific targets. **a** TMT intensities of phosphopeptides in $Rv\Delta B$ -pristinamycin (PknB depleted sample, labeled with TMT 127) or in $Rv\Delta B::B$ (complemented with 3F-PknB, labeled with TMT 128) or $Rv\Delta B::B$-GM (complemented with 3F-PknB-GM, labeled with TMT131), with respect to $Rv\Delta B$ +pristinamycin as the reference comparator (control strain, labeled with TMT 126). The intensities of phosphopeptides in each case were normalized with respect to the corresponding absolute protein intensities and the values were converted to log2 values. Data were sorted with respect to $Rv\Delta B::B$ sample and heatmap of the data were generated using online tool Morpheus. **b** The 257 phosphopeptides detected in TMT experiment belonged to 147 unique proteins, which were classified according to their functional category with reference to mycobrowser database. The phosphopeptides were categorized as probable PknB substrates if the TMT $\log_2$ phosphointensity upon depletion was <-0.32 and upon complementation was >1. 111 phosphopeptides were classified as probable PknB substrates, which belonged to 73 unique proteins. The 73 PknB targets were also functionally characterized according to mycobrowser database. **c** Normalized TMT intensities of all 111 phosphopeptides which are probable PknB targets were converted to $\log_2$ values and data were sorted with respect to $Rv\Delta B::B$. Heatmap was generated using online tool Morpheus. **d** Normalized TMT intensities of 5 phosphopeptides each belonging to cluster 1, cluster 2, and cluster 3. **e** Normalized TMT intensities of PknB-dependent tyrosine phosphorylations are represented. Source data are provided as a Source Data file
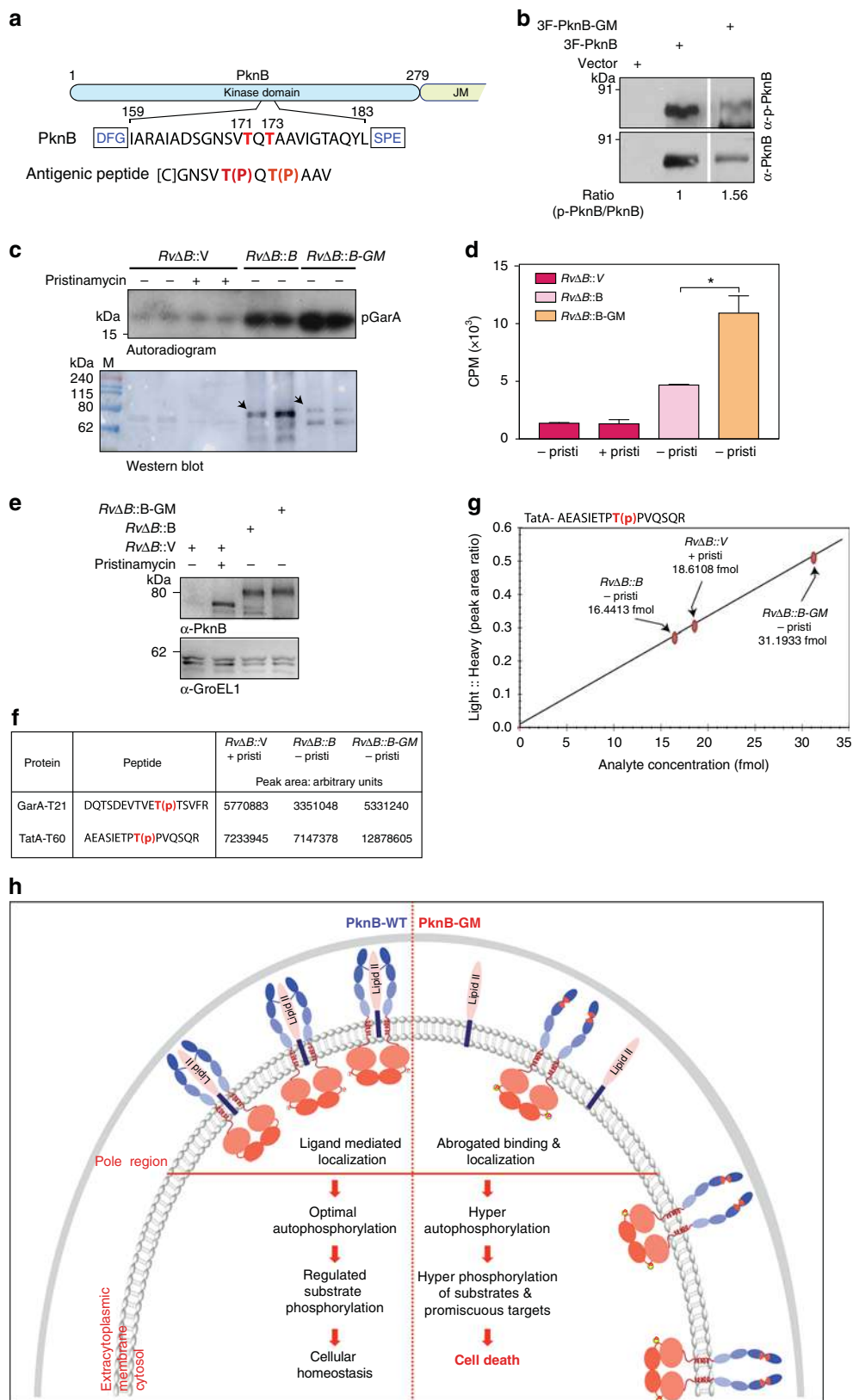
of the synthesis and continuous remodeling of PG is a fundamental process of the bacterial cell involving multiple proteins. PknB$_{Mtb}$ is a well-known modulator of multiple substrates involved in cell division and cell wall synthesis, phosphorylating MviN and FhaA proteins among others, a molecular event that is linked to reduced PG biosynthesis[45,46]. Thus, a feedback loop regulation mechanism intertwining PknB activity and peptidoglycan synthesis may exist.

Fig. 8 Hyperphosphorylation is a result of increased activity of the PknB-GM mutant. **a** Schematic outline showing the activation loop region of PknB and the peptide sequence used for generating phospho-specific antibodies. **b–d** WCL were prepared from $Rv\Delta B$::V grown in the presence and absence of pristinamycin; $Rv\Delta B$::B and $Rv\Delta B$::B-GM grown in the absence of pristinamycin and in the presence of IVN for 4 days. **b** 3F-PknB or 3F-PknB-GM proteins were immunoprecipitated from 1 mg WCLs using FLAG-M2 beads and 1/10th of IP was probed with α-PknB antibodies and 9/10th of IP was loaded for α-pPknB antibodies. The ratio of signal from total PknB and phospho-PknB was evaluated with the help of imageJ. **c** In vitro kinase assays samples were resolved on 15% SDS-PAGE, transferred to nitrocellulose membrane and autoradiographed. Upper part of the membrane corresponding to 40–240 kDa was probed with α-PknB antibody. **d** The bands corresponding to p-GarA (~17 kDa) were excised from the membrane described in **c** and counts per minute (CPM) were determined (right panel). **e** 5 mg WCL prepared from $Rv\Delta B$::V +pristinamycin; $Rv\Delta B$::B −pristinamycin+IVN and $Rv\Delta B$::B-GM -pristinamycin+IVN cultures grown for 4 days were digested with trypsin, and phosphoenriched. **f** We determined the peak area for GarA-T21 and TatA-T60 phosphopeptides using targeted proteomics. Table shows the total integrated area of GarA-T21 and TatA-T60 phosphopeptide in the samples. **g** Determination of absolute endogenous TatA-T60 phosphopeptide amounts in the samples by PRM. Graph showing absolute endogenous TatA-T60 light phosphopeptide concentration (fmoles) in phosphoenriched samples with respect to the standard curve generated by measuring peak area of different concentrations of heavy standard peptide (Supplementary Fig. 7). The horizontal axis represents Light: Heavy phosphopeptide integrated peak area ratios determined by skyline software. The vertical axis represents the absolute endogenous phosphopeptide TatA-T60 analyte concentration in fmoles. **h** Model depicting PknB regulation wherein LipidII interacts with specific region of PASTA 3-4 linker region of PknB and defines its localization to polar/septal niches and regulates the activity to optimal levels and hence maintains cellular homeostasis and cell survival. Source data are provided as a Source Data file

If the ligand binding is required for the activation of PknB, abrogation of binding should result in compromised loop phosphorylation. Contrary to this supposition, we observed significant hyperphosphorylation of activation loop and juxtamembrane regions in the PknB-GM mutant (Fig. 6). PrkC$_{bs}$ localizes to the division site and interacts and phosphorylates GpsB, which in turn regulates its activity by inhibiting its auto/transphosphorylations[47]. We hypothesize that upon binding of ligand, the kinase would be localized to the appropriate niche, whereupon a combination of other regulatory proteins/partners (including PstP) would ensure tight regulation of autophosphorylation levels, and by extension, kinase activity. In consonance, results (Fig. 8) showed that 3F-PknB-GM to be a more active kinase compared with 3F-PknB. The mis-regulated kinase results in hyperphosphorylation events targeting proteins, which are both canonical and non-canonical substrates that may be leading to aberrant functionality, leading to eventual death (Fig. 7). PRM analysis showed ~2-fold increase in the phosphorylation of the substrate of TatA on T60 residue upon complementation with PknB-GM, thus validating the data (Fig. 8). There are few examples in literature wherein phosphomimetic mutant of PknB substrates such as InhA, KasB, PcaA, and CwlM have been shown to have significant impact on the catalytic function and/or survival defects[46,48–51]. Complementation with phosphomimetic mutant of KasB (T334D/T336D) results in loss of acid fastness character and also causes loss of virulence[50]. Phosphomimetic mutant of InhA (T266E) fails to rescue Msmeg/Mtb inhA conditional mutant upon depletion[48,49]. PcaA-T168D/T183D phosphomimetic mutant shows reduced bacterial survival and defective mycolic acid profile[51]. Recently, a double phosphomimetic mutant of a major substrate of PknB, CwlM (T382D + T386D) was shown to be defective in complementing the mutant strain[46].

The hyperphosphorylation of the juxtamembrane domain could be linked to the hyperphosphorylation of the activation loop. Although the specific role of PknB juxtamembrane phosphorylation is unknown, it might be critical for transducing the ligand-mediated signal to the intracellular kinase domain, or for recruitment of regulatory interacting partners. Based on in vitro phosphorylation assays, Sassetti's group suggested that PknB and PknH are master regulators that are capable of phosphorylating multiple other kinases[6]. It is possible that promiscuous hyperphosphorylation could be due to aberrant activation of other STPKs by mislocalized PknB. Even though, we did not find any other STPKs in our final phosphoproteome, we cannot negate this prospect. These aspects need further investigation. Future PknB interactome studies may provide possible insights into how PknB activation loop and juxtamembrane phosphorylations are regulated.

Methods

Generation of plasmid constructs. *pknB* was amplified from the genomic DNA of *Mtb* and the amplicon was cloned into NdeI-HindIII sites of pNit-1[52] and pNit-3F vectors to generate pNit-B and pNit-3F-B, respectively. *PknB* upto transmembrane region (NdeI-SapI) and *PASTA-234* (SapI-HindIII) were PCR amplified and the digested amplicons were ligated with NdeI-HindIII digested pNit-3F to generate PknB-234. Similarly, *pknB-12* and *PASTA-12* were ligated with pNit-3F to generate PknB-1212. PknB activation loop mutants and PASTA point mutants were generated by overlapping PCR. The codon optimized nucleotide sequence of superfolder *gfp* was commercially synthesized from Genscript. *pknB or pknB-GM* were amplified using specific primers containing SapI and HindIII sites, and *sgfp* was amplified from pUC57-sGFP using specific primers containing NdeI and SapI sites. The amplicons were digested and ligated with pNit-3F vector digested with NdeI-HindIII to generate pNit-GFP-PknB and pNit-GFP-PknB-GM. The extracytoplasmic domain of *pknB*$_{wt/mutant}$ was PCR amplified using pNit-3F-PknB$_{wt/mutant}$ as the template and the amplicons were digested with BamHI-HindIII and cloned into corresponding sites in pET28a vector to generate pET-*pknB-Ec*, pET-*pknB-Ec-G*, pET-*pknB-Ec-M*, and pET-*pknB-Ec-GM*. Oligonucleotides and strains used in the study are described in Supplementary Material.

Analysis of growth, isolation of lysates, and western blot. *pknB* conditional mutants, *mc²ΔB* and *RvΔB* (Rv-pptr-B)[5,17] were electroporated with pNit, pNit-3F or pST-CiT[53] derived constructs (Supplementary Material). Transformants were grown in 7H9 media containing ADC (10%) and pristinamycin 1A (1.5 μg per ml; Molcon Corp) till A$_{600}$ reached ~1.0. To determine the ability of mutants to rescue growth, the cultures were washed thrice with equal volumes of PBST$_{80}$ (1X PBS with 0.05% tween 80), diluted to A$_{600}$ of ~0.05, and grown for 6 days in the presence or absence of 1.5 μg per ml pristinamycin or 0.2 μM isovaleronitrile (IVN). CFUs were enumerated after 6 days of growth. To evaluate the expression of 3X-FLAG tagged wild type and mutant PknB proteins, the transformants were grown in the absence of pristinamycin and presence of IVN for 5 days and probed with anti-PknB (α-PknB), anti-phosphoPknB (α-pPknB), or anti-GroEL1 (α-GroEL1) antibodies. α-PknB and α-GroEL1 antibodies were raised in rabbits and were used at 1:10,000 dilutions. The rabbit polyclonal phospho-specific antibodies were custom generated by PhosphoSolutions (Aurora, CO) using the antigenic peptide "[C]GNSVT(P)QT(P)AAV", a sequence derived from the PknB activation loop. For the α-pPknB blot the membrane was blocked with 5% BSA followed by overnight incubation with α-pPknB (1:250 dilution in 5% BSA) at 4 °C. Monoclonal α-FLAG M2 (Sigma-F1804) antibody was used at 1:2500 dilution.

THP-1 infections. *Rv* or *RvΔB* transformants grown up to A$_{600}$ of ~0.8 in the presence of 1.5 μg per ml pristinamycin were washed once with PBST$_{80}$ and twice with PBS to remove Tween$_{80}$ and pristinamycin and the cells were passed through 27 G needle syringe to make them into single-cell suspension. Human monocytic THP1 cells (ATCC-TIB-202) were cultured in RPMI (Hyclone) supplemented with 10% FBS (Invitrogen). THP1 infections were performed with 5×10^5 cells seeded in 24-well plates that were differentiated with 10 nM PMA for 24 h. Differentiated cells were allowed to recover for 12 h prior infection with Mtb at 1:10 or 1:4 MOI[54]. The extracellular bacteria were removed 4 h post infection by washing the cells thrice with sterile PBS, and this was considered as the zero time point. 0.2 μM IVN was added in the media wherever *RvΔB*::B$_{wt/mutant}$ transformants were used for the infection. Cells were lysed in 1 ml of 0.1% triton-X100 at 0 and 72 h post infection and CFUs were enumerated on 7H11 plates containing 1.5 μg per ml pristinamycin.

Identification of the muropeptide binding site. The coordinates of the PASTA domains of mycobacterial PknB were obtained from the NMR structure (2KUI)[18]. The two monomeric PASTA3-4 domains were subjected to protein-protein docking using HADDOCK web server[55,56]. Surface exposed hydrophobic residues – Met586, Val593, Val604, and Ile619 – were treated as active residues. To investigate possible binding modes of muropeptide to the dimeric model of PASTA3-4 domains, muropeptide (N-acetylglucosaminyl-N-acetylmuramyl-ala-iso-Gln-meso-diaminopimelic acid-ala-ala; Molecular formula: $C_{40}H_{67}N_9O_{21}$) was docked using AutoDock4[57]. Coordinates of the muropeptide were generated using the Babel program of Open Babel package[58] and PyMOL software was used for visualization (The PyMOL Molecular Graphics System, Version 1.5.0.4 Schrödinger, LLC). The ligand was allowed maximum possible flexibility with 27 rotatable bonds and Gasteiger atomic charges assigned to it. Coordinates of dimeric model of PASTA3-4 domains were kept rigid, and the ligand was allowed to explore the entire surface through the construction of a grid box, within the docking grid of $60 \times 45 \times 29$ Å[3] with a grid spacing of 0.475. The docking simulation involved 27,000 generations, and population size of 150 in each genetic algorithm (GA) run. Energy evaluations were carried out 2,500,000 times, and one best individual was chosen from each iteration of the 250 Lamarkian search GA runs. The rate of genetic mutations and cross-overs were set to 0.02 and 0.8, respectively. The most stable binding mode of the ligand had a free energy of binding of −4.29 kcal per mol. The ligand-receptor interface on the PASTA dimer was defined as residues from each of the PASTA3-4 monomers, which had at least one atom within 5 Å of any atom of the ligand.

Purification and circular dichroism. *E. coli* BL21(DE3) (Stratagene) cells transformed with the appropriate recombinant plasmid (pET28a-*pknB*-Ec, pET28a-*pknB*-Ec-G, pET28a-*pknB*-Ec-M, and pET28a-*pknB*-Ec-GM) were grown in 1 L LB-medium (50 μg per ml kanamycin) at 37 °C. At an A_{600} of 0.6, IPTG was added at a final concentration of 1 mM to induce expression of the recombinant proteins at 30 °C. The purification of hexa-His tagged protein was performed as described earlier[48]. Jasco J-815 spectopolarimeter was used for analyzing the ellipticity changes for each protein in far-UV (195–250 nm) wavelength range at 20 °C. The ellipticity changes were converted into MRE (Molar residual ellipticity) values and plotted against wavelength using SigmaPlot version 10.0.

In vitro LipidII interaction studies. In vitro LipidII binding assay was performed using purified His_6-PknB-Ec_{wt} or PknB-$Ec_{mutants}$. His_6-PknB-Ec_{wt} or PknB-$Ec_{mutants}$ were incubated with 2 nmol LipidII at molar ratios ranging from 0.5 to 8:1 (PknB:LipidII) in 50 mM Tris/HCl pH 7.0, 5 mM $MgCl_2$, 60 min at 30 °C[22]. The reaction mixture was extracted with an equal volume of butanol/pyridine acetate (2:1; vol:vol; pH 4.2) and analyzed by thin layer chromatography (TLC)[22]. For tryptic digestions, 25 μg trypsin (Gibco) were added thereafter, and the mixture was incubated at 37 °C for 60 min.

Fluorescence microscopy. $mc^2\Delta B$ strain was electroporated with pNit-GFP-PknB or pNit-GFP-PknB-GM and the colonies exhibiting optimal GFP fluorescence were chosen. The cultures supplemented with 50 ng per ml ATc and 0.2 μM IVN (for inducing sGFP-PknB) were initiated at A_{600} of ~0.025. After 12 h of growth cultures were washed twice with $PBST_{80}$ and supplemented with 7H9 containing 1 mM IVN. The cultures were withdrawn at 3 and 6 h post depletion of native *pknB* and fixed with 4% PFA for microscopic analysis. The fixed cultures (5 ml) were washed twice with 1X PBS and re-suspended in 100 μl PBS and 5 μl of fixed cultures were placed under a coverslip on a glass slide and observed in epifluorescence microscope at ×100 oil immersion using 488 nm excitation wavelength. For antibiotic treatment experiment, washed cultures supplemented with 7H9 media containing 1 mM IVN in the presence of 25 μg per ml nisin or 250 ng per ml INH were grown for 3 h prior to fixation and microscopy.

FRAP measurements. Cultures of mc^2-155 electroporated with pNit-GFP-PknB or pNit-GFP-PknB-GM ($mc^2::GFP$-PknB or $mc^2::GFP$-PknB-GM) were seeded at A_{600} of ~0.05 and expression of GFP-PknB/PknB-GM was induced with 1 μM of IVN for 16 h at 30 °C. For imaging, 100 μl of culture spotted on a glass bottom dish and low-melting agarose (1% in 7H9) was layered and allowed to settle and dry before FRAP measurements. For FRAP experiments, the bacilli containing the GFP signal were focused and one end of each bacteria (covering 30–50% area) was photo bleached using a 488 nm laser at 100% output power using a 3i vector system (3i, USA) mounted on the Olympus IX83 inverted microscope, controlled using the Slidebook 6.0 software. The fluorescence recovery was measured by time-lapse imaging in the GFP channel (488 nm excitation through a SpectraX light engine and emission filter of 510/20 nm), using the ×60 1.35 NA plan-apochromat lens. The images were acquired using a Cascade II EM-CCD camera (Photometrics, USA) with EM gain for a total duration of 10 min with 10 s interval between two successive frames[59]. To plot the fluorescence recovery kinetics, the intensity normalized at each time point (I_t) to the first time point (I_0, $t = 0$ s). The values obtained were subtracted from the intensity at the time point of bleaching (I_b) [= $(I_t/I_0) − I_b$], allowing the recovery to be recorded with respect to I_b. The polar regions of ~120 cells for each sample were photo-bleached at the fifth frame (50 s) and the fluorescence recovery was monitored up to 600 s from at least three

biologically independent experiments. The mean relative intensity obtained was plotted as a function of time (in seconds) to calculate the rate of recovery ($t_{1/2}$, the time taken to attain half of the maximum intensity) in the bleached areas of each bacterium and plotted using the Non-linear fit equation in Prism 6.0.

Immunoprecipitation and in vitro kinase assays. $Rv\Delta B$ strains electroporated with pNit-3F-PknB$_{WT/GM}$ were inoculated at A_{600} of ~0.05 and were grown in the absence of pristinamycin and presence of 0.2 μM IVN for 72 h. Cultures were centrifuged at 4000 rpm for 5 min and the pellets were resuspended in PBSG (PBS containing 5% glycerol) at 1:3 (pellet weight in g:PBSG volume in ml) ratio. Cells were lysed using 0.1 mm zirconium beads (Biospec) for 10 1 min cycles with 1 min intervals on ice using Biospec minibeadbeater. The lysates were clarified at 13,000 rpm at 4 °C and the concentration of supernatant whole-cell lysates (WCLs) were estimated. 1 mg of WCL was used for FLAG immunoprecipitation (IP) using FLAG-M2 beads and the 3F-PknB or 3F-PknB-GM were eluted with 0.1 M glycine (pH 2.2) and the eluate was neutralized by addition of 1/10th vol 1 M Tris-HCl (pH 8.0). The IPed proteins were resolved on SDS-PAGE and subjected to western blotting. The western blots were probed with 1:10,000 & 1:250 dilution of α-PknB and α-pPknB antibodies. The ratio of phospho-PknB band to that of PknB was evaluated using image J[60]. The in vitro kinase assays were performed in 30 μl reaction volume containing 25 mM HEPES-NaOH, pH 7.4, 20 mM magnesium acetate, 20 mM $MnCl_2$, 1 mM DTT, 100 μM ATP, 10 μCi of $[\gamma^{32}P]ATP$, and 2 μg of GarA and 10 μl eluate from IP for 30 min at 30 °C. The reactions were stopped by adding 15 μl of 6X-SDS sample buffer followed by heating at 95 °C for 5 min Reactions were resolved on 15% SDS-PAGE, transferred to nitrocellulose membrane and autoradiographed. The bands corresponding to pGarA were excised, incubated overnight in the scintillation cocktail (spectrochem) and counts per minute (CPM) were determined using Perkin Elmer microbeta TriLux 1450 LSC & Luminescence counter.

TMT labeling and MS/MS analysis. Cultures pellets were resuspended in SDS lysis buffer (2% SDS, 50 mM Triethylammonium bicarbonate buffer (TEAB; sigma), PhosSTOP tablets (Roche)in PBSG (PBS containing 5% glycerol) at 1:3 (pellet weight in g:buffer) ratio. Samples were heated at 95 °C for 20 min followed by 10 cycles of beadbeating. The lysates were clarified and the concentration of supernatant WCLs were estimated with the help of BCA reagent (Pierce). WCL (250 μg) from each samples shown in Fig. 6e were reduced using 10 mM tris (2-carboxyethyl) phosphine at 55 °C for 1 h and alkylated using 10 mM iodoacetamide for 30 min at 25 °C. Samples were acetone precipitated and the pellet was resuspended in 100 μl of 100 mM TEAB and digested with 6 μg Trypsin (Promega) for 16 h at 37 °C. TMT labeling (Thermo Fisher Scientific) was performed as per manufacturer's instructions. Peptides from $Rv\Delta B::V$ +pristinamycin; $Rv\Delta B::V$ −pristinamycin; $Rv\Delta B::B$ -pristinamycin + IVN; and $Rv\Delta B::B$-GM - pristinamycin + IVN were labeled with 126, 127, 128, and 131 reporter ions respectively. Labeled samples were pooled, dried, and Strong Cation Exchange chromatography (SCX) was performed using two salt gradients, 100 and 350 mM KCl[61]. 1/20th of each fraction was secured for the total proteome analysis. Rest of the sample was enriched for the phosphopeptide using IMAC beads as described earlier[62].

The desalted samples for the total proteome analysis as well as the enriched peptide samples for phosphoproteomics analysis were reconstituted in Buffer A (95% Water, 5% Acetonitrile, 0.1% Formic acid). All experiments were performed using EASY-nLC system (Thermo Fisher Scientific) coupled to LTQ Orbitrap-Velos mass spectrometer (Thermo Fisher Scientific) equipped with nanoelectrospray ion source. A 10-cm PicoFrit Self-Pack microcapillary column (New Objective) was used to resolve the peptide mixture and the peptides were eluted at a flow rate of 300 nl per min for 120 min. The acetonitrile (containing 0.1% formic acid) gradient for the run was 0–40% for 70 min, 40–80% for 10 min, 80% for 10 min, 80–0% for 5 min, and 0% for last 25 min LTQ orbitrap was used for the full MS scan. The peptides were dissociated with both HCD and CID for better MS/MS spectra. The collision energy induced dissociation of X ion precursors was performed at 35 for CID and 40 for HCD. Both MS and MS/MS data were acquired using scan range of 20–2000 M/Z ratios. The dynamic exclusion was set at 500 for both ion trap (CID) and FTMS (HCD) and the resolution was set at 7500. Spectra obtained were queried against *Mtb* H37Rv database (refseq database 85, release date 11 January 2018). Proteome Discoverer 1.3 was used as the search algorithm with oxidation of methionine and carbamidomethylation of cysteine as static modification. Phosphorylation of serine, threonine, and tyrosine was used as a dynamic modification. TMT 6 plex modification of peptide N-termini and lysine residues were set as the fixed modification. The TMT ratios were calculated with TMT126 ($Rv\Delta B::V$ +pristinamycin sample) as the reference comparator. All PSMs were identified at 1% false discovery rate (FDR). Mass tolerance for precursor ions and fragment ions were set at 10 ppm and 0.1 Da respectively. Mass-spectrometry analysis was performed to obtain a list of intensities of various proteins in proteome and phospho-enriched proteome. The phosphorylation sites in the protein for the phosphopeptides were identified with the help of in-house scripts tool for the proteomic analysis (http://protocols.ibioinformatics.org/InHouse/). A localization probability cutoff of 75% was defined in the in-house scripts proteomic analysis tool prior to p-site analysis. The p-sites hence identified were further analyzed for pRS score and PEP values. The p-sites with pRS score >50 and PEP <0.05 were only considered for further analysis. The

common proteins represented in the total proteome and phosphoproteome were analyzed using venn diagram generating tool venny[63]. The phosphointensity ratio of each phosphopeptide was normalized against the whole-protein intensity ratio of the corresponding protein. The normalized phosphointensity from three replicates was averaged and the average phosphointensity ratios were converted into $\log_2$ values. Heatmap was generated using online tool Morpheus (https://software. broadinstitute.org/morpheus/). The functional characterization of individual phosphoproteins identified in the study was done using mycobrowser database. The TMT-phosphoproteomics data has been submitted to the ProteomeXchange Consortium (http://proteomecentral.proteomexchange.org)[64] and can be accessed using data set identifier PXD012180 via the PRIDE partner repository.

Targeted proteomics. Synthetic isotopically labeled (SIL) peptides (Maxi Spike-Tides QL_AAA-peptides) with C-terminus ^{15}N and ^{13}C -labeled arginine were purchased from JPT Peptide Technologies GmbH (Berlin, Germany). The synthetic peptides were resuspended in 0.1 % Formic acid at a final concentration of 1.7 µg per µl and working concentrations of 0.6, 6, 60, and 600 fmol per µl were prepared. All the samples were analyzed using EASY-nLC 1000 system (Thermo Fisher Scientific) coupled to Thermo Fisher-Orbitrap Q- Exactive mass spectrometer (Thermo Scientific, Germany) equipped with nanoelectrospray ion source. Samples were loaded with buffer A and eluted with a 0–40% split gradient of buffer B (95% acetonitrile, 0.1% formic acid) at a flow rate of 300 nl per min for 30 min using 25 cm PicoFrit column. The acquisition method had a non-scheduled parallel reaction monitoring (PRM) event targeting the doubly charged precursor ion of the SIL peptides. The PRM event was performed with an orbitrap resolution of 17500 (at m/z 200), a target AGC value of 1e6, and maximum fill times of 100 ms. Fragmentation was acquired with a normalized collision energy of 27 eV and MS/MS scan range of m/z 100–1500 was used for mass determination. PRM data analysis was performed using skyline-Daily software version 4.1.1.18179 (https://skyline. ms/project/home/begin.view?). For reproducibility and precision of the PRM method, calibration graph was generated in skyline against different SIL peptide concentrations and most confident and intense transitions of the SIL peptide were used for quantification purpose. A fixed amount of SIL peptide (60 fmol) was spiked in each phospho-enriched sample (2 µg) for absolute concentration determination of endogenous phosphopeptide. The skyline file for data analysis has been attached as Supplementary Data 4, 5 and 6.

Data availability

The TMT-phosphoproteomics raw data associated with Figs. 6 and 7 has been submitted to the ProteomeXchange Consortium (http://proteomecentral.proteomexchange.org) and can be accessed using data set identifier PXD012180 via the PRIDE partner repository. The Skyline files for the PRM data analysis (Fig. 8) are submitted as Supplementary Data 4–6. Images of unprocessed western blots, coomassie stained gels, TLC images, and autoradiograms used in the study are provided in Supplementary Fig. 8. The source data underlying Figs. 1a, f, 2d–e, 3c–g, 4c, 5b–d, 6c, d, 7d, e, and 8d are provided as a Source Data file. The source data underlying Fig. 6 are provided in Supplementary Table 1.

References

1. Jones, G. & Dyson, P. Evolution of transmembrane protein kinases implicated in coordinating remodeling of gram-positive peptidoglycan: inside versus outside. *J. Bacteriol.* **188**, 7470–7476 (2006).
2. Manuse, S., Fleurie, A., Zucchini, L., Lesterlin, C. & Grangeasse, C. Role of eukaryotic-like serine/threonine kinases in bacterial cell division and morphogenesis. *FEMS Microbiol. Rev.* **40**, 41–56 (2016).
3. Sassetti, C. M., Boyd, D. H. & Rubin, E. J. Comprehensive identification of conditionally essential genes in mycobacteria. *Proc. Natl Acad. Sci. USA* **98**, 12712–12717 (2001).
4. Fernandez, P. et al. The Ser/Thr protein kinase PknB is essential for sustaining mycobacterial growth. *J. Bacteriol.* **188**, 7778–7784 (2006).
5. Chawla, Y. et al. Protein kinase B (PknB) of Mycobacterium tuberculosis is essential for growth of the pathogen in vitro as well as for survival within the host. *J. Biol. Chem.* **289**, 13858–13875 (2014).
6. Baer, C. E., Lavarone, A. T., Alber, T. & Sassetti, C. M. Biochemical and spatial coincidence in the provisional Ser/Thr protein kinase interaction network of Mycobacterium tuberculosis. *J. Biol. Chem.* **289**, 20422–20433 (2014).
7. Richard-Greenblatt, M. & Av-Gay, Y. Epigenetic phosphorylation control of Mycobacterium tuberculosis infection and persistence. *Microbiol. Spectr.* **5**, 10.1128/microbiolspec.TBTB2-0005-2015 (2017).
8. Kang, C. M. et al. The Mycobacterium tuberculosis serine/threonine kinases PknA and PknB: substrate identification and regulation of cell shape. *Genes Dev.* **19**, 1692–1704 (2005).
9. Ortega, C. et al. Mycobacterium tuberculosis Ser/Thr protein kinase B mediates an oxygen-dependent replication switch. *PLoS Biol.* **12**, e1001746 (2014).
10. Betts, J. C., Lukey, P. T., Robb, L. C., McAdam, R. A. & Duncan, K. Evaluation of a nutrient starvation model of Mycobacterium tuberculosis persistence by gene and protein expression profiling. *Mol. Microbiol.* **43**, 717–731 (2002).
11. Mir, M. et al. The extracytoplasmic domain of the Mycobacterium tuberculosis Ser/Thr kinase PknB binds specific muropeptides and is required for PknB localization. *PLoS Pathog.* **7**, e1002182 (2011).
12. Wang, Q. et al. A comprehensive study of the interaction between peptidoglycan fragments and the extracellular domain of Mycobacterium tuberculosis Ser/Thr kinase PknB. *Chembiochem* **18**, 2094–2098 (2017).
13. Lombana, T. N. et al. Allosteric activation mechanism of the Mycobacterium tuberculosis receptor Ser/Thr protein kinase, PknB. *Structure* **18**, 1667–1677 (2010).
14. Mieczkowski, C., Iavarone, A. T. & Alber, T. Auto-activation mechanism of the Mycobacterium tuberculosis PknB receptor Ser/Thr kinase. *EMBO J.* **27**, 3186–3197 (2008).
15. Wehenkel, A. et al. The structure of PknB in complex with mitoxantrone, an ATP-competitive inhibitor, suggests a mode of protein kinase regulation in mycobacteria. *FEBS Lett.* **580**, 3018–3022 (2006).
16. Zucchini, L. et al. PASTA repeats of the protein kinase StkP interconnect cell constriction and separation of Streptococcus pneumoniae. *Nat. Microbiol.* **3**, 197–209 (2018).
17. Forti, F., Crosta, A. & Ghisotti, D. Pristinamycin-inducible gene regulation in mycobacteria. *J. Biotechnol.* **140**, 270–277 (2009).
18. Barthe, P., Mukamolova, G. V., Roumestand, C. & Cohen-Gonsaud, M. The structure of PknB extracellular PASTA domain from mycobacterium tuberculosis suggests a ligand-dependent kinase activation. *Structure* **18**, 606–615 (2010).
19. Prigozhin, D. M. et al. Structural and genetic analyses of the Mycobacterium tuberculosis Protein Kinase B sensor domain identify a potential ligand-binding site. *J. Biol. Chem.* **291**, 22961–22969 (2016).
20. Crick, D. C., Mahapatra, S. & Brennan, P. J. Biosynthesis of the arabinogalactan-peptidoglycan complex of Mycobacterium tuberculosis. *Glycobiology* **11**, 107R–118R (2001).
21. Mahapatra, S. et al. Mycobacterial lipid II is composed of a complex mixture of modified muramyl and peptide moieties linked to decaprenyl phosphate. *J. Bacteriol.* **187**, 2747–2757 (2005).
22. Hardt, P. et al. The cell wall precursor lipid II acts as a molecular signal for the Ser/Thr kinase PknB of Staphylococcus aureus. *Int. J. Med. Microbiol.* **307**, 1–10 (2017).
23. Jani, C. et al. Regulation of polar peptidoglycan biosynthesis by Wag31 phosphorylation in Mycobacteria. *BMC Microbiol.* **10**, 327 (2010).
24. Breukink, E. et al. Use of the cell wall precursor lipid II by a pore-forming peptide antibiotic. *Science* **286**, 2361–2364 (1999).
25. Wiedemann, I. et al. Specific binding of nisin to the peptidoglycan precursor lipid II combines pore formation and inhibition of cell wall biosynthesis for potent antibiotic activity. *J. Biol. Chem.* **276**, 1772–1779 (2001).
26. Hsu, S. T. et al. The nisin-lipid II complex reveals a pyrophosphate cage that provides a blueprint for novel antibiotics. *Nat. Struct. Mol. Biol.* **11**, 963–967 (2004).
27. Duran, R. et al. Conserved autophosphorylation pattern in activation loops and juxtamembrane regions of Mycobacterium tuberculosis Ser/Thr protein kinases. *Biochem. Biophys. Res. Commun.* **333**, 858–867 (2005).
28. Young, T. A., Delagoutte, B., Endrizzi, J. A., Falick, A. M. & Alber, T. Structure of Mycobacterium tuberculosis PknB supports a universal activation mechanism for Ser/Thr protein kinases. *Nat. Struct. Biol.* **10**, 168–174 (2003).
29. Prisic, S. et al. Extensive phosphorylation with overlapping specificity by Mycobacterium tuberculosis serine/threonine protein kinases. *Proc. Natl Acad. Sci. USA* **107**, 7521–7526 (2010).
30. Fortuin, S. et al. Phosphoproteomics analysis of a clinical Mycobacterium tuberculosis Beijing isolate: expanding the mycobacterial phosphoproteome catalog. *Front. Microbiol.* **6**, 6 (2015).
31. Verma, R. et al. Quantitative proteomic and phosphoproteomic analysis of H37Ra and H37Rv strains of Mycobacterium tuberculosis. *J. Proteome Res.* **16**, 1632–1645 (2017).
32. Sajid, A. et al. Interaction of Mycobacterium tuberculosis elongation factor Tu with GTP is regulated by phosphorylation. *J. Bacteriol.* **193**, 5347–5358 (2011).
33. Gupta, M. et al. HupB, a nucleoid-associated protein of Mycobacterium tuberculosis, is modified by serine/threonine protein kinases in vivo. *J. Bacteriol.* **196**, 2646–2657 (2014).
34. Carette, X. et al. Multisystem Analysis of Mycobacterium tuberculosis Reveals Kinase-Dependent Remodeling of the Pathogen-Environment Interface. *MBio* **9**, e02333-17 (2018).
35. Kusebauch, U. et al. Mycobacterium tuberculosis supports protein tyrosine phosphorylation. *Proc. Natl Acad. Sci. USA* **111**, 9265–9270 (2014).

36. O'Hare, H. M. et al. Regulation of glutamate metabolism by protein kinases in mycobacteria. *Mol. Microbiol.* **70**, 1408–1423 (2008).

37. Khan, M. Z. et al. Protein kinase G confers survival advantage to Mycobacterium tuberculosis during latency-like conditions. *J. Biol. Chem.* **292**, 16093–16108 (2017).

38. Zhang, C. C. Bacterial signalling involving eukaryotic-type protein kinases. *Mol. Microbiol.* **20**, 9–15 (1996).

39. Ortiz-Lombardia, M., Pompeo, F., Boitel, B. & Alzari, P. M. Crystal structure of the catalytic domain of the PknB serine/threonine kinase from Mycobacterium tuberculosis. *J. Biol. Chem.* **278**, 13094–13100 (2003).

40. Yeats, C., Finn, R. D. & Bateman, A. The PASTA domain: a beta-lactam-binding domain. *Trends Biochem. Sci.* **27**, 438 (2002).

41. Shah, I. M., Laaberki, M. H., Popham, D. L. & Dworkin, J. A eukaryotic-like Ser/Thr kinase signals bacteria to exit dormancy in response to peptidoglycan fragments. *Cell* **135**, 486–496 (2008).

42. Righino, B. et al. Structural model of the full-length Ser/Thr protein kinase StkP from S. pneumoniae and its recognition of peptidoglycan fragments. *J. Biomol. Struct. Dyn.* **7**, 1–14 (2017).

43. Turapov, O. et al. The external PASTA domain of the essential serine/threonine protein kinase PknB regulates mycobacterial growth. *Open Biol.* **5**, 150025 (2015).

44. Mahapatra, S., Crick, D. C., McNeil, M. R. & Brennan, P. J. Unique structural features of the peptidoglycan of Mycobacterium leprae. *J. Bacteriol.* **190**, 655–661 (2008).

45. Gee, C. L. et al. A phosphorylated pseudokinase complex controls cell wall synthesis in mycobacteria. *Sci. Signal.* **5**, ra7 (2012).

46. Turapov, O. et al. Two faces of CwlM, an essential PknB substrate, in Mycobacterium tuberculosis. *Cell Rep.* **25**, 57–67 e55 (2018).

47. Pompeo, F., Foulquier, E., Serrano, B., Grangeasse, C. & Galinier, A. Phosphorylation of the cell division protein GpsB regulates PrkC kinase activity through a negative feedback loop in Bacillus subtilis. *Mol. Microbiol.* **97**, 139–150 (2015).

48. Khan, S. et al. Phosphorylation of enoyl-acyl carrier protein reductase InhA impacts mycobacterial growth and survival. *J. Biol. Chem.* **285**, 37860–37871 (2010).

49. Molle, V. et al. Phosphorylation of InhA inhibits mycolic acid biosynthesis and growth of Mycobacterium tuberculosis. *Mol. Microbiol.* **78**, 1591–1605 (2010).

50. Vilcheze, C. et al. Phosphorylation of KasB regulates virulence and acid-fastness in Mycobacterium tuberculosis. *PLoS Pathog.* **10**, e1004115 (2014).

51. Corrales, R. M. et al. Phosphorylation of mycobacterial PcaA inhibits mycolic acid cyclopropanation: consequences for intracellular survival and for phagosome maturation block. *J. Biol. Chem.* **287**, 26187–26199 (2012).

52. Pandey, A. K. et al. Nitrile-inducible gene expression in mycobacteria. *Tuberculosis (Edinb.)* **89**, 12–16 (2009).

53. Nagarajan, S. N. et al. Protein kinase A (PknA) of Mycobacterium tuberculosis is independently activated and is critical for growth in vitro and survival of the pathogen in the host. *J. Biol. Chem.* **290**, 9626–9645 (2015).

54. Puri, R. V., Reddy, P. V. & Tyagi, A. K. Secreted acid phosphatase (SapM) of Mycobacterium tuberculosis is indispensable for arresting phagosomal maturation and growth of the pathogen in guinea pig tissues. *PLoS ONE* **8**, e70514 (2013).

55. Dominguez, C., Boelens, R. & Bonvin, A. M. HADDOCK: a protein-protein docking approach based on biochemical or biophysical information. *J. Am. Chem. Soc.* **125**, 1731–1737 (2003).

56. de Vries, S. J. et al. HADDOCK versus HADDOCK: new features and performance of HADDOCK2.0 on the CAPRI targets. *Proteins* **69**, 726–733 (2007).

57. Morris, G. M. et al. Automated docking using a Lamarckian genetic algorithm and and empirical binding free energy function. *J. Comput. Chem.* **19**, 1639–1662 (1998).

58. O'Boyle, N. M. et al. Open Babel: an open chemical toolbox. *J. Cheminform.* **3**, 33 (2011).

59. Jain, R., Watson, U., Vasudevan, L. & Saini, D. K. ERK activation pathways downstream of GPCRs. *Int. Rev. Cell Mol. Biol.* **338**, 79–109 (2018).

60. Schneider, C. A., Rasband, W. S. & Eliceiri, K. W. NIH Image to ImageJ: 25 years of image analysis. *Nat. Methods* **9**, 671–675 (2012).

61. Dephoure, N. & Gygi, S. P. A solid phase extraction-based platform for rapid phosphoproteomic analysis. *Methods* **54**, 379–386 (2011).

62. Shaik, A. A. et al. Phosphoprotein network analysis of white adipose tissues unveils deregulated pathways in response to high-fat diet. *Sci. Rep.* **6**, 25844 (2016).

63. Oliveros, J. C. VENNY. An interactive tool for comparing lists with Venn's diagrams (2007–2015).

64. Vizcaino, J. A. et al. 2016 update of the PRIDE database and its related tools. *Nucleic Acids Res.* **44**, D447–D456 (2016).

Author contributions
P.K., M.R., B.M., U.W., N.P.D., Y.C., S.S., and K.S. were involved in execution of experiments, data acquisition, analysis, and providing raw data for figures. T.S., G.D.J., D.S., D.M., F.G., and V.K.N. provided the scientific overview. P.K. and V.K.N. were involved in overall experimental design, manuscript writing, and making figures. V.K.N. guided the study.

Additional information
Supplementary Information accompanies this paper at https://doi.org/10.1038/s41467-019-09223-9.

Competing interests: The authors declare no competing interests.

Reprints and permission information is available online at http://npg.nature.com/reprintsandpermissions/

Journal peer review information: *Nature Communications* thanks Nelson da Cruz Soares and Robert Husson for their contribution to the peer review of this work. Peer reviewer reports are available.

Publisher's note: Springer Nature remains neutral with regard to jurisdictional claims in published maps and institutional affiliations.